Karlsruhe Institute of Technology

# Evolution of silicon sensor parameters of the CMS tracker due to continuous irradiation during operation

Master's thesis of

Julia Hunt

at the
Institute of Experimental Particle Physics

| | |
|---|---|
| Reviewer: | Prof. Dr. Thomas Müller |
| Second reviewer: | Prof. Dr. Ulrich Husemann |
| Advisors: | Dr. Frank Hartmann |
| | Dr. Erik Butz |

01 November 2017 – 31 October 2018

Ich versichere wahrheitsgemäß, die Arbeit selbstständig angefertigt, alle benutzten Hilfsmittel vollständig und genau angegeben und alles kenntlich gemacht zu haben, was aus Arbeiten anderer unverändert oder mit Änderungen entnommen wurde.

**Karlsruhe, 30.10.2018**

. . . . . . . . . . . . . . . . . . . . . . . . . . . . . . . . . .

(Julia Hunt)

# Abstract

In the near-beam environment of the Large Hadron Collider, the tracker of the CMS experiment is exposed to high radiation levels. Depending on their position with respect to the interaction point, where the particle collisions take place, the silicon detectors were designed to withstand fluences of $10^{14}$ to $10^{15}$ MeV $n_{eq}/cm^2$. Microscopic radiation-induced damage in the silicon sensors has important consequences on the evolution of sensor parameters like charge collection efficiency, full depletion voltage and leakage current. In order to provide a fact base for decisions concerning operational settings, these and other sensor parameters are continuously monitored in both the pixel and strip tracker.

The scope of this master's thesis includes establishing a simulation tool for the pixel tracker that predicts the evolution of leakage current and depletion voltage based on fluence and temperature history. A similar tool for the strip tracker had been developed in 2011 by C. Barth [1]. His work was continued and served as a basis for the pixel tracker modelling tool. The leakage current evolution is modelled according to a well-established empirical model, which describes the evolution with fluence, temperature, and time [2]. The full depletion voltage of the sensors is calculated from an effective charge concentration. The latter was obtained from the Hamburg model [2].

Comparisons of the pixel tracker depletion voltage and leakage current modelling results with available detector data have been performed to obtain a general understanding of the tool and its input parameters. Predictions on the evolution of the detector parameters were performed in close coordination with the monitoring and operation groups of the pixel and strip tracker. Several times during the past year, the results of the tool provided a basis for decisions on detector operation procedures.

Both the strip tracker and pixel tracker tools are imparted in a functional state and may contribute to the monitoring and prediction of the leakage current and depletion voltage in the coming years.

# Zusammenfassung

In der direkten Umgebung des Large Hadron Colliders ist der Spurdetektor des CMS Experiments hoher Strahlungsbelastung ausgesetzt. Abhängig von ihrer Position in Bezug auf den Interaktionspunkt, an welchem die Teilchenkollisionen stattfinden, sind die Siliziumdetektoren dafür ausgelegt, Fluenzen bis $10^{14}$ oder $10^{15}$ MeV $n_{eq}/cm^2$ standzuhalten. Mikroskopische Strahlenschäden in den Siliziumsensoren beeinflussen die Entwicklung von Sensorparametern wie Ladungssammlungseffizienz, Verarmungsspannung und Leckstrom. Diese und andere Sensorparameter werden sowohl im Pixel-, als auch im Streifenspurdetektor kontinuierlich überwacht, um eine Faktenbasis für Entscheidungen bezüglich der Betriebseinstellungen des Detektors bereitzustellen.

Diese Masterarbeit umfasst die Etablierung eines Simulationswerkzeugs für den Pixeldetektor, welches basierend auf der Fluenz- und Temperaturhistorie die Entwicklung von Leckstrom und Verarmungsspannung vorhersagt. Ein ähnliches Werkzeug war 2011 von C. Barth für den Streifendetektor entwickelt worden [1]. Seine Arbeit wurde wiederaufgegriffen und diente als Grundlage für das Pixeldetektor-Simulationswerkzeug. Die Leckstromentwicklung wird anhand eines etablierten empirischen Modells berechnet, welches die Entwicklung in Abhängigkeit von Fluenz, Temperatur und Zeit beschreibt. Die Verarmungsspannung der Sensoren wird aus seiner effektiven Ladungskonzentration bestimmt. Letztere wird aus dem Hamburg-Modell gewonnen.

Vergleiche der Vorhersagen mit verfügbaren Detektordaten zu Verarmungsspannung und Leckstrom wurden durchgeführt, um ein allgemeines Verständnis des Simulationswerkzeugs und seiner Eingangsparameter zu gewinnen. Vorhersagen zur Entwicklung der Detektorparameter wurden in enger Absprache mit den für das Monitoring und den Detektorbetrieb zuständigen Gruppen des Pixel- und Streifendetektors gemacht. Mehrmals wurden im vergangenen Jahr basierend auf den Ergebnissen des Simulationswerkzeugs Entscheidungen zum Detektorbetrieb getroffen.

Die Simulationswerkzeuge für den Streifen- und Pixeldetektor werden in einem funktionalen Zustand weitergegeben. Sie werden in den kommenden Jahren einen Beitrag zur Überwachung und Vorhersage der Leckströme und Verarmungsspannungen leisten können.

# Contents

# 1. Introduction

The Large Hadron Collider (LHC) at the European Organisation for Nuclear Research CERN[1] near Geneva is a high energy physics particle accelerator. At the time of writing in 2018, the LHC has been successfully operated for several years.

The LHC constantly passes through cycles of physics data-taking, called runs, and breaks of various duration. A timeline of the LHC programme is shown in Figure 1.1.

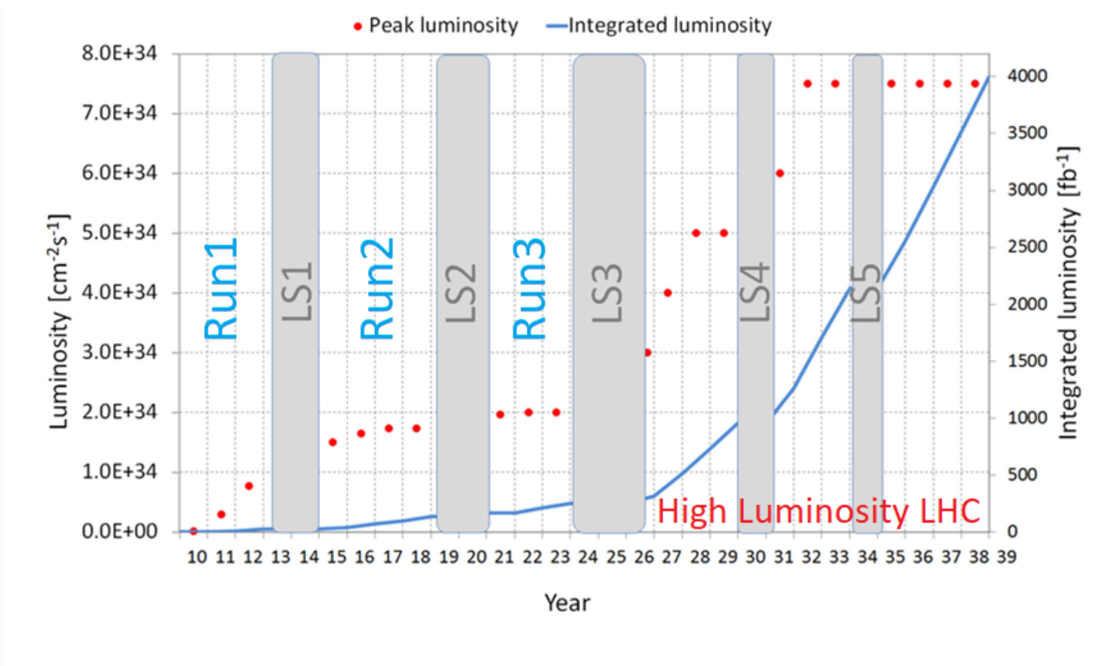


Figure 1.1.: Roadmap of the LHC programme showing the periods of data-taking and the long shutdowns (LS). The first period of data-taking, Run 1, lasted from 2010 to 2013. It was followed by LS1 until the end of 2014. Currently the end of Run 2 is approaching and with it LS2, which is scheduled from December 2018 until early 2021. The increasing integrated luminosity corresponds to the increasing amount of data delivered by the machine. Adapted from [3].

Major upgrade programmes of the LHC and the experiments, in the scope of which newest research and development results are incorporated in the experimental setup, may take several years of installation time. To this end *long shutdowns* (LS) are necessary.

Shorter breaks are also budgeted for: *Technical stops* (TS), a couple of days every few weeks during operations, are often enough to perform smaller repairs. Over the winter

[1] formerly Conseil Européen pour la Recherche Nucléaire

months the LHC is shut down for the *year end technical stop* (YETS), during which more complex repairs or replacements can be performed.

All collaborations operating experiments along the LHC particle accelerator ring have to coordinate their maintainance accesses minutely; access is not possible while beams of particles are circulating in the ring due to radiation exposure.

The CMS (*Compact Muon Solenoid*) experiment has now collected a total integrated luminosity of about 170 $\text{fb}^{-1}$ since 2010. Recorded integrated luminosity is a measure for the amount of data collected, and is therefore a key figure of merit of any experiment. Yet a high integrated luminosity entails that the detector has seen a high irradiation level, which involves radiation damage inflicted by the traversing particles.

Located in the centre of the CMS experiment, where the radiation environment is harshest, is the pixel tracker. It has been built in a way that allows comparatively quick access during a YETS or even TS for replacements which are necessary due to the higher radiation dose close to the beampipe.

The pixel tracker underwent an evolutionary upgrade during the *extended year-end technical stop* (EYETS) 16/17 from *Phase-0* (installed in 2008, data-taking since the start of Run 1 in 2010, operated until 2016) to *Phase-1* (since 2017). During the upcoming LS2 the innermost pixel barrel layer will be replaced. Afterwards the pixel tracker will be prepared for operation throughout Run 3 until its *Phase-2* upgrade, which is scheduled for LS3.

The strip tracker surrounding the pixel tracker was not devised to be maintained in a similar fashion. Therefore the design had to be extraordinarily robust, reliable, and long-term radiation tolerant. The upgrade of the strip tracker is scheduled for LS3. During LS3, all experiments as well as the accelerator itself will undergo comprehensive upgrades. This happens in preparation for the era of the *High Luminosity LHC* (HL-LHC) thereafter.

Constant monitoring of the detector health is crucial for both the strip and the pixel detector: Operational settings such as temperature can mitigate or aggravate the consequences of radiation damage on detector parameters. Decisions must be carefully taken with both the longevity of the detector and the primary goal of physics data-taking in mind.

The scope of this thesis included resuming and establishing tools which contribute to the monitoring activities concerning the strip and pixel tracker. The aim was to model radiation-dependent detector parameters and provide projections for the future.

# 2. Silicon detectors

## 2.1. Material choice silicon

Semiconductors like silicon or germanium are a suitable material for a tracking detector for several reasons [4]. In comparison with gas detectors, better position resolutions are achievable due to smaller cell size. Faster signals thanks to high carrier mobility leads in turn to shorter dead times. For the LHC, the geometry and exact composition of the silicon sensors can be engineered to be less sensitive to some kind of radiation-induced damage [5], as the damage mechanisms are understood to a large extent.

Silicon has additional advantages as tracking detector material. A mature manufacturing infrastructure is on hand thanks to wide applications of silicon sensors in industry. As opposed to other semiconductors like germanium or gallium arsenide, silicon is readily available in nature; quantity being an important factor when considering the detector area that needs to be instrumented. The existence of a natural oxide, silicon dioxide $SiO_2$, with suitable properties, is a crucial aspect. $SiO_2$ is chemically inert and withstands high field strengths, making it a prime choice for an isolation layer of a silicon sensor. The energy resolution of silicon is also favourable: It is defined by the threshold ionisation energy, which is a mere 3.6 eV. In gas detectors the ionisation energy lies around 20-40 eV.

Main drawbacks of semiconductor detectors are the inconveniently high energy loss of particles in the dense material as well as the higher cost factor in production.

## 2.2. Energy band model and band gap of silicon

The remainder of this chapter closely follows lines of argument which can be found e.g. in [1, 2, 4, 6, 7, 8, 9].

A semiconductor may behave as an electric insulator or as a conductor, depending on its temperature. This macroscopic property can be understood in the context of the energy band model, described e.g. in [6, 7, 8]: The material is approximated as a perfect monocrystal with a regular crystal lattice and infinite dimensions. Possible energy states of the charge carriers in the material are governed by quantum mechanics.

If visualised in an energy-position *band diagram* or energy-momentum *band structure plot*, these possible states form quasi-continuous energy bands that define the parameter space in which the charge carriers can exist. The band structure of silicon is shown in Figure 2.1.

In the ground state at absolute zero temperature only the lowest energy states are occupied. The highest energy band whose states are fully occupied at 0 K is termed *valence band*. Above it lies the *conduction band*.

Only partially filled bands allow transport of charge. *Charge carriers* are thus either electrons in energy states of the conduction band, or *holes* – unoccupied states in the valence band, which can be interpreted as positively charged quasi-particles.

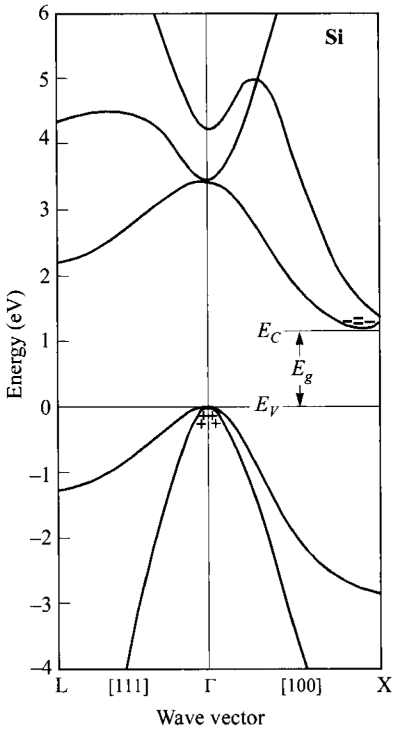


Figure 2.1.: Band structure of the indirect semiconductor silicon. $E_g$ marks the band gap energy. Taken from [8].

The density of free charge carriers ($n$ for electrons and $p$ for holes) can be written as

$$n = \int_{E_C}^{\infty} D(E) f(E,T) \mathrm{d}E \quad \text{and} \quad p = \int_{-\infty}^{E_V} D(E) \left(1 - f(E,T)\right) \mathrm{d}E. \tag{2.1}$$

Integration limits are the upper edge of the valence band $E_V$ and the lower edge of the conduction band $E_C$, respectively. $D(E)$ is the density of states. The Fermi-Dirac distribution $f(E,T)$ accounts for the fact that electrons are fermions and thus follow Fermi-Dirac statistics. It describes the fraction of occupied states of an energy $E$ at $T > 0$ K in thermodynamic equilibrium and is given by

$$f(E,T) = \frac{1}{\exp\left(\frac{E-E_F}{k_B T}\right) + 1}. \tag{2.2}$$

$k_B$ is the Boltzmann constant. The Fermi energy $E_F$ is the highest energy a fermion can have in the ground state at absolute zero temperature.

The formula for $D(E)$ of a free electron gas must be modified by introducing effective masses for electrons $m_n^*$ and holes $m_p^*$. This is to account for the fact that in a semiconductor the charge carriers are not free, but are moving through electric and magnetic fields in the crystal lattice, resulting in

$$D_C(E) = \frac{(2m_n^*)^{3/2}}{2\pi^2\hbar^3}\sqrt{E - E_C} \quad \text{for } E > E_C \tag{2.3}$$

$$D_V(E) = \frac{(2m_p^*)^{3/2}}{2\pi^2\hbar^3}\sqrt{E_V - E} \quad \text{for } E < E_V. \tag{2.4}$$

Semiconductors and insulators possess a band gap: No energy states with $E_V < E < E_C$ exist. Unlike insulators however, semiconductors have a small enough band gap for thermal energies around room temperature to lift charge carriers into the conduction band.

For intrinsic semiconductors Equation (2.2) can be approximated by a Boltzmann distribution

$$f(E,T) \approx \exp\left(\frac{-(E - E_F)}{k_B T}\right) \quad \text{for } E > E_F. \tag{2.5}$$

This approximation remains valid for small enough defect concentrations. Charge carrier densities can then be expressed through effective state densities

$$\mathcal{N}_{C,\,V} = 2\left(\frac{m_{n,p}^* k_B T}{2\pi\hbar^2}\right)^{3/2} \tag{2.6}$$

as

$$n = \mathcal{N}_C \exp\frac{-(E_C - E_F)}{k_B T} \quad \text{for } E > E_C \tag{2.7}$$

$$p = \mathcal{N}_V \exp\frac{(E_V - E_F)}{k_B T} \quad \text{for } E < E_V. \tag{2.8}$$

For an intrinsic semiconductor charge neutrality $n_i = p_i$ is given. It follows that $E_F$ lies in the middle between the valence and conduction band for $T = 0$ K:

$$E_F = \frac{E_C + E_V}{2} + \frac{k_B T}{2}\ln\left(\frac{\mathcal{N}_V}{\mathcal{N}_C}\right) \tag{2.9}$$

Semiconductors can be further subdivided into *direct* and *indirect* types:

If the minimum of the conduction band and the maximum of the valence band coincide at the same momentum in an energy-momentum plot, an electron can change the band without changing its momentum. This defines a direct semiconductor.

In an indirect semiconductor the least energy costly transition from valence to conduction band requires a change of the momentum of the electron, as energy and quasi-momentum have to be conserved simultaneously in the process. The lattice will take the excess, thus a phonon[1] is created in the process. Silicon is such an indirect semiconductor. Its band gap is 1.12 eV, as shown in Figure 2.1, but the ionisation energy for an electron-hole pair is 3.6 eV due to the additionally necessary phonon creation.

[1]Phonons are virtual particles that represent excitations of the crystal lattice.

## 2.3. Doping of semiconductors

Silicon is a semiconductor with four valence electrons and therefore belongs to group IV of the periodic table. Its lattice has the same structure as diamond and bonds between the atoms are covalent. Conductivity and band gap properties of a semiconductor can be purposefully altered by introducing impurity atoms with suitable electron configurations. This process is called *doping*. An element of group IV is commonly doped with group III or group V atoms. Group V elements will function as *donors*: They carry an additional valence electron compared to the surrounding atoms. The Coulomb binding of the fifth electron to the atom is effectively weakened by the covalent binding structure of the crystal and it is therefore easier to "free" the fifth electron. It will contribute to the conductivity of the material at room temperature. A semiconductor doped with a donor is called *n-type*. Electrons are the majority charge carriers in this case.

Similarly, group III elements will function as *acceptors*: They lack a fourth electron to fit into the surrounding covalent binding structure. As one of the surrounding electrons is therefore likely to take the place, the resulting holes traverse the crystal structure as majority charge carriers. Acceptor doped semiconductors are called *p-type*.

The doping concentrations for donors $n_\mathrm{D}$ and acceptors $n_\mathrm{A}$ can be split into an ionised (charged) fraction, and a non-ionised (neutral) one

$$n_\mathrm{D} = n_\mathrm{D}^+ + n_\mathrm{D}^0 \tag{2.10}$$

$$n_\mathrm{A} = n_\mathrm{A}^- + n_\mathrm{A}^0. \tag{2.11}$$

For the temperature regime relevant for CMS silicon detectors (around ±20 °C), all impurities are ionised: $n_\mathrm{A}^0 = 0$ and $n_\mathrm{D}^0 = 0$, and the effective doping concentration is

$$n_\mathrm{A} - n_\mathrm{D} = n_\mathrm{A}^- - n_\mathrm{D}^+. \tag{2.12}$$

Further, overall charge neutrality still holds even though the dopant atoms themselves are immobile and do not contribute to the charge transport

$$n + n_\mathrm{A}^- = p + n_\mathrm{D}^+. \tag{2.13}$$

From Equation (2.12) and Equation (2.13) follows that the effective doping concentration is equal to the effective charge concentration $N_\mathrm{eff}$:

$$n_\mathrm{A} - n_\mathrm{D} = p - n = N_\mathrm{eff}. \tag{2.14}$$

Thus doping leads to an inequality between positive and negative charge carriers $n \neq p$ and shifts the Fermi energy of the system. In an n-doped semiconductor, the additional electrons shift $E_\mathrm{F}$ towards the conduction band. In a p-type semiconductor, $E_\mathrm{F}$ lies closer to the valence band.

## 2.4. Microscopic parameters of silicon

### 2.4.1. Mobility

*Mobility* $\mu$ of the free charge carriers is defined in terms of the electron charge $e$, the effective mass $m^*$ and the time $\tau$ between two interactions with phonons or impurities in the lattice

$$\mu = \frac{e\tau}{m^*_{\mathrm{n,p}}} \tag{2.15}$$

Good charge carrier mobility is a desirable feature in a high energy physics sensor, since it corresponds to fast signal times.

### 2.4.2. Conductivity

*Conductivity* $\sigma$ of the material depends on the mobilities of the electrons and holes $\mu_{\mathrm{n,p}}$

$$\sigma = e\left(n\mu_{\mathrm{n}} + p\mu_{\mathrm{p}}\right). \tag{2.16}$$

For high doping concentrations either of acceptors or of donors, the formula simplifies due to

$$p \approx n_{\mathrm{A}} \gg n \quad \text{for p-type} \tag{2.17}$$

$$n \approx n_{\mathrm{D}} \gg p \quad \text{for n-type} \tag{2.18}$$

respectively.

Conductivity depends on the doping concentration in two ways: There is an obvious direct dependence on $n_{\mathrm{D,A}}$ and another one via $\mu(\tau)$, compare Equation (2.15): Scattering occurs more often in materials with more defects, thus $\tau$ is smaller and mobility is lower for higher doping concentrations.

### 2.4.3. Resistivity

The reciprocal of the conductivity is *resistivity* $\rho$

$$\rho = \frac{1}{\sigma}. \tag{2.19}$$

$\rho$ is a very important design parameter of detectors, since the necessary voltage for detector operation depends on it (see Equation (2.38)).

In case of high n-type doping, as e.g. in the CMS silicon sensor bulk

$$\rho \approx \frac{1}{e\mu n_{\mathrm{D}}}. \tag{2.20}$$

## 2.5. p-n junction

When an n-type and p-type semiconductor are brought into contact, the initially different Fermi levels provoke a rearrangement of charge carriers. The electrons occupying higher energy levels on the n-type side will drift towards the initially lower Fermi levels in the p-type material, where energetically more favourable states are now available. They leave ionised group V atoms behind. This is equivalent with holes diffusing in the opposite direction.

At some point the electric potential generated by the ionised dopants is strong enough to prevent further charge carrier diffusion; the Fermi level is now constant everywhere. Around the interface of the n- and p-doped material a *space charge region* (SCR) has formed, see Figure 2.2. It is naturally depleted of all free charge carriers $n = p \approx 0$ before irradiation (indicated by subscript 0), and consequently

$$N_{\mathrm{eff,n,0}} = n_{\mathrm{D}} \tag{2.21}$$

$$N_{\mathrm{eff,p,0}} = n_{\mathrm{A}}. \tag{2.22}$$

This equilibrium state is reached at the *built-in voltage* $V_{\mathrm{bi}}$, to be derived in the following. The extent of the SCR into the n-type material $x_{\mathrm{n}}$ and p-type material $x_{\mathrm{p}}$ is usually different, depending on doping concentrations.

### 2.5.1. Electric field in the space charge region

With Poisson's equation

**Poisson's equation**

$$-\frac{\mathrm{d}^2\Phi(x)}{\mathrm{d}x^2} = \frac{\rho(x)}{\epsilon\epsilon_0} \tag{2.23}$$

the shape of the electric field in the space charge region can be calculated. The result is also shown in Figure 2.2.

Let $x = 0$ be the position of the interface between the p- and n-type semiconductor; $-x_{\mathrm{p}}$ be the end of the SCR in the p-type semiconductor and $x_{\mathrm{n}}$ the extent of the SCR into the n-type semiconductor. Assuming that the charge distribution $\rho(x)$ is constant within the SCR $-x_{\mathrm{p}} < x < +x_{\mathrm{n}}$ outside which it abruptly goes to zero, it can be written as

**Depletion approximation**

$$\rho(x) = e\left(N_{\mathrm{eff,p}}\theta(-x)\theta(x + x_{\mathrm{p}}) + N_{\mathrm{eff,n}}\theta(x_{\mathrm{n}} - x)\theta(x)\right), \tag{2.24}$$

with the Heaviside step function $\theta(x)$.

The resulting electric fields on either side of the p-n junction have a linear dependence on $x$:

$$E_{\mathrm{p}}(x) = -\int_{-x_{\mathrm{p}}}^{x} \frac{\mathrm{d}^2\Phi}{\mathrm{d}x^2} = -\frac{\mathrm{d}\Phi}{\mathrm{d}x} = -\frac{qN_{\mathrm{eff,p}}}{\epsilon\epsilon_0}\left(x + x_{\mathrm{p}}\right) \tag{2.25}$$

$$E_{\mathrm{n}}(x) = \int_{x}^{x_{\mathrm{n}}} \frac{\mathrm{d}^2\Phi}{\mathrm{d}x^2} = -\frac{\mathrm{d}\Phi}{\mathrm{d}x} = \frac{qN_{\mathrm{eff,n}}}{\epsilon\epsilon_0}\left(x - x_{\mathrm{n}}\right) \tag{2.26}$$

where the boundary conditions $\frac{\mathrm{d}\Phi}{\mathrm{d}x}|_{x=-x_{\mathrm{p}}} = \frac{\mathrm{d}\Phi}{\mathrm{d}x}|_{x=x_{\mathrm{n}}} = 0$ were used.

The maximum of the field at $x = 0$ is $E_{\mathrm{max}} = \frac{qN_{\mathrm{eff,p}}x_{\mathrm{p}}}{\epsilon\epsilon_0} = \frac{qN_{\mathrm{eff,n}}x_{\mathrm{n}}}{\epsilon\epsilon_0}$. This can be rewritten in terms of the width of the depleted zone $w$:

$$E_{\mathrm{max}} = \frac{q}{\epsilon\epsilon_0}\left(\frac{N_{\mathrm{eff,p}}x_p}{2(x_{\mathrm{p}} + x_{\mathrm{n}})} + \frac{N_{\mathrm{eff,n}}x_n}{2(x_{\mathrm{p}} + x_{\mathrm{n}})}\right)w = \frac{q}{2\epsilon\epsilon_0}\left(\frac{1}{\frac{1}{N_{\mathrm{eff,p}}} + \frac{1}{N_{\mathrm{eff,n}}}}\right)w. \tag{2.27}$$

Integrating a second time yields the built-in voltage and its dependence on $w$

$$V_{\mathrm{bi}} = -\int_{-x_{\mathrm{p}}}^{0} \frac{qN_{\mathrm{eff,p}}}{\epsilon\epsilon_0}\left(x + x_{\mathrm{p}}\right)\mathrm{d}x - \int_{0}^{x_{\mathrm{n}}} \frac{qN_{\mathrm{eff,n}}}{\epsilon\epsilon_0}\left(x - x_{\mathrm{n}}\right)\mathrm{d}x \tag{2.28}$$

$$= \frac{qN_{\mathrm{eff,p}}x_{\mathrm{p}}^2}{\epsilon\epsilon_0} + \frac{qN_{\mathrm{eff,n}}x_{\mathrm{n}}^2}{\epsilon\epsilon_0} \tag{2.29}$$

$$= \frac{1}{2}E_{\mathrm{max}}w. \tag{2.30}$$

### 2.5.2. Diodes in reverse bias

A p-n junction can be operated as a diode by applying an external voltage $V_{\mathrm{bias}}$. Depending on the polarity of the bias voltage, the p-n junction is either conductive (forward bias: positive terminal at p-doped side) or non-conductive (reverse bias: positive terminal at n-doped side).

An applied reverse bias allows further charge carriers to diffuse through the interface between p and n-doped material, allowing deliberate control of the SCR width.

$V_{\mathrm{bias}}$ alters the difference in potential in Equation (2.28) to

$$V_{\mathrm{bi}} + V_{\mathrm{bias}} = \frac{1}{2}E_{\mathrm{max}}w \tag{2.31}$$

The width of the depletion zone under external voltage then follows from Equation (2.28), Equation (2.27), and Equation (2.31):

$$w = \sqrt{\frac{2\epsilon\epsilon_0}{q}\left(\frac{1}{N_{\mathrm{eff,n}}} + \frac{1}{N_{\mathrm{eff,p}}}\right)\left(V_{\mathrm{bi}} + V_{\mathrm{bias}}\right)} \tag{2.32}$$

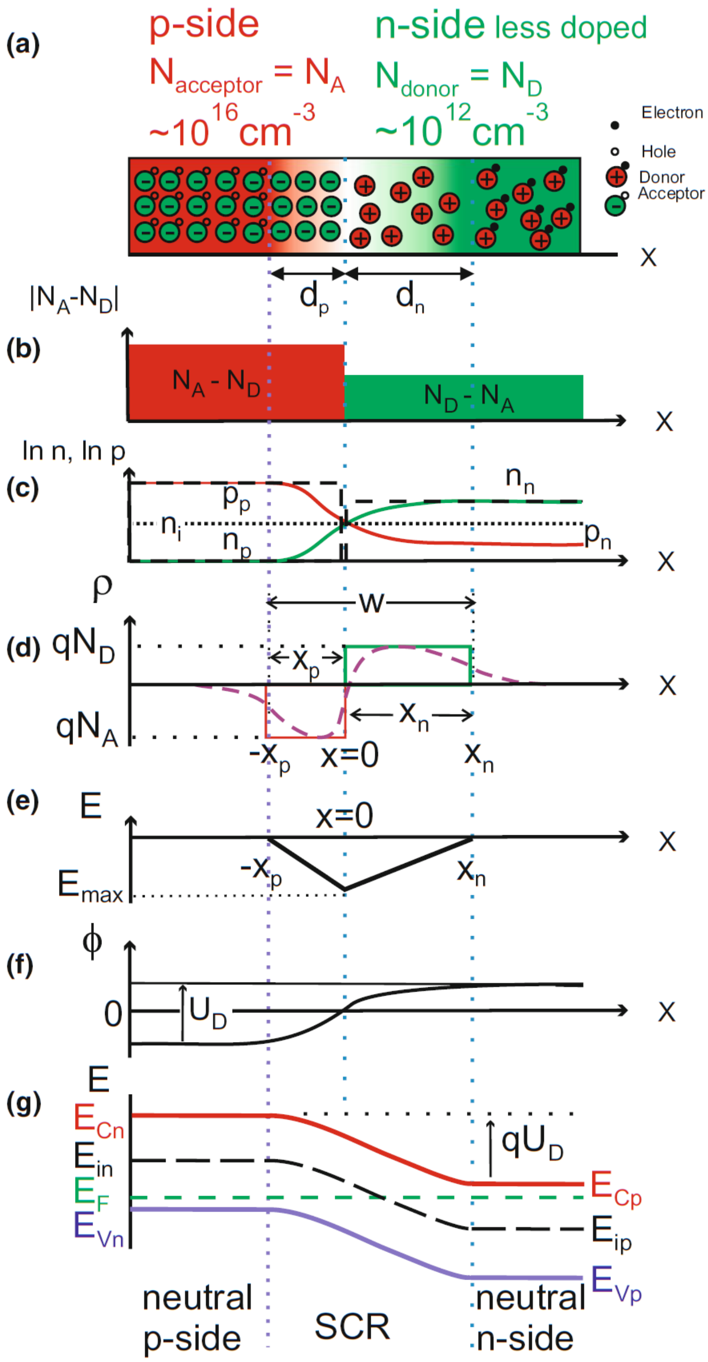


Figure 2.2.: A p-n junction: (a) Charge configuration (b) Doping profile (c) Charge carrier density (d) Space charge density (e) Electric field (f) Electric potential (g) Energy band diagram. Taken from [4].

## 2.6. Silicon particle detectors

Fundamentally, a silicon particle detector is a p-n junction in reverse bias. Electron-hole pairs created in the bulk through ionisation by a traversing particle will separate according to the applied voltage.

It is important to fully deplete the volume of a silicon sensor in order to successfully detect the signal of traversing particles. This will become clear in the following.

The energy loss of a traversing charged particle in the energy regime relevant for high energy particle physics is described by the Bethe-Bloch formula[2] [10]. It gives the mean rate of energy loss per distance travelled:

$$-\left\langle \frac{\mathrm{d}E}{\mathrm{d}x} \right\rangle = 4\pi N_A r_e^2 m_e c^2 z^2 \frac{Z}{A} \frac{1}{\beta^2} \left( \frac{1}{2} \ln \frac{2 m_e c^2 \beta^2 \gamma^2 T_{\text{max}}}{I^2} - \beta^2 - \frac{\delta(\beta\gamma)}{2} \right) \tag{2.33}$$

with the maximum transferred kinetic energy in a collision $T_{max}$, electron mass times the speed of light squared $m_e c^2$, atomic number of the material $Z$, atomic mass of the absorber $A$, the mean excitation energy $I$, the density effect correction to ionisation energy loss $\delta(\beta\gamma)$ , Avogadro's constant $N_A$, and the classical electron radius $r_e$ [11]. An example for the Bethe-Bloch formula validity range is given in Figure 2.3.

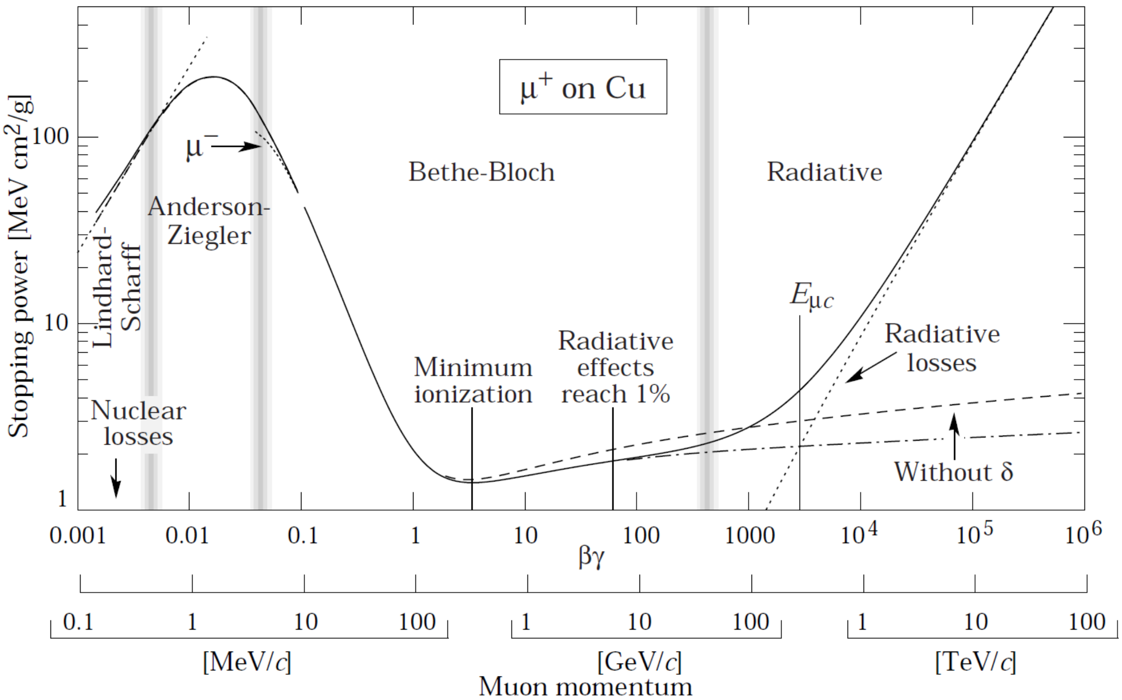


Figure 2.3.: Mean rate of energy loss (stopping power) for positive muons in copper (Cu) as a function of $\beta\gamma$. The Bethe-Bloch formula describes the region around the minimum at around $\beta\gamma = 3$, correponding to minimum ionising particles. Taken from [11].

[2] valid for $0.1 \lessapprox \beta\gamma \lessapprox 1000$

The Bethe-Bloch equation has a minimum at $\beta\gamma \approx 3$ and most relativistic particles will have mean energy loss rates close to the minimum.

The most probable value (MPV) for the energy loss lies below the mean value[3]. A traversing *minimum ionising particle* (MIP) in silicon thus most likely generates about $10^4$ electron-hole pairs in a thin 320 μm sensor.

Intrinsic silicon has a background of about $10^9$ to $10^{10}$ free charge carriers in a volume the size of a CMS pixel or strip tracker sensor. Distinguishing the small signal of a MIP from the large background noise in intrinsic silicon is impossible. Therefore the depletion of the sensor is mandatory in detector operation to reduce the free charge carriers. The alternative, cooling to very low temperatures, is impractical or unfeasible for experiments the size of CMS.

### 2.6.1. Signal induction

*Signal S* in this context is the charge induced in the electrodes due to ionisation in the sensor bulk by traversing particles. The deposited energy in a silicon detector is proportional to the number of generated electron-hole pairs. These charge carriers of charge $q$ move in the device due to the applied bias voltage. Their moving will instantaneously induce a current in the electrodes. Once they actually reach the electrode, the signal induction stops.

The induced charge $Q$ at the electrodes does not depend on space charge nor bias voltage; thus the signal found in the readout electrode is directly related to the charge generated by an ionising particle (assuming no trapping, see Section 3.5).

The *Shockley-Ramo theorem* provides a method to calculate the unique connection between $q$ and $Q$. It states that a static weighting potential $\phi_\mathrm{w}(\mathbf{x})$, which can be derived from the geometry of the sensor and solely depends on the spatial position $\mathbf{x}$, describes the translation from $q$ to $Q$:

$$Q = -q\phi_\mathrm{w}(\mathbf{x}). \tag{2.34}$$

Equivalently, the induced current $i$ in the electrode is described by the corresponding weighting field $\mathbf{E}_\mathrm{w}(\mathbf{x})$, where $\mathbf{v}$ is the drift velocity of the charge $q$:

$$i = -q\mathbf{E}_\mathrm{w}(\mathbf{x}) \cdot \mathbf{v}. \tag{2.35}$$

## 2.7. Macroscopic parameters of silicon sensors

### 2.7.1. Full depletion voltage

In Equation (2.31) the relation between an externally applied bias voltage and the width of the depleted region in the sensor was found. The full depletion voltage $V_\mathrm{dep}$ is defined as the external bias voltage which needs to be applied to deplete the full thickness $d$ of the

[3] The probability distribution of the energy loss for a particle with given $\beta$ in a thin silicon sensor is described by a straggling function, see [12, 11].

bulk of the sensor. It marks the minimum bias voltage setting at which a sensor must be operated to ensure optimal charge collection. Usually the built-in voltage $V_{\mathrm{bi}}$ is negligible for silicon particle detectors with respect to $V_{\mathrm{bias}}$.

Approximating the sensor geometry with an ideal diode, discussing the case $x_{\mathrm{n}} \gg x_{\mathrm{p}}$ and fully depleting the n-type bulk $x_{\mathrm{n}} = d$ leads to

$$w(V) \approx x_{\mathrm{n}} = d = \mathrm{const} \quad \text{for } V_{\mathrm{bias}} > V_{\mathrm{dep}}. \tag{2.36}$$

The full depletion voltage then follows directly from Equation (2.29)

$$V_{\mathrm{dep,diode}} = \frac{qN_{\mathrm{eff}}d^2}{2\epsilon\epsilon_0}. \tag{2.37}$$

It can also be expressed via resistivity using Equation (2.20)

$$V_{\mathrm{dep,\ diode}} = \frac{d^2}{2\epsilon\epsilon_0\mu\rho}. \tag{2.38}$$

$V_{\mathrm{dep}}$ is highly dependent on the sensor thickness, which is why thinner sensors are more radiation tolerant (compare Section 3.3).

### 2.7.2. Capacitance

*Capacitance* in a diode is defined as the variation of space charge $Q$ with bias voltage $V_{\mathrm{bias}}$

$$C = \frac{\mathrm{d}Q}{\mathrm{d}V_{\mathrm{bias}}}. \tag{2.39}$$

The *junction capacitance* is the dominant capacitance contribution under reverse bias conditions. It takes only the charge in the depleted region into account and thus

$$\mathrm{d}Q = qN_{\mathrm{eff}}A\,\mathrm{d}w \tag{2.40}$$

Using Equation (2.32) and Equation (2.36) the capacitance can be expressed as

$$C(V_{\mathrm{bias}}) = \frac{\mathrm{d}Q}{\mathrm{d}w}\frac{\mathrm{d}w}{\mathrm{d}V_{\mathrm{bias}}} \tag{2.41}$$

$$\begin{cases} = A\sqrt{\frac{\epsilon\epsilon_0 q|N_{\mathrm{eff}}|}{2(V_{\mathrm{bias}}+V_{\mathrm{bi}})}} & V_{\mathrm{bias}} \leq V_{\mathrm{dep}} \\ = A\sqrt{\frac{\epsilon\epsilon_0 q|N_{\mathrm{eff}}|}{2(V_{\mathrm{dep}}+V_{\mathrm{bi}})}} = \mathrm{const} & V_{\mathrm{bias}} > V_{\mathrm{dep}} \end{cases} \tag{2.42}$$

$$= \frac{\epsilon\epsilon_0 A}{w(V_{\mathrm{bias}})} \tag{2.43}$$

Capacitance-voltage (CV) curves are useful to determine the depletion voltage. Typically $1/\mathrm{C}^2$ is plotted against the bias voltage. Such a curve displays a sharp kink which coincides with $V_{\mathrm{dep}}$, see Figure 2.4.

### 2.7.3. Leakage current

The current that is measured in a semiconductor device when reverse bias is applied is called leakage current $I_{\mathrm{leak}}$. It consists of the diffusion current which is present even in an ideal diode, plus the current from electron-hole pairs which are generated at any irregularity in the semiconductor lattice. Unavoidable impurities from the manufacturing process, doping atoms, and radiation-induced impurities thus increase the leakage current.

The leakage current in a sensor can be split into two different components: The surface generation current $I_{\mathrm{surf}}$ and the bulk generation current $I_{\mathrm{bulk}}$. When the term leakage current is used in this thesis it refers to the bulk generation current.

Since generation and recombination of electron-hole pairs are in a dynamic equilibrium, the lifetime of an excited electron in the conduction band before recombination has an influence on the generation of electron-hole pairs: The shorter the generation lifetime of an electron-hole pair, the more often pairs of free charge carriers are generated. If a bias voltage is applied, these charge carriers constitute the leakage current - the more frequently they are generated, the higher the current.

The leakage current of a diode before irradiation, $I_{\mathrm{leak},0}$, can be parametrised as

$$I_{\mathrm{leak},0} = \frac{eN_{\mathrm{eff},0}wA}{2\tau_{\mathrm{L}}} \tag{2.44}$$

with electron charge $e$, initial charge carrier concentration $N_{\mathrm{eff},0}$, depletion zone width $w$, surface of the p-n interface $A$, and generation lifetime $\tau_L$.

Shockley, Read [13] and Hall [14] find for the generation lifetime $\tau_{\mathrm{L}}$

$$\tau_{\mathrm{L}} = \frac{1}{n_{\mathrm{t}}}\left(\frac{\exp\left(\frac{E_{\mathrm{t}}-E_{\mathrm{F,i}}}{k_{\mathrm{B}}T}\right)}{v_{\mathrm{tp}}\sigma_{\mathrm{p}}} + \frac{\exp\left(\frac{-(E_{\mathrm{t}}-E_{\mathrm{F,i}})}{k_{\mathrm{B}}T}\right)}{v_{\mathrm{tn}}\sigma_{\mathrm{n}}}\right). \tag{2.45}$$

with thermal velocities $v_{\mathrm{t}}$ of electrons and holes, intrinsic fermi level $E_{\mathrm{F,i}}$ and the concentration of traps in the material $n_{\mathrm{t}}$.

The minimum of $\tau_{\mathrm{L}}$ is reached for traps with energy levels $E_{\mathrm{t}}$ near the intrinsic Fermi level $E_{\mathrm{F,i}}$, close to the centre of the band gap. The concentration of *deep-level traps* $n_{\mathrm{dl}}$ thus makes up the highest contribution to the generation of charge carriers. For a deep-level trap $\frac{1}{\tau_{\mathrm{L}}} \approx \sigma v_{\mathrm{t}} n_{\mathrm{t}}$ and the leakage current can be written as

$$I_{\mathrm{leak},0} = \frac{1}{2} eN_{\mathrm{eff},0}\sigma_{\mathrm{i}} v_{\mathrm{t}} n_{\mathrm{dl}} A w. \tag{2.46}$$

Since only electron-hole pairs in the depleted region contribute, the leakage current is proportional to $w$. The expectation is therefore that the leakage current will be independent of the bias voltage for $V_{\mathrm{bias}} > V_{\mathrm{dep}}$:

$$I_{\mathrm{leak},0} \begin{cases} \propto \sqrt{V_{\mathrm{bias}}}, & V_{\mathrm{bias}} \leq V_{\mathrm{dep}} \\ \mathrm{const}, & V_{\mathrm{dep}} < V_{\mathrm{bias}}. \end{cases} \tag{2.47}$$

The temperature dependence [8] of the leakage current is

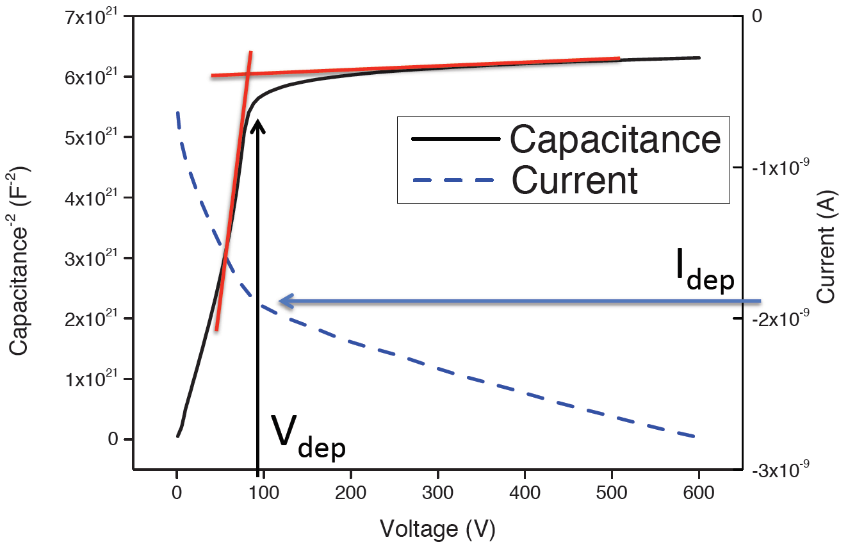


Figure 2.4.: Exemplary CV and IV curve: The CV curve displays a sharp kink which coincides with $V_{\mathrm{dep}}$. The current also rises until the volume of the sensor is fully depleted, where it reaches a plateau.

$$I(T) \propto T^2 \exp\left(-\frac{E_{\mathrm{g,eff}}}{2k_B T}\right). \tag{2.48}$$

The effective band gap $E_{\mathrm{g,eff}}$ of silicon is 1.21 eV according to [15].

### 2.7.4. Noise contributions

*Noise N* refers to charge carriers from other sources competing with the signal. In a silicon sensor the main sources for noise are the load capacitance $C_{\mathrm{load}}$ and the leakage current $I_{\mathrm{leak}}$. Other important contributions are the parallel (bias) resistance $R_{\mathrm{P}}$ and series (metal strip) resistance $R_{\mathrm{S}}$.

The Equivalent Noise Charge (ENC) is commonly used to define the signal-to-noise ratio (compare Section 4.3.5.1)

$$\mathrm{ENC} = \sqrt{\mathrm{ENC}^2_{\mathrm{C_{load}}} + \mathrm{ENC}^2_{\mathrm{I_{leak}}} + \mathrm{ENC}^2_{\mathrm{R_P}} + \mathrm{ENC}^2_{\mathrm{R_S}}}. \tag{2.49}$$

$\mathrm{ENC}_{\mathrm{C_{load}}}$ can be parametrised as $\mathrm{ENC}_{\mathrm{C_{load}}} = a + b\frac{u_{\mathrm{chip}} C_{\mathrm{d}}}{t_{\mathrm{p}}}$, depending on the peaking time $t_{\mathrm{p}}$ and intrinsic chip noise $u_{\mathrm{chip}}$. The contribution from the leakage current is called *shot noise* and depends on the peaking time, $\mathrm{ENC}_{\mathrm{I_{leak}}} \propto \sqrt{I_{\mathrm{leak}} t_{\mathrm{p}}}$. The *thermal noise* term due to parallel resistance shows the behaviour $\mathrm{ENC}_{R_{\mathrm{P}}} \propto \sqrt{T t_{\mathrm{p}}/R_{\mathrm{P}}}$. The *serial thermal noise* term $\mathrm{ENC}_{\mathrm{R_S}}$ is proportional to $\sqrt{T R_{\mathrm{S}}/t_{\mathrm{p}}}$.

In case of the LHC, where bunch crossings occur every 25 ns and readout peaking times are correspondingly short, those terms with $\frac{1}{t_{\mathrm{p}}}$ and $\sqrt{t_{\mathrm{p}}}$ dependencies have the greatest impact. Consequently the aim is to minimise leakage current (e.g. via temperature during detector operation), load capacitance (via strip length, see Equation (4.1)) and series resistance, while a high parallel resistance is desirable.

# 3. Radiation damage in silicon detectors

## 3.1. Defects and introduction mechanisms

The harsh radiation environment of the LHC has degrading effects on silicon detectors and their properties. Overviews are given e.g. in [2, 4, 16, 17, 18]. Traversing particles interact with the material through ionising and *non-ionising energy loss* (NIEL) processes.

Damage in the surface layer and the bulk of the silicon sensor are caused by different mechanisms and impact different parameters. Electronics are also affected.

### 3.1.1. Surface damage

Ionisation through photons or charged particles is the main cause of *surface damage* [19] in the $SiO_2$ layer. Ionising processes lead to the creation of electron-hole pairs. Since electrons have a higher mobility in the material, they may leave the volume via the positive electrodes, whilst holes get trapped in the $SiO_2$ layer.

Neglecting surface damage in the modelling of sensor parameters in the scope of this thesis is justified thanks to the sensor design and the high quality manufacturing process.

The impact of non-ionising interactions on the surface is negligible, since the displacement of atoms in the anyway highly irregular lattice structure of the oxide has no macroscopic consequences.

### 3.1.2. Bulk damage

The main impact on silicon sensors' macroscopic properties comes from *bulk damage*. Non-ionising processes, which can be elastic scatterings or nuclear interactions with massive particles such as neutrons, protons, or pions lead to displacement of atoms and therefore irregularities in the lattice. Essentially these irregularities are vacancies or interstitial atoms in the surrounding lattice structure, see Figure 3.1. Combinations of multiple interstitials or vacancies and also radiation-unrelated impurities are possible, leading to a rich variety of additional energy levels in the silicon band structure, see e.g. [20, 21].

The defects may change over time. For example, pairs of interstitials and vacancies (*Frenkel pairs*) may recombine. Defects may also move through the lattice or eventually interact with each other to form stable defects. This time-dependence is summarised under the term *annealing*.

The energy states in the band gap introduced by defects influence the microscopic and macroscopic parameters of the sensors. Figure 3.2 gives a simplified classification of energy levels regarding their position in the band gap and resulting effect [21].

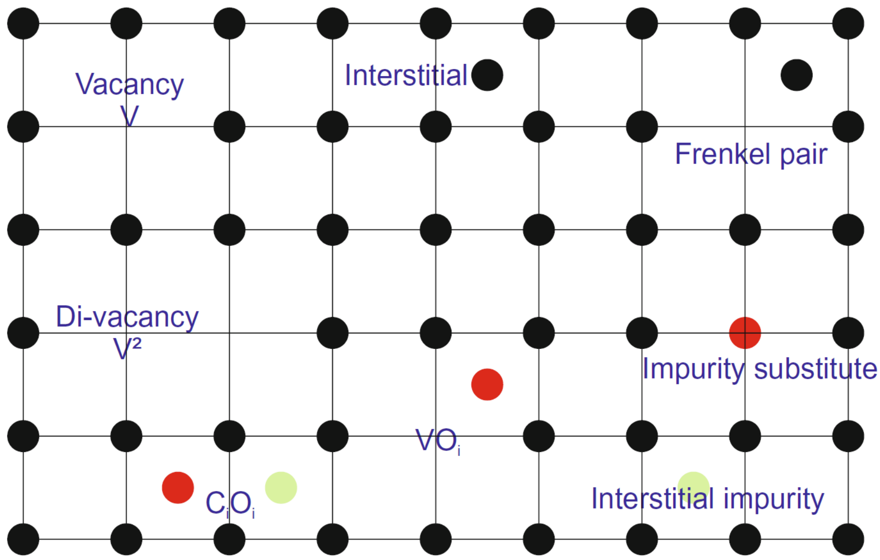


Figure 3.1.: Graphical representation of some common lattice defects. The basic building blocks are vacancies in the lattice, and interstitial atoms in-between the regular lattice positions. Complex defects are combinations of interstitials, vacancies, and impurities. Taken from [4].

- Defects with energy levels in the upper half of the band gap act as donors, while levels in the lower half of the band gap act as acceptors. In Section 3.3 the impact on the effective space charge and thus the depletion voltage is described.
- Levels close to the middle of the band gap lead to an increase in leakage current, which is described in Section 2.7.3 and Section 3.6.
- Defects with shallow energy levels act as traps for charge carriers. Trap release times can be high for low temperatures, thus signal and *charge collection efficiency* are affected. More detail is given in Section 3.4.
- Trapping further has an effect on the electric field shape, which as a consequence is no longer linear, see Section 3.5.

Seen on a larger scale, bulk damage may occur in point-like and cluster-like shapes, with probabilities depending on the particle type and energy. Neutrons interact only via the strong interaction. The *primary knock on atom* does further damage in the lattice, which leads to isolated clustered defects.

Protons and pions tend to inflict cluster damage above a transferred momentum of 5 keV, while at lower energies point defects are the more likely outcome. The lower threshold to produce a single point defect is about 25 eV [18].

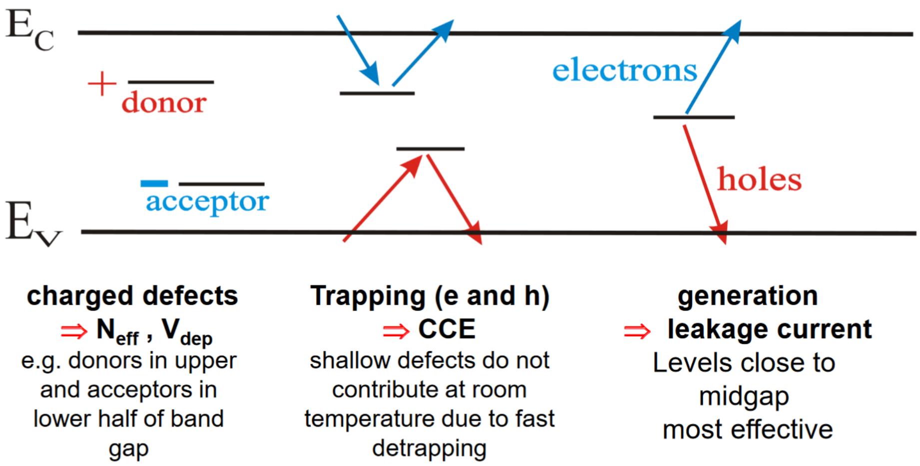


Figure 3.2.: Energy levels introduced by radiation-induced defects in the lattice influence the macroscopic parameters of the silicon sensor. Taken from [22] (after [2].

## 3.2. NIEL scaling

The displacement damage cross section $D$ describes the NIEL damage depending on the kinetic energy $E$ of the incident particle [23]

$$D(E) = \sum_{\nu} \sigma_{\nu}(E) \int_{0}^{E_{\mathrm{R,max}}} f_{\nu}(E, E_{\mathrm{R}}) \, P(E_{\mathrm{R}}) \mathrm{d}E_{\mathrm{R}}. \tag{3.1}$$

All possible interaction processes are summed over. Their cross section is denoted $\sigma_{\nu}$. $f_{\nu}$ is the probability distribution for a recoil energy $E_{\mathrm{R}}$ to be transferred during a process $\nu$. $P(E_{\mathrm{R}})$ is the Lindhard partition function [24] and describes the fraction of the recoil energy which actually ends up in atom displacement.

The maximum possible recoil energy $E_{\mathrm{R,max}}$ depends on the mass of the incident particle $m$ and its energy $E$, as well as the silicon atomic mass $m_{\mathrm{Si}}$:

$$E_{\mathrm{R,max}} = 4E \frac{m_{\mathrm{Si}} m}{(m + m_{\mathrm{Si}})^2} \tag{3.2}$$

The *NIEL hypothesis* is based on the assumption that all energy deposition is due to NIEL processes, thus independent of the particle's charge. This is not entirely true, however it remains a useful concept [25]. An important exception to NIEL scaling is discussed below. Assuming NIEL-only energy deposition, the manifestation of the damage only depends on the transferred energy. Therefore a direct comparison between different particles is possible by normalising the damage to that of a reference particle at a reference energy [23, 26]. Neutrons at $E = 1$ MeV serve as standard reference:

$$D_{\mathrm{neutron}}(E = 1\,\mathrm{MeV}) = 95\,\mathrm{MeV\,mb} \tag{3.3}$$

The resulting normalised damage functions for protons, neutrons, electrons, and pions are shown in Figure 3.3.

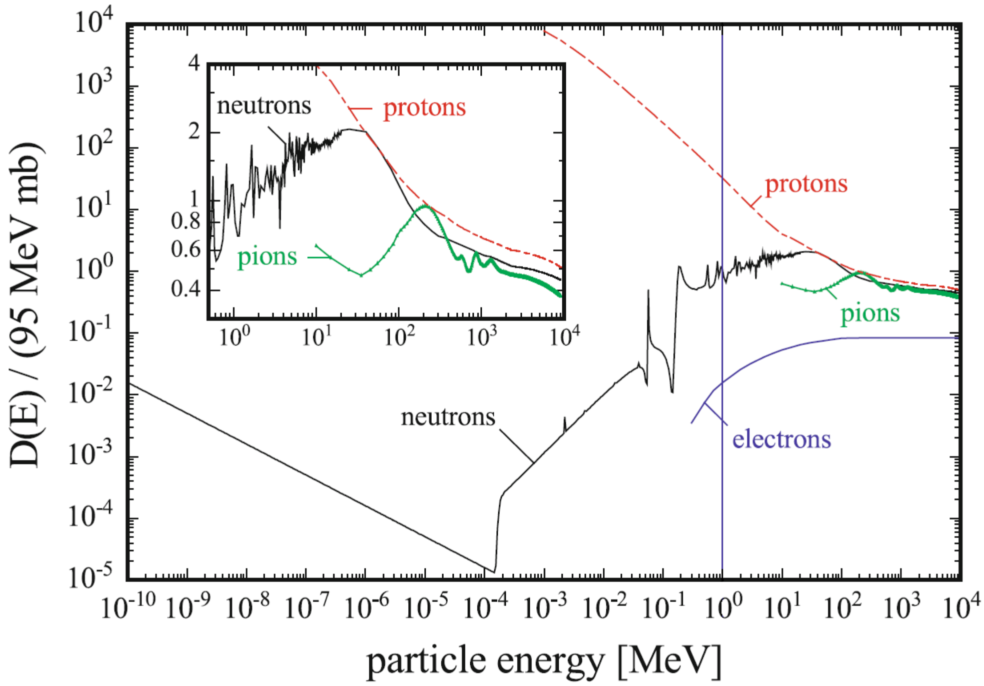


Figure 3.3.: Displacement damage functions of protons, neutrons, electrons, and pions, all normalised to the damage function of 1 MeV neutrons. The relevant energy regime for high energy physics is magnified. After [27, 2].

The fluence $\Phi = \int \phi(E)\mathrm{d}E$ of any particle type may then be translated into a fluence of exclusively 1 MeV neutrons it would take to yield the same radiation damage effect, the *1 MeV neutron equivalent fluence* $\Phi_{\mathrm{eq}}$. The corresponding unit is MeV $\mathrm{n_{eq}/cm^2}$. It is defined by weighting the energy spectrum of $\Phi(E)$ with the normalised displacement function:

$$\Phi_{\mathrm{eq}} \equiv \frac{\int D(E)\phi(E)\mathrm{d}E}{95\,\mathrm{MeV\,mb}}. \tag{3.4}$$

The scaling factor between $\Phi_{\mathrm{eq}}$ and $\Phi$ is a measure for the damage inflicted by a given radiation source and is called *hardness factor* $\kappa$

$$\kappa \equiv \frac{\int D(E)\phi(E)\mathrm{d}E}{95\,\mathrm{MeV\,mb}\,\Phi} = \frac{\Phi_{\mathrm{eq}}}{\Phi}. \tag{3.5}$$

The NIEL scaling hypothesis is not always applicable. The irradiation of oxygenated silicon for example shows a clear deviation of charged hadron damage from NIEL scaling: The observed impact on effective doping concentration is considerably lower than predicted by NIEL [28, 29, 30].

## 3.3. Hamburg model for effective doping concentration

The Hamburg model is an empirical model for the evolution of the effective space charge in irradiated silicon diodes. A change in $N_{\mathrm{eff}}$ corresponds to a change in depletion voltage, see Equation (2.37). The Hamburg model was described in [2] and has proven to be a good description for most applications up to fluences of $10^{15}$ MeV $n_{eq}/cm^2$. All numerical values listed in this section are taken from [2].

The typical fluence-, temperature- and time-dependent behaviour of the depletion voltage is visualised in Figure 3.4. Since irradiation decreases the effective doping concentration of an n-type bulk due to the introduction of new acceptor levels and donor removal, the depletion voltage first decreases with fluence. At some point the effective doping concentration changes sign and the material undergoes *type inversion*. For the type-inverted material the depletion voltage rises with irradiation.

The annealing behaviour of a sensor after irradiation can be monitored in the laboratory. Effective charge concentration changes with time and temperature: First, the radiation-induced part of $N_{\mathrm{eff}}$ decreases as radiation-introduced acceptor-like defects decay, then increases – even beyond the $N_{\mathrm{eff}}$ level directly after irradiation – as a result of additional acceptor level formation. Higher temperatures accelerate the annealing, lower temperatures slow the process down.

The Hamburg model [2] implements this annealing behaviour as three separate terms

$$N_{\mathrm{eff}} = N_{\mathrm{eff},0} + N_{\mathrm{C}}(\Phi_{\mathrm{eq}}) + N_{\mathrm{A}}(\Phi_{\mathrm{eq}}, t, T) + N_{\mathrm{Y}}(\Phi_{\mathrm{eq}}, t, T). \tag{3.6}$$

$N_{\mathrm{eff},0}$ is the initial doping concentration as described in Section 2.3. Some stable fraction of the radiation damage $N_{\mathrm{C}}$ is permanent and does not anneal. The stable damage term $N_C$ is given by

$$N_{\mathrm{C}}(\Phi_{\mathrm{eq}}) = N_{\mathrm{c},0}\left(1 - e^{-c\Phi_{\mathrm{eq}}}\right) + g_{\mathrm{c}}\Phi_{\mathrm{eq}} \tag{3.7}$$

with the donor removal constant $c$ and the acceptor creation constant $g_{\mathrm{c}}$. $N_{\mathrm{c},0}$ is the asymptotic value for complete donor removal.

The short-term annealing is parametrised as

$$N_{\mathrm{A}}\left(\Phi_{\mathrm{eq}}, t\right) = \Phi_{\mathrm{eq}} \sum_i g_{\mathrm{a,i}} \exp\left(-\frac{t}{\tau_{\mathrm{a,i}}(T)}\right) \approx \Phi_{\mathrm{eq}} g_{\mathrm{A}} \exp\left(-\frac{t}{\tau_{\mathrm{A}}}\right) \tag{3.8}$$

with damage parameter $g_{\mathrm{A}}$ and time constant

$$\frac{1}{\tau_{\mathrm{A}}} \equiv k_{\mathrm{A}} = k_{A0} \exp\left(-\frac{E_{\mathrm{A}}}{k_{\mathrm{B}} T_{\mathrm{A}}}\right). \tag{3.9}$$

where $T_{\mathrm{A}}$ is the annealing temperature. The effective band gap energy $E_{\mathrm{A}}$ is

$$E_{\mathrm{A}} = (1.09 \pm 0.03)\,\mathrm{eV}, \tag{3.10}$$

$$\text{and}\;\; k_{A0} = 2.4^{+1.2}_{-0.8} \cdot 10^{13}\,\mathrm{s}^{-1}. \tag{3.11}$$

The reverse annealing term is

$$N_{\mathrm{Y}}\left(\Phi_{\mathrm{eq}}, t\right) = N_{\mathrm{Y0}}\left(1 - \exp\left(-\frac{t}{\tau_{\mathrm{Y}}}\right)\right), \tag{3.12}$$

with

$$N_{Y0} = g_Y \Phi_{eq} \tag{3.13}$$

where $g_Y$ is the damage parameter for the reverse annealing. Again the time constants are parametrised similarly:

$$\frac{1}{\tau_Y} = k_Y = k_{Y0} \exp\left(-\frac{E_Y}{k_B T}\right) \tag{3.14}$$

$$\text{with } E_Y = 1.31\,\text{eV} \tag{3.15}$$

$$\text{and } k_{Y0} = 7.4 \cdot 10^{14}\,\text{s}^{-1}. \tag{3.16}$$

Reverse annealing was found to saturate in case of oxygenated silicon, compare Section 3.2. Different parameter sets are available for the Hamburg model and in principle they need to be newly extracted from irradiation and annealing studies for each sensor geometry.

The depletion voltage modelling in this thesis is performed by means of the Hamburg model. In order to translate the effective space charge concentration into the depletion voltage, Equation (2.37) was used. The linear relation between $|N_{\text{eff}}|$ and $V_{\text{dep}}$ in Equation (2.37) was derived assuming a linear electric field. However, after high fluences a significant change in the field configuration of a silicon sensor is observed, as will be explained in the next section. The range of validity of the application of the Hamburg model to calculate the full depletion voltage is limited to fluences below $10^{15}$ MeV $n_{eq}/cm^2$. $N_{\text{eff}}$ is still validly described by the Hamburg model after higher irradiations; however the concept of a full depletion voltage is no longer well-defined.

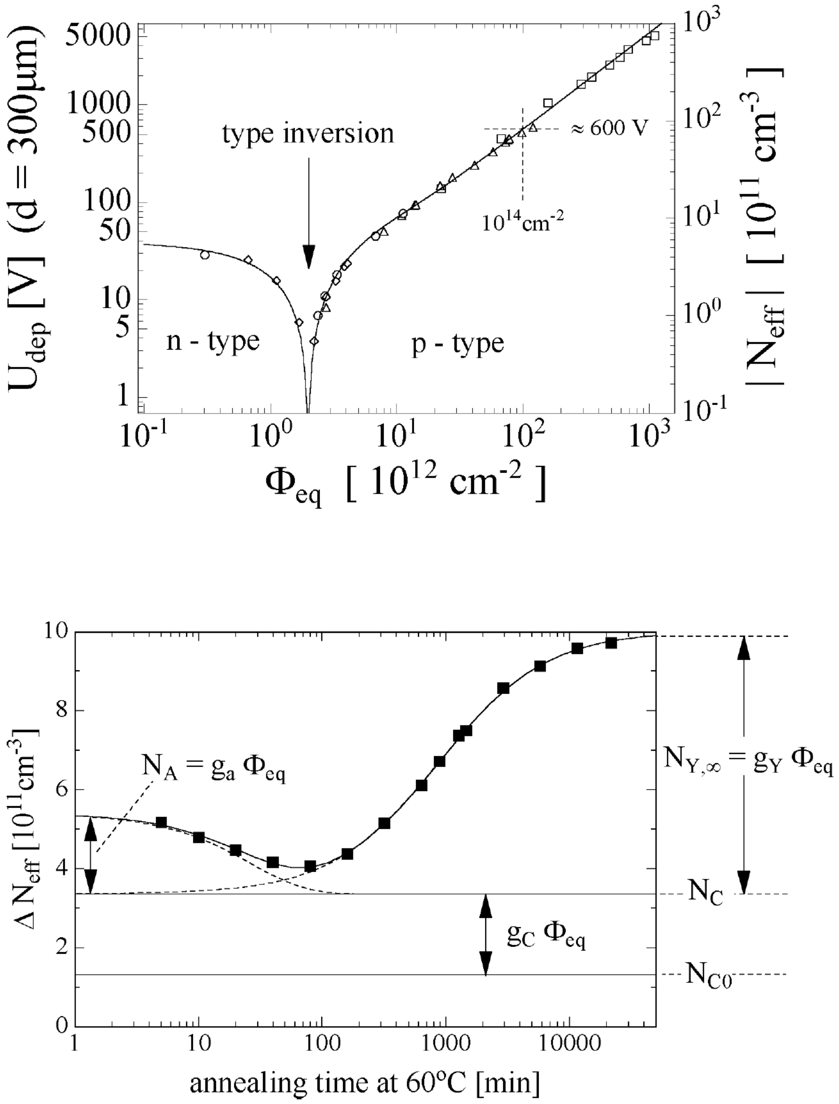


Figure 3.4.: **Top:** The change of the depletion voltage with fluence. **Bottom:** The annealing behaviour after irradiation for a fixed temperature. Short-term and reverse annealing clearly have different time constants. Not shown here: Higher temperatures lead to faster short-term and reverse annealing times. Taken from [2].

## 3.4. Trapping and charge collection efficiency

Irradiation introduces trapping centres to the material, compare Figure 3.2. Some of the generated charge from ionisation will be trapped in these centres and consequently is not "collected" at the electrodes any more, despite having an electric field throughout the bulk. The difference between the collected charge at a given bias voltage before irradiation and after irradiation is the amount of trapped charges $Q_{\text{trapped}}$. It is lost for the signal.

$$Q_{\text{trapped}} = Q_{\text{non-irrad}} - Q_{\text{irrad}} \tag{3.17}$$

The *charge collection efficiency* is a useful parameter to quantify this effect:

$$\text{CCE} = \frac{Q_{\text{irrad}}}{Q_{\text{non-irrad}}}. \tag{3.18}$$

## 3.5. Double junction

After high irradiation, the linear solution for the electric field found in Equation (2.25) holds no longer. Figure 3.5 shows the parabolic field found in the sensor after irradiation. It can be derived from *transient current technique* (TCT) studies: Time-resolved analyses of laser-induced signal currents in the sensor show a *double peak*.

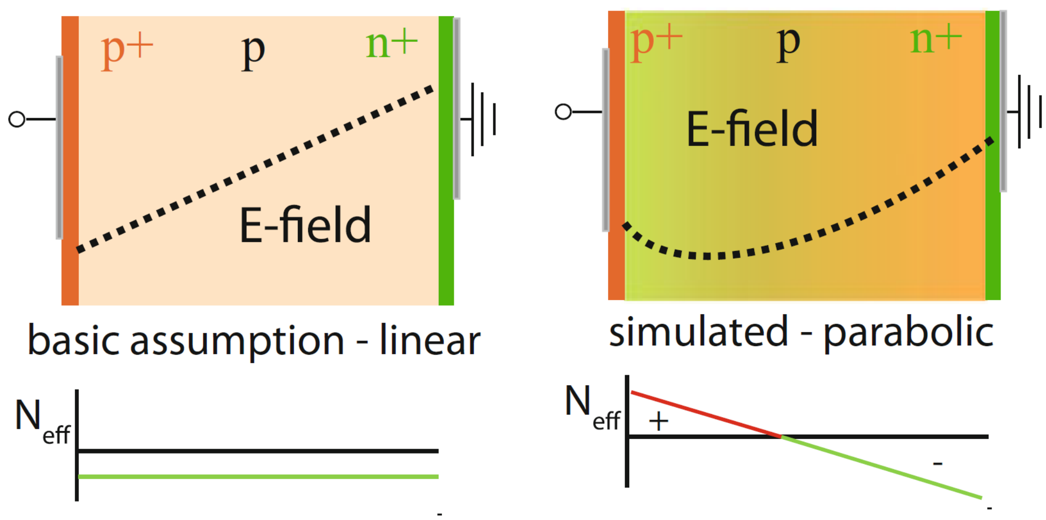


Figure 3.5.: **Left:** The linear electric field before irradiation as found in Equation (2.25). **Right:** A linear distribution of effective charge carriers due to capture of thermally produced electrons and holes in radiation-induced traps explains the parabolic electric field observed in sensors after high irradiation levels. Taken from [4].

To first order, the new field configuration may be approximated by two superimposed linear fields, corresponding to one junction on either side of the sensor (*double junction*) [4]. Yet while the defect concentration in the material is homogeneous, the field measurements show a clear asymmetry. This asymmetric field configuration can be explained by radiation-induced traps in the material. When thermal electron-hole pairs are produced, the electrons and holes move in opposite directions due to the applied bias voltage. The defects in the volume between the origin of the electron-hole pair and the positive electrode are likely to trap a traversing electron, while positive holes are more likely to be trapped in the other part of the volume. This quasi-static occupation of traps results in a distribution of effective space charge as shown in Figure 3.5 on the right, which leads to a parabolic field configuration in the sensor volume.

For a parabolic field configuration and $V_{\text{bias}} < V_{\text{dep}}$, the undepleted zone is now in the middle of the sensor. Unlike before, there are fields present even in the undepleted zone. Charges are constantly drawn from this region, increasing noise and simultaneously rendering the depletion voltage concept non-applicable.

For irradiation levels higher than $10^{15}$ MeV $\text{n}_{\text{eq}}/\text{cm}^2$, the study of parameters like CCE and signal-to-noise ratio are more meaningful for the determination of optimal detector settings. Full simulations of sensor field configurations and derivation of these parameters is currently done with the tool PixelAV [31].

## 3.6. Empirical model for leakage current

As irradiation increases, the number of radiation-induced electron-hole pair generation centres increases in the bulk. Consequently the bulk leakage current rises. A well-tested empirical parametrisation [2, 32] describes the leakage current increase $\Delta I$ depending on fluence $\Phi_{eq}$, annealing time $t$, temperature $T_{\text{A}}$ during annealing, and reference temperature $T_{\text{ref}}$

$$I(\Phi_{\text{eq}}, t, T_{\text{ref}}, T_{\text{A}}) = I_0 + \Delta I(\Phi_{\text{eq}}, t, T_{\text{ref}}, T_{\text{A}}) \tag{3.19}$$

$$\text{with} \quad \Delta I(\Phi_{\text{eq}}, t, T_{\text{ref}}, T_{\text{A}}) = \alpha(t, T_{\text{ref}}, T_{\text{A}})\Phi_{\text{eq}} V. \tag{3.20}$$

The model describes the leakage current independent of material and particle type. Fluence dependence and annealing behaviour of the leakage current are shown in Figure 3.6.

Operational temperatures are an important handle on the leakage current. Warm temperatures lead to a faster annealing (decreasing) of the leakage current in the detector, which is advantageous: Low leakage current means low noise. Further care must be taken to avoid reaching the HV power (Equation (6.1)) supply limits; here low leakage current is also desirable. During operations these limits can also be avoided by reducing temperature - thereby effectively scaling the leakage current to lower values, but at the same time slowing down the beneficial annealing.

The $\alpha$ parametrisation used for both the pixel and strip tracker leakage current calculations was taken from [2] in combination with a parameter set at $T_{\text{ref}} = 20\,^\circ\text{C}$:

$$\alpha_{20^\circ C}(t, T_{\text{A}}) = \alpha_{\text{I}} \exp\left(-\frac{t}{\tau_{\text{I}}(T_{\text{A}})}\right) + \alpha_0(T_{\text{A}}) + \beta \ln\left(\frac{t}{t_0}\right) \tag{3.21}$$

with the parameters from [2]

$$\frac{1}{\tau_{\mathrm{I}}} = k_{0\mathrm{I}} \exp\left(-\frac{E_{\mathrm{I}}}{k_{\mathrm{B}} T_{\mathrm{a}}}\right) \tag{3.22}$$

$$k_{0\mathrm{I}} = 1.2^{+5.3}_{-1.0} \cdot 10^{13}\,\mathrm{s}^{-1} \tag{3.23}$$

$$E_{\mathrm{I}} = (1.11 \pm 0.05)\,\mathrm{eV} \tag{3.24}$$

$$\alpha_{\mathrm{I}} = (1.23 \pm 0.06) \cdot 10^{-17}\,\mathrm{A/cm} \tag{3.25}$$

$$\beta = (3.07 \pm 0.18) \cdot 10^{-18}\,\mathrm{A/cm} \tag{3.26}$$

$$\alpha_0 = -(8.9 \pm 1.3) \cdot 10^{-17}\,\mathrm{A/cm} + (4.6 \pm 0.4) \cdot 10^{-14} \frac{1}{T_{\mathrm{A}}}\,\mathrm{AK/cm}. \tag{3.27}$$

Once the leakage current at $T_{\mathrm{ref}}$ is known, its value for a measurement temperature $T_{\mathrm{M}}$ can easily be calculated remembering the temperature scaling in Equation (2.48).

### 3.6.1. Self-heating and thermal runaway

A feedback loop called *self-heating* exists between the sensor temperature and the leakage current: As a result of the temperature dependence of the leakage current given in Equation (2.48), an increase in sensor temperature will entail an increase in leakage current. This increases the module power (compare Equation (6.1)), which will in turn raise the heat dissipation and may have an impact on the sensor temperature. The increase of temperature with module power is called thermal contact $\frac{\mathrm{d}T}{\mathrm{d}P}$.

Self-heating has to be counteracted by sufficiently efficient cooling. There are three possibilities:

1. The cooling is such that the loop converges and the situation stabilises with a leakage current below the threshold imposed by the power supply.
2. *Thermal runaway*: If the cooling efficiency is not good enough, the loop does not converge and temperature and leakage current keep rising. Once the leakage current is beyond the capacity of the power supply, the voltage channel trips and the corresponding modules are lost for operations. An example of a thermal runaway was observed in a strip tracker power group with a degraded cooling contact, see Figure 3.7.
3. The third scenario has the same result as the second one: If the cooling is theoretically good enough to prevent a thermal runaway but the point of equilibrium lies beyond the power supply limit, the power supply still trips.

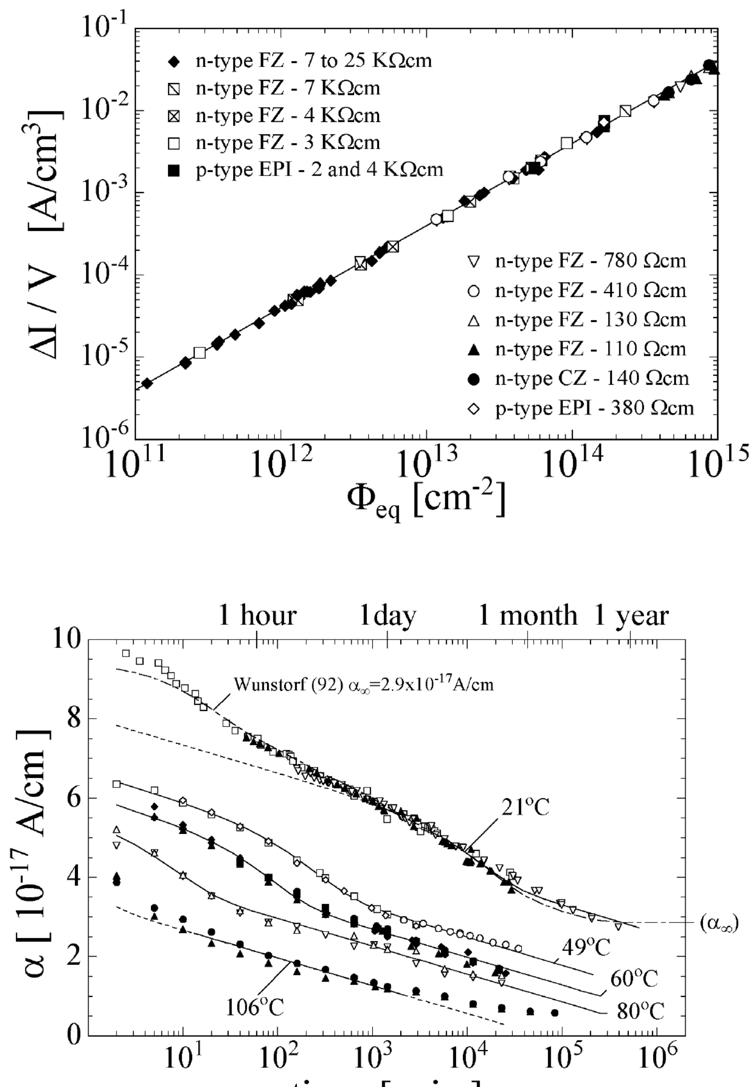


Figure 3.6.: **Top:** The change of the leakage current with fluence. **Bottom:** After irradiation the annealing behaviour, visible as a decrease in $\alpha$, depends on time and temperature. A range of temperatures between 21 °C and 106 °C was studied. Taken from [2].

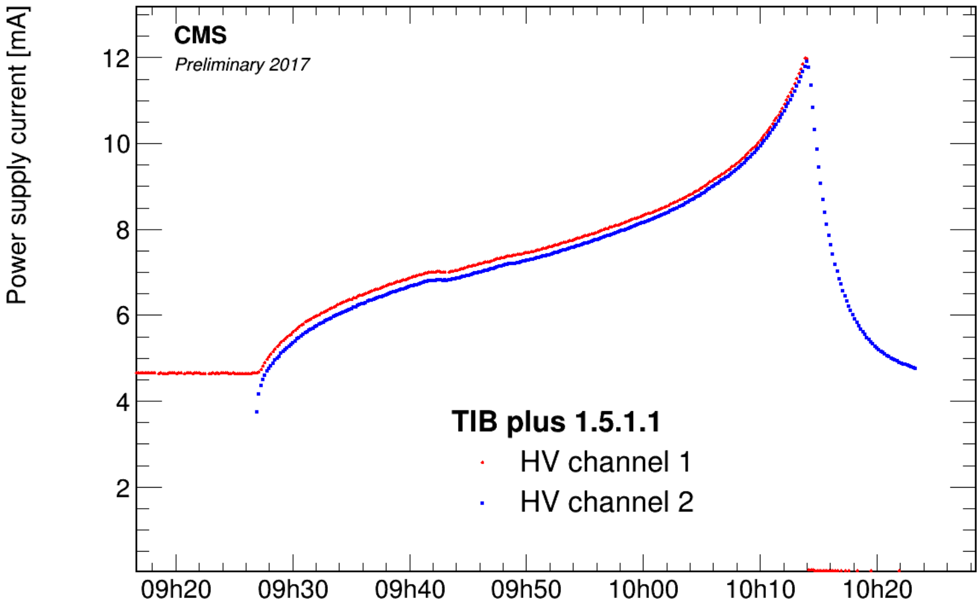


Figure 3.7.: A thermal runaway was observed for one power group (out of 2000) with a known issue of degraded cooling contact leading to high operational temperatures ($\sim 30\,°\mathrm{C}$). The combination of bad cooling contact and high radiation levels led to a point where the leakage-current-induced temperature increase of the power group could no longer be compensated by the cooling system, leading to a self-amplifying leakage current behaviour: As the HV channel 2 is switched on, the sensors of both channels started heating each other, being placed back to back. After a trip of the HV channel 1 occurred at the power supply limit, the second HV channel's current and temperature stabilised again. In order to continue operation of the channel, the bias voltage had to be lowered. Taken from [33].

# 4. The Large Hadron Collider and the CMS experiment

## 4.1. The Large Hadron Collider at CERN

The circular underground tunnel of the LHC at CERN has a circumference of 27 km. In two beam pipes, bunches of particles are accelerated in opposite directions to almost the speed of light. An overview of the accelerator complex is shown in Figure 4.1.

Primarily, the LHC is colliding protons, but about four weeks per year are dedicated to collisions of heavy ions. The protons stem from an ordinary hydrogen bottle. Electrons are stripped from the hydrogen gas atoms by means of a strong electric field in the Duoplasmatron. The remaining nuclei pass through several pre-accelerators. Electric fields in radio-frequency cavities are used for accelerating the beam and simultaneously portioning it into *bunches*. The beam energy is raised to 50 MeV in Linac 2, 1.4 GeV in the Proton Synchrotron Booster, 25 GeV in the Proton Synchrotron, and then 450 GeV in the Super Proton Synchrotron.

Finally, the proton bunches are injected into the LHC where they are accelerated to the final collision energy. After operating at 3.5 TeV and then 4.0 TeV per beam in the years between 2010 and 2013, the current energy per beam is 6.5 TeV. The design beam energy of the LHC is 7.0 TeV and is targeted after LS2.

An ultra-high vacuum of $10^{-13}$ bar is maintained inside the beam pipes to reduce interactions of the accelerated particles with molecules as much as possible.

Dipole magnets deflect the beam onto the roughly circular orbit of the accelerator. Quadrupole magnets defocus and focus the beam, thereby keeping it safely in the centre of the pipes and also providing the desired beam cross section when the beams are collided.

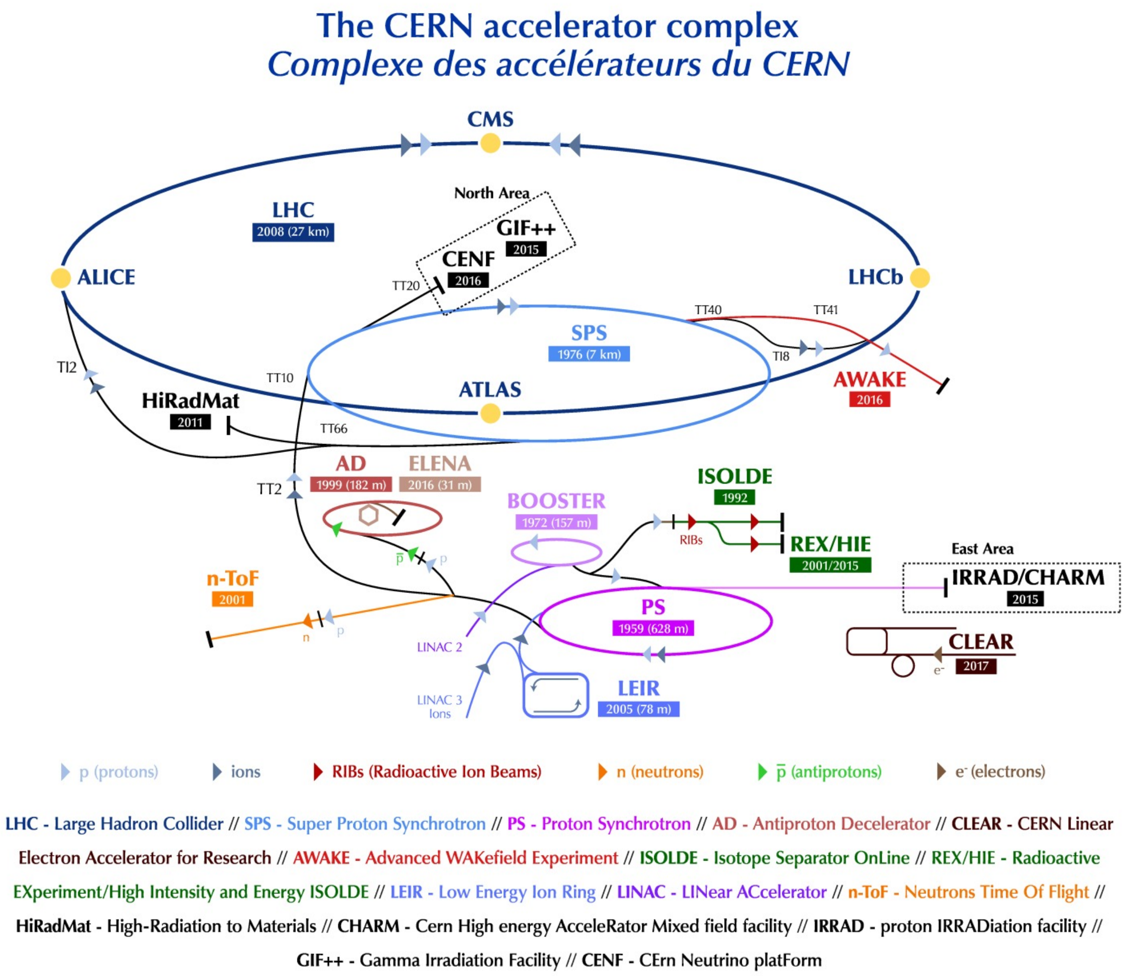


Figure 4.1.: The accelerator complex at CERN. The sketch features the pre-accelerators to the LHC, the LHC ring itself, and the four big LHC experiments ATLAS, CMS, LHCb, and ALICE. Taken from [34].

## 4.2. Experiments at the LHC

Four major experiments are placed along the ring. In their focus lies an *interaction point* (IP) each, where the two beams cross and statistically some of the protons collide. The physical processes that then take place, produce a number of outgoing particles. When traversing the detectors, they generate signals which are selectively read out and stored for further analysis. The underlying physical processes can be studied by comparing theoretical expectations with experimental observations from collision data.

Two of the four big detectors are specialised on a specific physics topic. LHCb (*b* for beauty) is examining events related to b-quarks and b-antiquarks to gain a better understanding of the asymmetry of matter over antimatter in the universe. The detector ALICE (*A Large Ion Collider Experiment*) was designed for research related to the strong interaction by recording heavy ion collisions, in which a state called quark-gluon plasma is created.

The other two big experiments however were built as versatile multi-purpose detectors: ATLAS (*A Toroidal LHC ApparatuS*) and CMS. Both collaborations are searching for signatures of yet unknown phenomena while working on increasing the measurement precision of various properties of the known Standard Model forces and particles. ATLAS and CMS had a common spotlight moment in 2012, when they announced the discovery of the Higgs boson [35, 36, 37, 38].

## 4.3. The CMS detector

The CMS detector [39] consists of different layers and was designed to be virtually hermetic. The subsystems are organised into a cylindrical barrel part placed symmetrical around the IP. A cylindrical coordinate system is used to describe the detector. The $z$ axis lies parallel to the beam pipe, with $z = 0$ marking the IP.

Endcap disks are mounted adjacent to the barrel in both plus and minus $z$ direction. The forward region is instrumented for a good pseudorapidity[1] coverage ($|\eta| \approx 5$ in case of the hadron forward calorimeter, see Section 4.3.4, and $|\eta| \approx 2.5$ in the tracker).

The various layers of CMS have different functions in the process of detecting and identifying particles that traverse the detector coming from the IP. Accurately measuring both momentum and energy of the particles is the basis for particle identification.

Particle identification and reconstruction is done by the CMS *Particle Flow* algorithm [40, 41]. It uses combined information from all subsystems.

Naming the main subsystems from outside to centre, there are the muon chambers, the solenoid magnet, the calorimeter, and finally the tracker, which is in close proximity of the beam pipe. An image of the CMS detector is given in Figure 4.2.

A short introduction of the trigger system is given in the following; the subsystems are described in more detail in the sections thereafter.

### 4.3.1. Trigger

The slots for particle bunches in the LHC currently have a 25 ns spacing, however not all of the potential slots are actually occupied by a bunch. The bunch crossing rate is 40 MHz $\cdot$ available bunch slots/occupied bunch slots. In 2018, about 50 inelastic collisions occur per bunch crossing (*pile-up*). All of the subdetectors register particles originating from these collisions through a signal that is created within an active volume (see Section 2.6.1 on signal induction in silicon detectors).

The full amount of data that is created could not possibly be read out and stored.

By any standards the events that are categorised as "interesting" for physics analysis are statistically rare and thus only make up a small part of the data. This trait is exploited by a trigger system: Across two stages the data are filtered through sophisticated decision trees

[1]Pseudorapidity $\eta = -\ln\left(\tan\left(\frac{\theta}{2}\right)\right)$ is related to the angle $\theta$ between the particle's momentum and the beam pipe.

and only a fraction of them is kept. An indication to read out and store the full detector data of an event could for example be the occurrence of a muon with a momentum above a defined threshold.

Despite the large data rate, CMS uses only two trigger levels. Instead of several hardware-based trigger levels, the single hardware trigger of CMS is the Level-1 (L1) trigger [42]. It already reduces the data rate to a peak 100 kHz based on information from the calorimeters and the muon systems. In a second step, software algorithms on a computer farm called the *High Level Trigger* (HLT) [43] further select events, thereby achieving the permanent storage rate of 1 kHz [44].

The combined data from all experiments is processed by the Tier-0 server farm. The CERN Data Centre itself hosts 11 000 servers with 100 000 processor cores [45]. From there, the data is distributed to the World Wide LHC Computing Grid for further processing, permanent storage, and analysis.

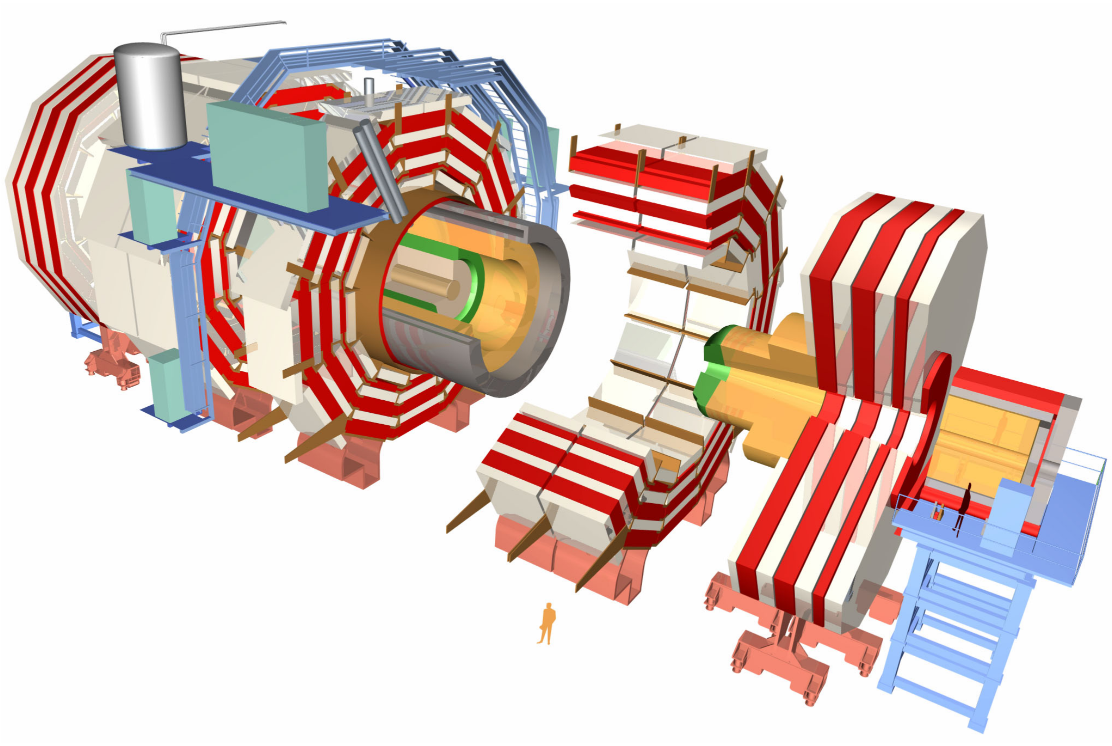

Figure 4.2.: View of the open CMS detector.

### 4.3.2. Muon chambers

The outermost layers in a typical high energy physics detector have essentially one task: detecting muons and measuring their momenta. The muon chambers of CMS [46] start in 7.4 m and end in about 4 m distance from the IP. The absorption length $\lambda$ is the distance after which all but $1/e$ of the initial particles have been stopped by a material. After the more than $10\lambda$ worth of calorimeters plus the magnet, only muons and neutrinos (or hypothetical non-Standard Model particles) are likely to have survived the traverse. Yet only the charged muons will leave a signal in the gas detectors and can thus be identified as such. For all other particles, the probability of interacting with the detector material through ionisation, nuclear interactions, bremsstrahlung, or pair production is high enough for them to be stopped before reaching the muon gas chambers.

There are three types of muon chambers used in CMS. *Drift tubes* (DT) in the barrel and *cathode strip chambers* (CSC) in the endcaps are responsible for position measurement and triggering; additionally, *resistive plate chambers* (RPC) in both barrel and endcap measure position information and can trigger the readout of the full detector data of an event.

### 4.3.3. Solenoid magnet

A charged particle's trajectory in a magnetic field will be curved due to the Lorentz force. Thus a strong magnetic field is required to allow an accurate measurement of a particle's momentum by tracking its curved path in the muon chambers and the silicon tracker.

The 3.8 T superconducting solenoid magnet [47] is the eponym of the Compact Muon Solenoid experiment. It creates a homogeneous magnetic field parallel to the beam pipe inside its volume. The magnetic field also penetrates the muon chambers both in barrel and forward region.

An important design feature is the size of the magnet's coil. It contains not only the pixel and strip tracker but also the electromagnetic and most of the hadronic calorimeter. The placement of most of the calorimeter[2] within the magnetic coil has the advantage that particles can be measured precisely in the calorimeter before they encounter the massive magnet. This way, the muon system is closer to the magnet and the particle paths are bent stronger within the muon system's volume. The return yoke of the magnet, which confines the magnetic field to the CMS detector volume, consists of massive layers of iron interleaved with the muon chambers (white in Figure 4.2).

### 4.3.4. Calorimeter

The barrel and endcap sections of the hadronic calorimeter (HCAL) [48, 49] of CMS are what is called a *sampling calorimeter*, with alternations of brass layers serving as absorber and plastic scintillator layers in-between. An additional section of the HCAL is the forward calorimeter [50], which instruments the area close to the beam pipe It is based on Cherenkov radiating quartz fibre.

The electromagnetic calorimeter (ECAL) [51] of CMS on the other hand is *homogeneous.* This means that it consists of a material that works as absorber and scintillator simultaneously. Lead tungstate crystals are used for this purpose.

Key requirement for a calorimeter is its good energy resolution. The ECAL and HCAL also have the task of measuring *jets* and *missing transverse energy*, explained in the following. Both are signatures of importance for the L1 calorimeter trigger and HLT as well as later analyses.

[2] Only the Hadronic Outer calorimeter (HO) and Hadronic Forward (HF) calorimeter are situated outside of the magnet. The task of the HO is to catch tails of hadron showers which may punch through the magnet.

Since the sum of transverse momenta before a collision is zero[3], this is also true for all outgoing particles after the collision. Neutrinos only interact via the weak force. They are therefore likely to escape the detector without generating any signal. Their presence only becomes obvious through *missing transverse energy*[4].

Elementary particles interacting via the strong force carry colour charge[5] and cannot exist individually. They will form composite particles with a net colour charge of zero called hadrons. Since the primary quark or gluon usually has a high velocity, the resulting particles all fly in a similar direction. These cones of particles are called *jet* in the detector.

### 4.3.5. The strip tracker

Another characteristic of the CMS design is the all-silicon tracking system. 206 $m^2$ of silicon have been used to build the strip tracker [4].

The amount of material must be kept as low as possible in order to reduce multiple scatterings and minimise the influence on later energy measurements in the calorimeter. The silicon sensors of the tracker are attached to a stiff and very light carbon fibre structure with good thermal conductivity. Cooling, readout fibres, and cabling are also supported by the carbon fibre.

The main task of the tracker is to record precise position information of particles. Charged particles' tracks are bent in the magnetic field and their momentum as well as the sign of the charge can be determined from the curvature.

A multitude of sensor hits is recorded for each bunch crossing and the tracking algorithms have the task of disentangling and combining them to individual particle tracks. These are subsequently used to reconstruct vertices. The two-dimensional position resolution of the strip tracker is in the order of several 10 μm [52].

The strip tracker [53, 54, 55] is structurally devided into four regions: Tracker EndCap (TEC), Tracker Inner Barrel (TIB), Tracker Inner Disks (TID), and Tracker Outer Barrel (TOB), see Figure 4.3. Their total of 10 layers and 3 plus 9 disks on each end cover the range between 22 cm and 115 cm in radius, 5.4 m in total length and a pseudorapidity region down to $|\eta| < 2.5$.

More than 20 different module designs can be found among the 15148 strip modules. Resistivity and physical dimensions are adapted to radiation exposure and overall geometry requirements. The characteristic wedge shape of the disk and endcap strip sensors reduces the overlap of modules.

Some layers and rings have double-sided stereo modules which are mounted back-to-back. The two modules are installed with a stereo angle of 100 mrad between their strip orientations. This improves the $z$ resolution. The small angle was chosen in order to keep the combinatorics of hits in the two modules at a reasonable level despite the high

[3]Even though proton or ion constituents usually have a momentum component transverse to the proton beam, at nearly the speed of light it is mostly negligible in the LHC's high energy collisions

[4]Apart from neutrinos, hypothetical long-lived neutral particles, interacting only via the weak force or some new interaction outside of the known Standard Model of Particle Physics, are a potential cause of missing transverse energy

[5]Quarks and gluons are the elementary particles which have colour charge in the Standard Model

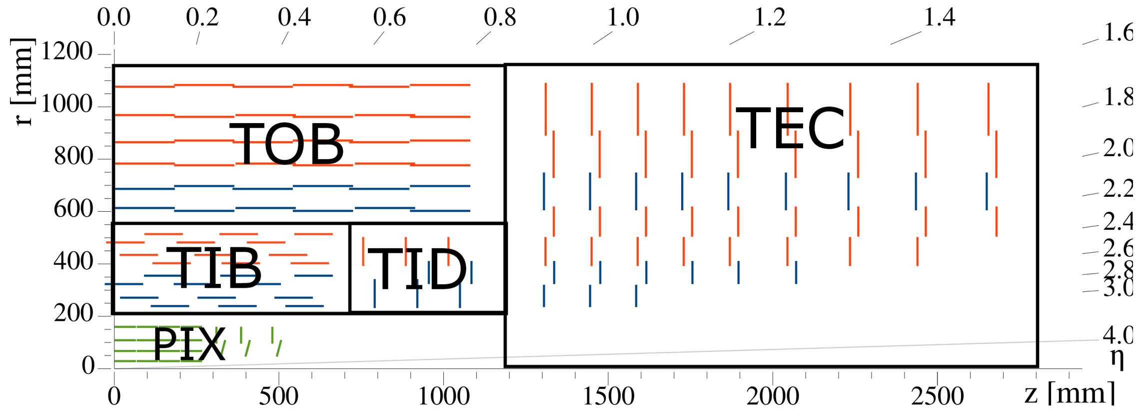


Figure 4.3.: Schematic layout of a quadrant of the CMS strip and pixel Phase-1 tracker. The pixel tracker layers and endcaps are shown in green. Strip tracker single layers are represented by red lines, double layers with stereo modules are indicated by blue lines. Adapted from [56].

occupancy in the LHC environment. Stereo layers are TIB and TOB L1 and L2, as well as rings TID R1 and R2, and TEC R1, R2, and R5 (compare Figure 4.3).

The front-end readout chips APV25 (*analogue pipeline voltage chips*), are wire-bonded to the strips. They were specially developed to cope with the short 25 ns bunch crossing intervals of the LHC. The design is radiation hard and has low noise contributions. From the APVs, the signal is further transmitted via an analogue optical link to the *front-end drivers* (FED), where it is digitised. The data amount in the strip tracker is independent of hit activity, therefore power consumption is fairly stable. Consequently the temperature environment is also stable compared with the pixel tracker, see Section 4.3.6.

Radiation damage (see Section 3.3) is the reason why the tracker is cooled down during operations and warm-up periods (which might be necessary for technical interventions) are usually kept as short as possible. However, short warm-up periods can be a tool to exploit the short-term annealing, thereby lowering the depletion voltage. Annealing is accelerated for higher temperatures and is almost fully suppressed at low temperatures ($T < 0\,°\mathrm{C}$). The short-term annealing $N_\mathrm{A}$ is beneficial for the CMS tracker; it partly reverses the radiation damage and therefore leads to a gain in depletion voltage. Contrarily the later onset of reverse annealing $N_\mathrm{Y}$ is detrimental, as the depletion voltage evolution progresses further with it.

The strip tracker is cooled by a monophase liquid cooling system. Further an active[6] thermal screen (TS) between the tracker and the ECAL keeps up a temperature gradient from -10 °C on the inside to approximately room temperature on the outside, even when the subdetectors are switched off. Both the main cooling system and the TS use $C_6F_{14}$ as cooling liquid.

[6]The thermal screen can simultaneously cool its inside while heating the outside by dedicated heating foils.

#### 4.3.5.1. CMS p-in-n AC-coupled microstrip sensor

A p-in-n microstrip design was chosen for the CMS strip tracker. The n-doped bulk comprises most of the volume of the sensor and consists of non-oxygenated *float-zone* (FZ) silicon. Float-zone refers to the growth technique of vertical zone melting. The melting is confined to a narrow zone of the material, which vertically passes through this zone. The technique results in a very pure material. Intentional introduction of impurities like oxygen may or may not be achieved by diffusion processes afterwards.

A low-resistivity material was chosen for the benefit of a high initial depletion voltage (compare Equation (2.38)), which means that type-inversion occurs later. Thus the maximum bias voltage defined by the power supply limit is reached later under irradiation (see Section 3.3 on the Hamburg model), due to the initial decrease of depletion voltage, before it starts to rise again after type-inversion.

The percentage of sensor cells simultaneously carrying a signal at any one time is called *occupancy*. A low occupancy is important for resolution of individual tracks. The strip tracker was designed to have a maximum occupancy of $1-3\ \%$. This was achieved through cell granularity. $p^+$-doped strips are implanted on the sensor front side, thereby segmenting the surface into p-n junctions for a higher granularity. The $p^+$-implants have a doping concentration much higher than that of the bulk (indicated by the $^+$). Consequently the SCR spreads further into the n-bulk under bias voltage while thin implants are sufficient to realise the full depletion of the bulk.

Bulk and strips are sealed off from the surroundings by a $SiO_2$ surface insulation layer. An aluminium readout strip is placed over each implant on top of the $SiO_2$ layer. They are capacitatively coupled to the $p^+$-strips. The distance from the centre of one implant strip to the next is called *pitch*.

Design and working principle of a microstrip sensor are sketched in Figure 4.4. In case

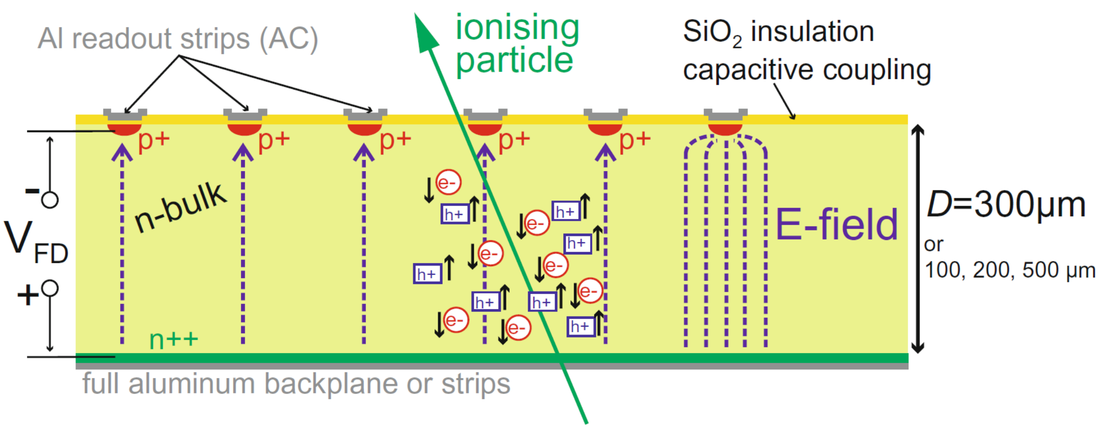


Figure 4.4.: Working principle of a p-in-n AC-coupled microstrip sensor, taken from [4]. The applied bias voltage enlarges the space charge region, which is depleted of free charge carriers, across the sensor n-bulk. Electron-hole pairs generated by traversing ionising particles are separated by the bias voltage. Transport of charge carriers towards the readout electrodes leads to a signal.

of a reverse-biased p-in-n detector, the strip implants are on ground and the $n^{++}$-backplane is on high voltage (HV) potential.

The electrons drift towards the $n^{++}$-backplane, holes drift towards the front side readout strips. The main contribution to the signal comes from holes, due to the properties of the weighting field in the sensor (see section on signal induction, Section 2.6.1).

An important parameter in the strip tracker is the signal-to-noise ratio $\frac{S}{N}$. It is crucial to optimise $\frac{S}{N}$ to yield the purest possible data.

Due to trapping (Section 3.4), signal decreases after irradiation. An increase of noise (defined in Equation (2.49)) is mainly driven by the increase in leakage current described in Section 3.6. Surface damage increases the load capacitance, which also results in higher noise levels. Overall, the signal-to-noise ratio decreases under irradiation due to decreasing signal on the one hand and rising noise contributions on the other hand. This must be taken into consideration during the sensor design phase. A signal-to-noise ratio of 10:1 at the end of life, after irradiation, was one of the design requirements of the strip tracker [53]. To some extent noise is unavoidable, but design parameters and operational settings can be chosen to minimise it.

In case of the strip tracker the total (load) capacitance is approximately a function of the width-over-pitch ratio due to a subtle interplay between interstrip and backplane capacitance [54]. It may be parametrised as

$$C_{\text{load}} = C_{\text{inter-strip}} + C_{\text{backplane}} = \left(0.83 + 1.67\frac{w}{p}\right) \text{ pF per cm strip length.} \tag{4.1}$$

making strip length an important design parameter of a sensor [4]. Direct consequence of the maximum occupancy goal of $1 - 3\ \%$ are the strip lengths, which range from 8.5 to 20.2 cm [55].

Sensors with smaller strip lengths have lower noise contributions from $C_{\text{load}}$ (compare Equation (4.1)). To meet the requirement of a good signal-to-noise ratio, the smaller signal yield of a thinner sensor (shorter tracks, thus less deposited charge) is sufficient. The radiation dose closer to the beam pipe commands the use of thinner 320 µm sensors (TIB, TID, and TEC R1-4). They are more radiation tolerant due to $V_{\text{dep}} \propto d^2$, compare Equation (2.37).

At higher radii, occupancy goals can be met with larger strip lengths, which are less expensive. This entails higher noise and therefore thicker 500 µm sensors with larger signal have to be used in TOB and TEC R5-7.

### 4.3.6. The pixel tracker

2 $m^2$ of silicon have been used to build the pixel tracker. Radiation-induced damage from charged hadrons was found to saturate in oxygenated silicon, as described in Section 3.2. This trait is exploited in the CMS pixel tracker, where charged hadron fluence is high; the sensors have an n-doped *diffused-oxygenated float-zone* (DOFZ) silicon *bulk* and $n^+$-doped implants.

At the low radii of the pixel tracker, where particle tracks are much denser than in the strip tracker, a higher granularity of detector cells is necessary to keep the occupancy low;

The goal was to stay below 1 % occupancy. Pixel instead of strip sensors are needed here. Position resultion in the pixel tracker is $\lesssim$ 10 µm.

Due to the high granularity, wire-bonding to a readout chip was not an option. Instead, readout chips (ROC) of the same geometry are placed on the front side of the pixel sensor. Each of the pixel cells is connected to a readout channel on this chip via small metal dots, the *bump bonds*. In the ROCs, *zero-suppression* is applied: Only hits with a signal above a defined threshold are kept. The signal is amplified and then stored on the edge of the chip until the trigger confirms further processing. The digital activity in the pixel tracker, and consequently the temperature, depends on hit activity.

In the Phase-0 detector, 1440 pixel modules had equipped the then three barrel layers (BPIX) and two forward disks (FPIX); when upgrading to Phase-1, the number was increased to 1632 modules. During Phase-0, the barrel had 3 barrel layers at $r$ = 4.4, 7.3, and 10.2 cm and 2 forward disks on each side of the barrel at $z$ = ±34.5 and $z$ = ±46.5.

The currently installed four layers of the Phase-1 pixel barrel span the range between 3 cm and 16 cm in radius and $z$ = ±27.4 cm along the beam pipe. Adjacent to the barrel cylinder are the three Phase-1 disks in the forward regions up to $z$ = ±51.6 cm.

The cooling of the pixel tracker was achieved with perfluorohexane ($C_6F_{14}$) during Phase-0, but has been changed to a two-phase cooling with $CO_2$ for Phase-1. The Phase-0 modules were attached to the carbon fibre support structure with silicon nitride base strips; the same mechanical layout was applied for the Phase-1 layers 2-4. The Phase-1 L1 modules are directly attached to the carbon fibre structure with thermal paste, thereby achieving better cooling efficiency.

#### 4.3.6.1. CMS n-in-n hybrid active pixel sensor

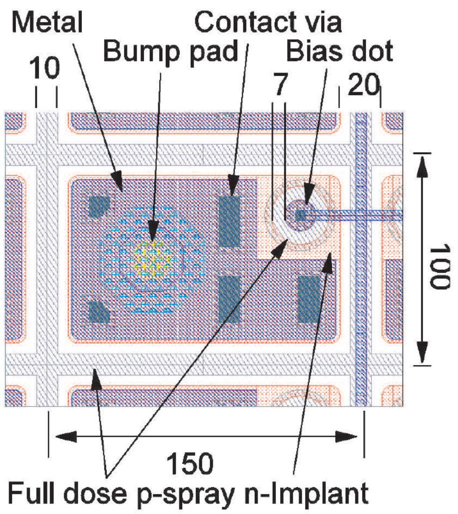


Figure 4.5.: Pixel cell close-up. The design choice fell upon diffused-oxygenated float-zone silicon [28]. Visible are the $n^{++}$-implants and bump pads. p-spray isolation increases the resistivity between neighbouring cells. Taken from [57].

An n-in-n Hybrid Active Pixel Sensor (HAPS) design has been chosen for the pixel tracker. The technology is comparable to microstrip sensors with an increased density of cells. Both Phase-0 [53, 58] and Phase-1 [59] pixel cells have a $(100 \times 150)\ \mu m^2$ surface and a thickness of 285 μm. The layout of a CMS pixel is shown in Figure 4.5.

A full pixel sensor consists of 66560 pixel cells and is read out by $2 \times 8$ Readout chips, as shown in Figure 4.6. The sensor is bump-bonded back-to-back with the ROCs. The ROCs are glued to silicon nitride base strips, which in turn are screwed onto the support structure [60]. The HDI (high density interconnect), TBM (token bit manager), and SMD (surface mount device) component also depicted in Figure 4.6 are all part of the readout structure.

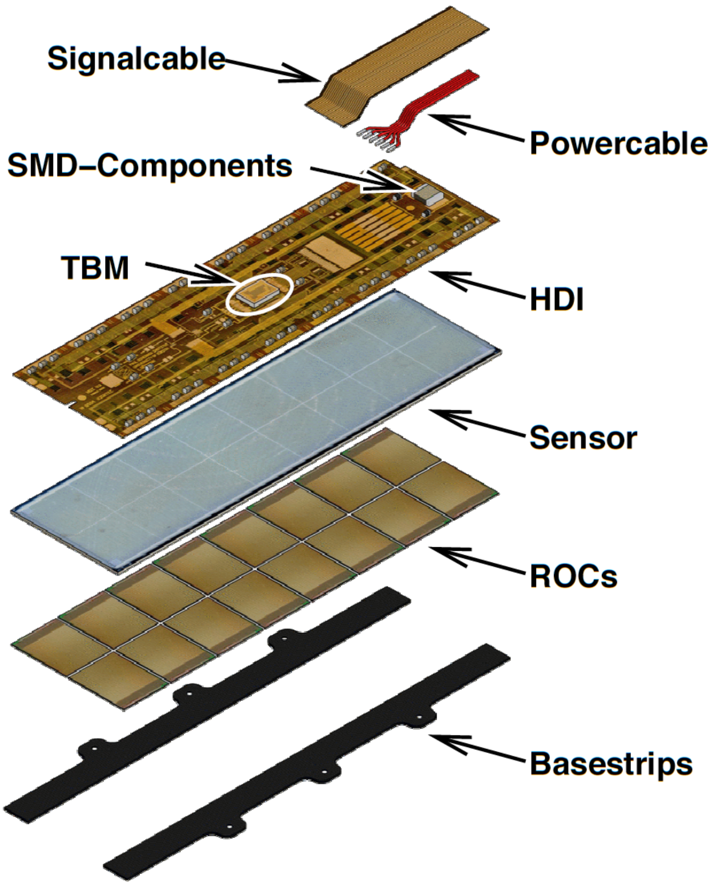


Figure 4.6.: Pixel module transect, taken from [61].

# 5. Modelling of the CMS strip tracker leakage current and depletion voltage

## 5.1. Foundations and previous results

The following chapter ties in with the 2013 dissertation of Christian Barth [1]. His work yielded insights, methods, and results concerning the modelling of strip tracker macroscopic parameters. The modelling tool described in [1] was adjusted in order to update the strip tracker results. Previous results include i.a. the prediction of leakage current, depletion voltage and expected number of thermal runaways in the strip tracker after 400 $fb^{-1}$ on a per module basis or per high voltage (HV) group[1].

Since both the $V_{dep}$ and $I_{leak}$ models depend on parameters like temperature and fluence, which constantly change in the LHC environment, a step-by-step calculation is performed. The principle is illustrated in Figure 5.1.

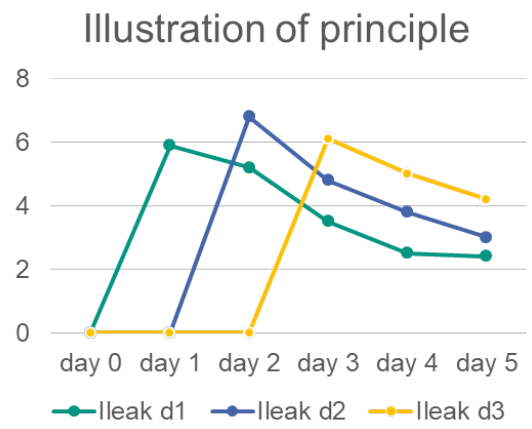


Figure 5.1.: Illustration of the underlying principle of the modelling tool: A step-by-step calculation of radiation damage impact on depletion voltage or leakage current is performed. Taken from [62].

For each time segment the radiation impact on the parameter in question is calculated. For the leakage current, the model described in Section 3.6 is used, and the depletion voltage was obtained from the Hamburg model according to Section 3.3. Annealing calculations are performed for each day's radiation damage separately and eventually the results are superimposed.

[1]One HV group contains several modules.

## 5.2. Input parameters for the strip tracker modelling

The input for the strip tracker script remained largely the same as in [1]. The tool was extended to include the year 2023. Five day periods are the base time blocks for the computing-intense calculations for all modules of the strip tracker. This time granularity is sufficient, as the temperature environment in the strip tracker is quite stable, see Section 4.3.5.

A strip specific Hamburg parameter set [1, 63] is used for the calculation of the depletion voltage. The leakage current parameters were given in Section 3.6.

### 5.2.1. Fluence

Sophisticated simulations of the detector geometry, material, and resulting radiation distribution in the CMS detector are performed by the BRIL (*CMS Beam Radiation Instrumentation and Luminosity*) RS (*Radiation Simulation*) group. The fluence input for this thesis was obtained from FLUKA [64, 65], a fully integrated Monte Carlo simulation package.

A FLUKA simulation of the fluence at 7 TeV beam energy is used (CMS FLUKA study v.3.9.0.0). It is scaled to the other beam energies via the proton-proton crosssection. NIEL scaling is approximately valid for non-oxygenated silicon, and contributions from charged and neutral particles do not require separate treatment as in the pixel tracker.

The $(r, z)$ position of each module's centre in the cylindrical coordinate system of the experiment is used to extract the corresponding bin entry from the FLUKA matrix. As CMS is mostly symmetric in $\varphi$, the FLUKA results are averaged in this regard.

### 5.2.2. Delivered integrated luminosity

The delivered integrated luminosity since 2010 will be ~190 $\text{fb}^{-1}$ by the end of Run 2. A scenario for a total 500 $\text{fb}^{-1}$ integrated luminosity by the end of Run 3, shown in Figure 5.2, is assumed for the 2023 predictions in this chapter. This is consistent with the current prognosis of an integrated luminosity of 300 $\text{fb}^{-1}$ in Run 3. Predictions of the modelling tool for 600 $\text{fb}^{-1}$ after Run 3 can be found in Appendix A.3.

### 5.2.3. Numerical correction to depletion voltage for strip geometry

The diode approximation, which was used in Section 2.7.1 to obtain $V_{\text{dep}}$ from $N_{\text{eff}}$ via Equation (2.37), is not accurate enough for a sensor with strip geometry; the finite pitch $p$ and width $w$ of the strip implants change the electric field in the sensor compared to a diode, and thus influence the depletion voltage.

The increase in depletion voltage for an AC-coupled junction-side microstrip detector has been derived in [66] to be

$$V_{\text{dep,strip}} = V_{\text{dep,diode}} \left(1 + \frac{p}{\pi d} \frac{\epsilon}{\epsilon + 1} A_0 \left(\frac{w}{p}\right)\right) \tag{5.1}$$

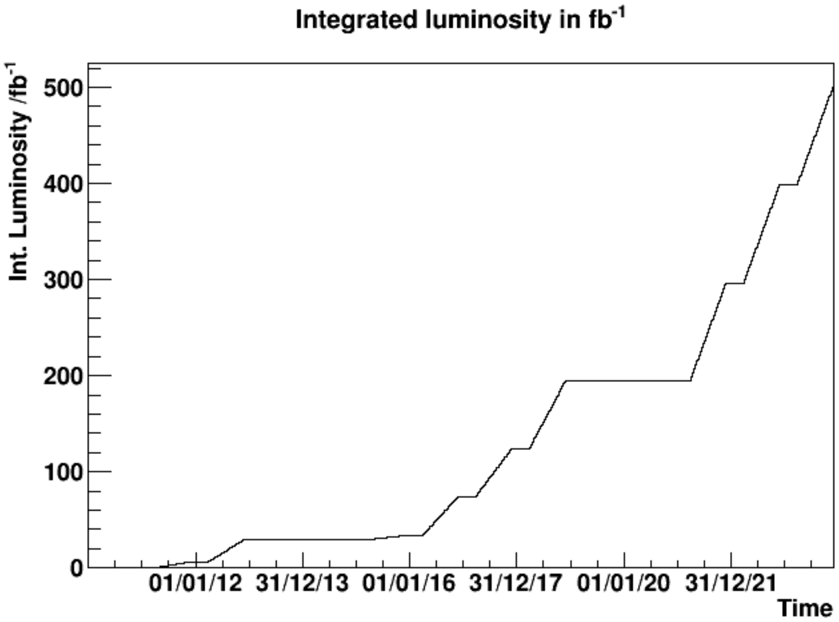


Figure 5.2.: The integrated luminosity scenario which served as an input for the strip tracker parameter predictions of Section 5.4. A delivered integrated luminosity of 100 $\mathrm{fb}^{-1}$ was assumed for each year in Run 3.

where

$$A_0\left(\frac{w}{p}\right) = \frac{\sqrt{2}}{\pi}\int_0^{\pi\left(1-\frac{w}{p}\right)} \frac{x \sin\frac{1}{2}x}{\sqrt{\cos x + \cos \pi\frac{w}{p}}}\mathrm{d}x \tag{5.2}$$

is a constant defined by the detector geometry.

In the calculation of the strip sensors' depletion voltage, the value $\frac{w}{p} = 0.25$ is used. For a sensor of thickness $d = 320$ µm, the geometry correction is a $\sim$ 23 % effect. For thicker 500 µm sensors, the increase is still 15 % compared to $V_{\mathrm{dep,diode}}$.

### 5.2.4. Tracker maps and temperature distribution in the strip tracker

Parameter distributions in the strip tracker, for which a per-module or per-HV group resolution is of interest, are typically visualised by means of a *tracker map*. An example is given in Figure 5.3. It shows a typical temperature distribution in the strip tracker, measured during Run 2.

A schematic layout of the strip tracker with the subdetectors TIB, TOB, TEC, and TID was given in Figure 4.3. The rectangles in the centre of the tracker map correspond to one layer of the barrel region each, unfolded into a flat shape. Starting from TIB L1 on the bottom left, which directly surrounds the pixel tracker, increasing layer numbers correspond to increasing radius. The endcaps and disks (D) are projected onto a circlet area. Numbering of their rings (R) – although not shown in Figure 5.3 – starts from inner rings and increases towards higher radii. Plus + and minus - indicate the $z$ position with respect to the IP.

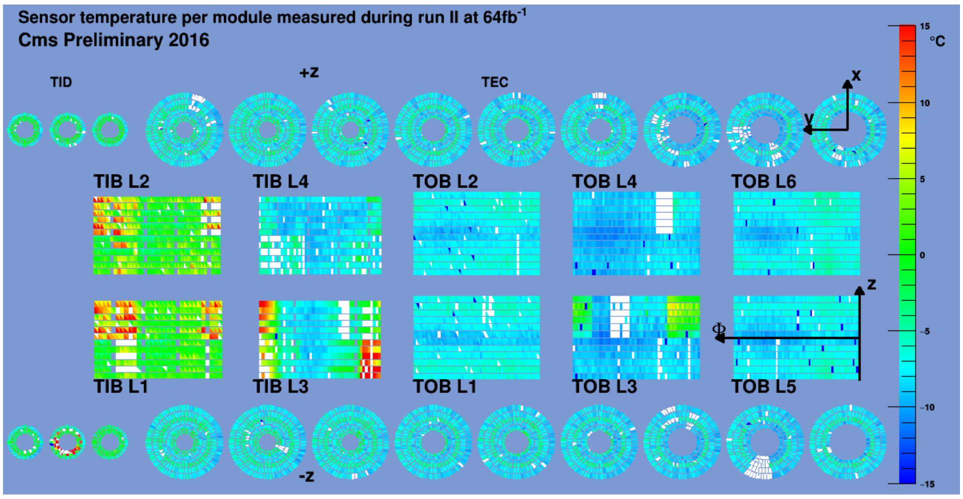


Figure 5.3.: Tracker map of the temperature distribution in the strip tracker. Visible features are explained in Section 5.2.4.

The white spots occur where information is missing. Reasons are either the failing readout as in TOB L4, TIB L1-4 and TEC or unstable control chain circuits, where *detector control unit* (DCU) readings are unavailable. Parts in TOB L3, TID- D2, TIB L3, and TIB L3 are only passively cooled by surrounding modules. Some parts in the detector have degraded cooling contacts. This explains the warm spots in TIB L1 and TIB L2. Since it is more difficult to cool the double modules with twice the power dissipation and worse cooling contacts, layers featuring stereo modules tend to be warmer (TIB L1 and 2, TOB L1 and 2, TID R1 and 2, TEC R1, R2, and R5). The temperature patterns will also be visible in the depletion voltage and leakage current in the following sections.

From 2010 until 2012, the cooling plant ran at 4 °C. After LS1, the cooling temperature was lowered to −15 °C, then further lowered to −20 °C after YETS 17/18. Depending on detector parameters, a cooling set point between −20 °C and −25 °C is considered a viable future option for Run 3. The lower limit is −25 °C, the minimum achievable temperature by the cooling plant.

Thermal contacts $\frac{\mathrm{d}T}{\mathrm{d}P}$ (compare Section 3.6.1) have been extracted for each individual module [1]. Since $V_{\mathrm{bias}}$, $I_{\mathrm{leak}}$, and $T_{\mathrm{sil}}$ are constantly monitored in the strip tracker, correlating power and temperature allows the calculation of $\frac{\mathrm{d}P}{\mathrm{d}T}$:

$$V_{\mathrm{bias}} I_{\mathrm{leak}} = P = \frac{\mathrm{d}P}{\mathrm{d}T} T_{\mathrm{sil}} \tag{5.3}$$

Occasional missing measurement information was replaced in the tool by a suitable thermal contact value comparable to those of the surrounding modules.

The procedure to obtain the temperature input for the modelling of the leakage current and depletion voltage in the strip tracker is described in the following.

- For each module, a reference temperature measurement serves as a starting point for the calcuation. This reference measurement has been taken with the cooling set point at +4 °C.
- A simplified temperature scenario is assumed, mimicking the cooling set points during operation. Future scenarios of the years after LS2 were based on the available schedule of the LHC Programme Coordination. In the future, 120 days at a room temperature of $RT = 20\,°C$ are budgeted for, otherwise temperatures are assumed at 0 °C for LS2 and all YETS.
- For each individual module, the offset between the reference module temperature measurement and the cooling set point at the time of the measurement, 4 °C, is propagated to each subsequent cooling set point, to obtain a base temperature scenario.
- An implementation of the self-heating loop described in Section 3.6.1 takes care of the module's temperature- and leakage current increase under irradiation. It makes use of the $\frac{dT}{dP}$ measurements described above.

The resulting temperature evolution of one example module, as calculated by the modelling tool, is shown in Figure 5.4.

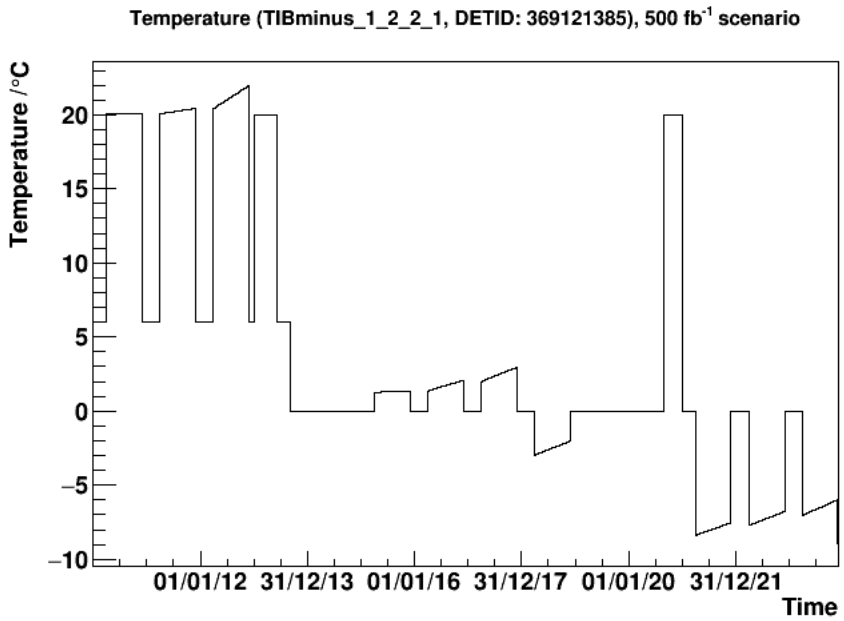


Figure 5.4.: Exemplary temperature evolution of a representative TIB L1 module until the end of 2023, as calculated by the modelling tool. The impact of self-heating is visible in the rising temperatures during operation periods.

## 5.3. Comparison with data: Depletion voltage drop

After resuming work with the strip tracker tool and successfully reproducing previous results, further cross-checks with data were made.

While CV curves are used to determine the full depletion voltage during R&D sensor characterisation, it is not possible to measure capacitances of the CMS silicon sensors during detector operation. Other macroscopic parameters are expected to saturate for bias voltages above $V_{\text{dep}}$:

*Cluster width*, or *Cluster size* (CS) for pixels, is the total number of cells which share the charge collection from one track.

*Cluster charge* (CC) is the amount of charge deposited in the sensor. It depends on the track length in the sensor, to which it is consequently normalised. The track length differences are corrected by normalising the charge to the shortest possible track length (perpendicular to the sensor).

Depletion voltage data points are obtained from HV bias scans, during which the bias voltage is varied stepwise. Two kinds of signal bias scans exist in the strip tracker: Once per month, a small bias scan is performed, which can be done parasitically during data-taking, since only a small subset of the power supply units (PSU) is participating. Full scans need dedicated time slots and are performed twice per year.

Detector data is subsequently analysed to obtain the variables cluster width and cluster charge. An exemplary cluster width distribution with the rising flank and a plateau is shown in Figure 5.5. The kink position marks the bias voltage of what is interpreted as the depletion voltage. An algorithm for the extraction of the kink position had already been developped by the strip tracker community. Figure 5.5 features an example of the linear fitting method.

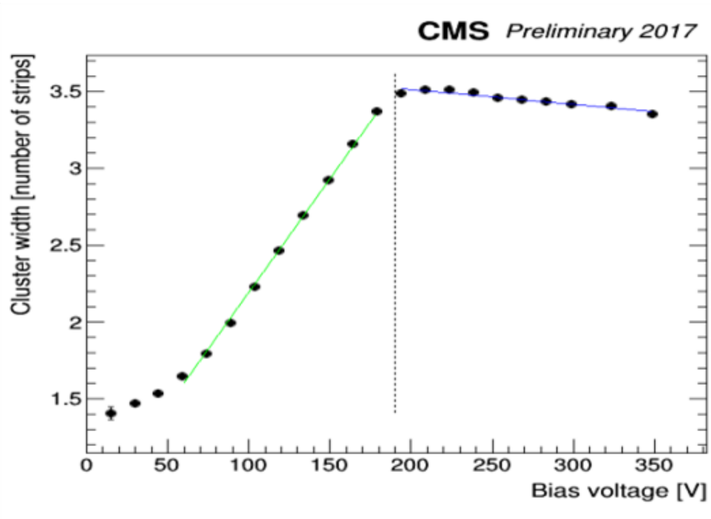


Figure 5.5.: Example of the linear fit algorithm to cluster width data from HV bias scans. The aim is to extract the full depletion voltage which marks the point at which the variable saturates. Taken from [33].

A recent compilation of the bias scan results yielded the evolution of the full depletion voltage of each layer in the strip tracker. In order to anchor the modelling results to current data, the depletion voltage drop with fluence was simulated and compared with the already available data plot. Both are juxtaposed in Figure 5.6. The data points follow a slight up-and-down modulation from one scan to the next. This is caused by annealing behaviour during the YETS and visible in the start-of-year scans, while the depletion voltage in the mid-year scans after irradiation tends to be higher.

The depletion voltage evolution is very similar in the data and the simulation. In both cases the thicker TOB sensors with $d = 500\,\mu\text{m}$ show a steeper slope in the drop of depletion voltage compared to the 320 µm TIB sensors due to $V_{\text{dep}} \propto d^2$ (compare Equation (2.37)). The thicker modules will undergo type-inversion first.

The comparison confirms the reliability of the modelling tool for the strip tracker in terms of depletion voltage.

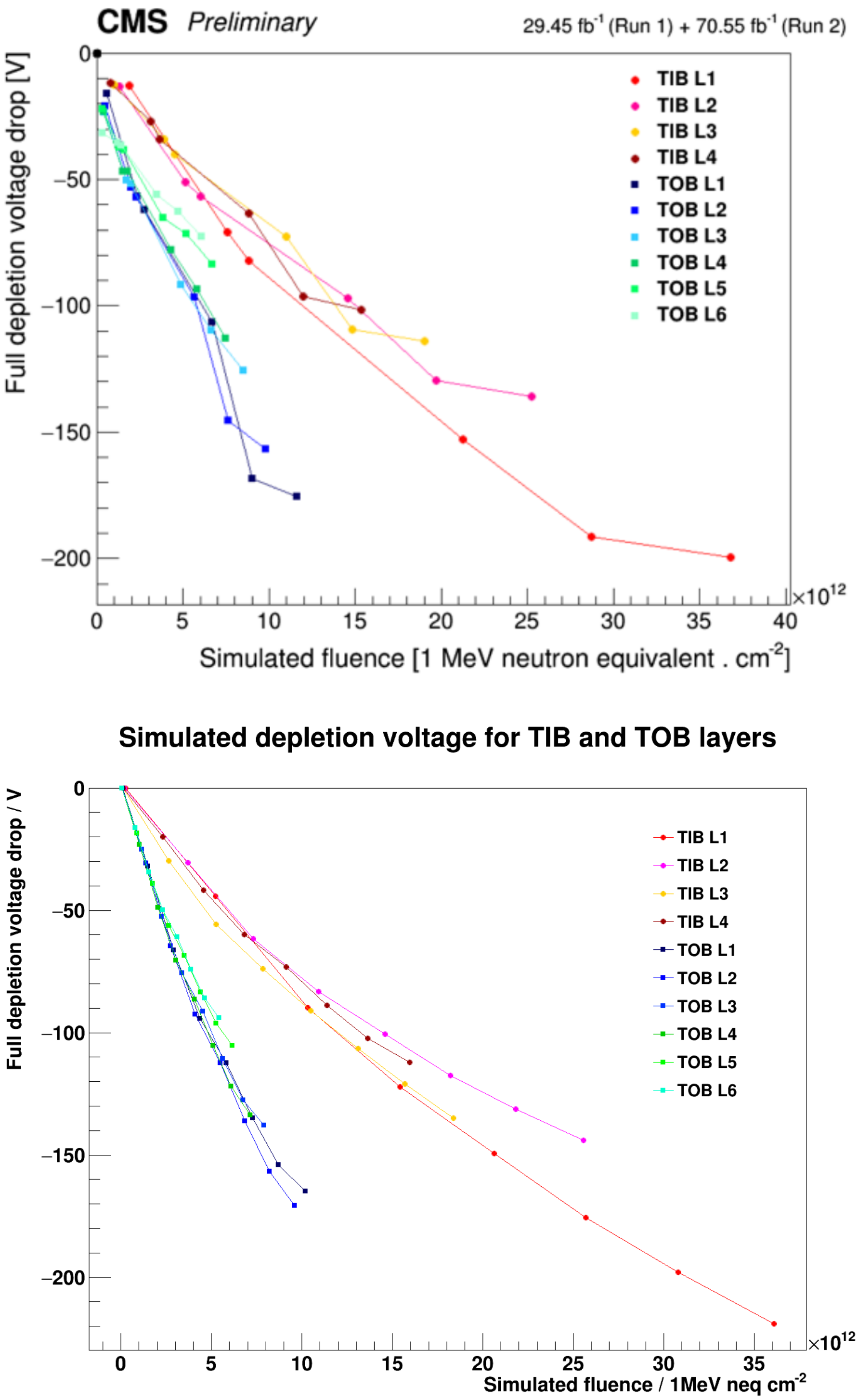


Figure 5.6.: **Top**: Data from bi-yearly full scans up to April 2018 was averaged for each of the TIB and TOB layers. Fluence was calculated from FLUKA simulations and delivered integrated luminosity. Reference values of the initial depletion voltage are from laboratory measurements. **Bottom**: Modules with representative temperature histories in TIB and TOB were chosen and their depletion voltage evolution modelled up to similar fluences.

## 5.4. Future projections

### 5.4.1. Strip tracker depletion voltage after Run 3

Based on the input parameters described in the previous sections, the depletion voltage was modelled. The resulting tracker map with projected depletion voltages after an integrated luminosity of 500 $fb^{-1}$ is shown in Figure 5.7.

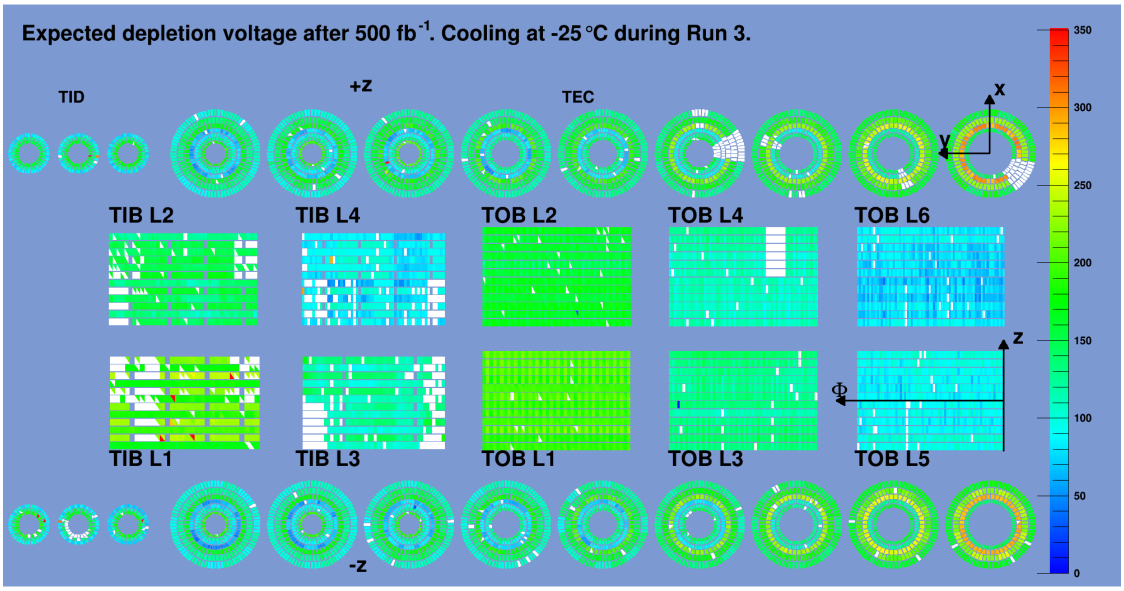


Figure 5.7.: The expected depletion voltage after 500 $fb^{-1}$ in the strip tracker. The depletion voltage is predicted to stay well below the power supply limit of 600 V during Run 3. Visible features are explained in Section 5.4.1.

A range of depletion voltages occurs and can be traced back to multiple key influences.

- The sensor thickness (see Section 4.3.5) plays an important role due to $V_{dep} \propto d^2$.
- Warmer modules are subject to faster annealing. The temperature distribution Figure 5.3 is therefore imprinted in the depletion voltage distribution. Double layers tend to be warmer, compare Section 5.2.4.
- Initial depletion voltage dictates when type-inversion will occur. Specifications allowed inital depletion voltages in a range of 100 – 300 V. After Run 3, most modules are past type-inversion.
- Radiation exposure decreases with the radial distance from the interaction point. There is increased radiation in the forward region due to neutron backscattering from the calorimeters.

A visibly higher depletion voltage occurs e.g. in TEC Disk 9 Ring 5 (the second ring of this disk, counting from inside out). This roots in a combination of several factors. R5 has stereo modules which are harder to cool; it features thick 500 µm sensors; and it is exposed to comparatively high radiation as it is positioned at intermediate radius and is subjected to neutron backscattering near the calorimeter.

Overall the depletion voltage predictions stay below 350 V in the whole strip tracker until the end of Run 3. As the power supply limit is at 600 V, the margin is ample. It had been shown in past studies that any operational temperature between −20 °C and −25 °C during Run 3 will lead to very similar depletion voltage predictions.

### 5.4.2. Strip tracker leakage current after Run 3

The leakage current prediction for after Run 3 in Figure 5.8 is again represented in a tracker map. The input parameters have been described in the previous sections.

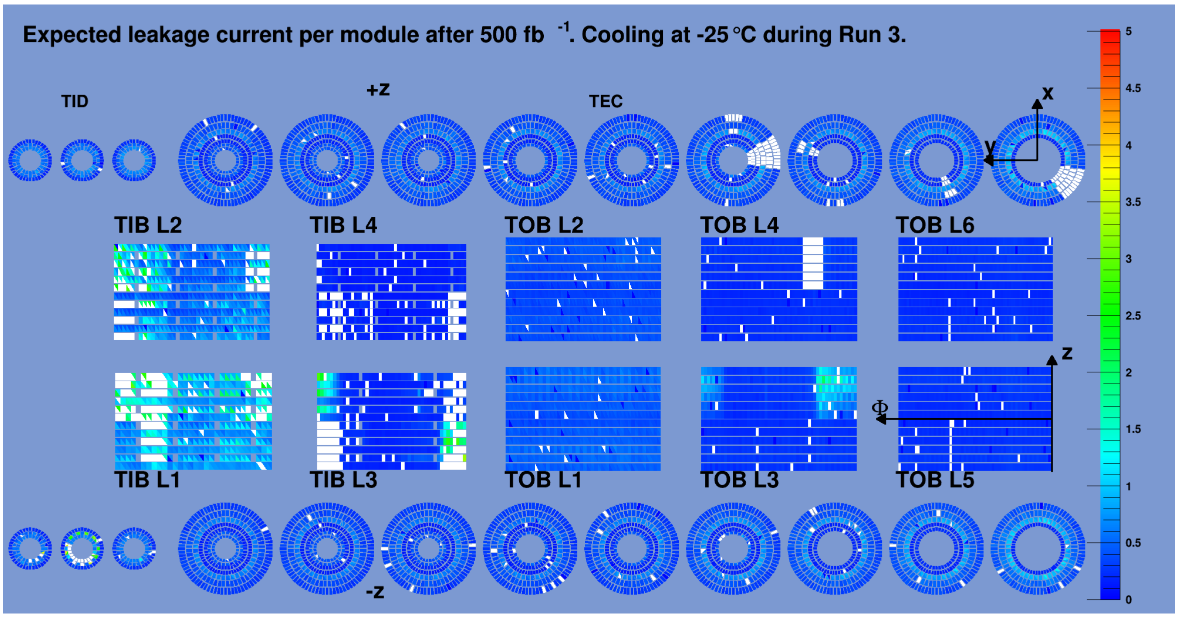


Figure 5.8.: The expected leakage current per module after 500 $fb^{-1}$ in the strip tracker. The leakage current simulation is known to underestimate the data by about 20 %. Some regions approach critically high values, where the risk of thermal runaways is imminent. Visible features are explained in Section 5.4.2.

The spread in the leakage current values has again several origins. Different sensor volumes, individual radiation exposure of the modules, but most critically temperature have an impact on the leakage current evolution.

Previous studies had shown that the leakage current simulation results underestimate the data by 20 %. The discrepancy was fairly constant over time in the past. This has to be kept in mind when interpreting the predictions. Even with the lowest possible cooling set point at −25 °C, some modules' leakage current reaches critically high values, at which a thermal runaway may evolve. Some of the white spots in the tracker map in Figure 5.8 correspond to missing input information, however some represent thermal runaways predicted by the simulation. The concerning modules are highlighted in Figure 5.9.

Most of the 307 simulated thermal runaways occur in the double layers TIB L1 and TIB L2, where suboptimal cooling (Figure 5.3) boosts the self-heating effect. In combination with high radiation exposure, the radiation-induced leakage current increase is substantial. Further clusters of thermal runaways occur in hot spots in TIB L3 and TID- D2.

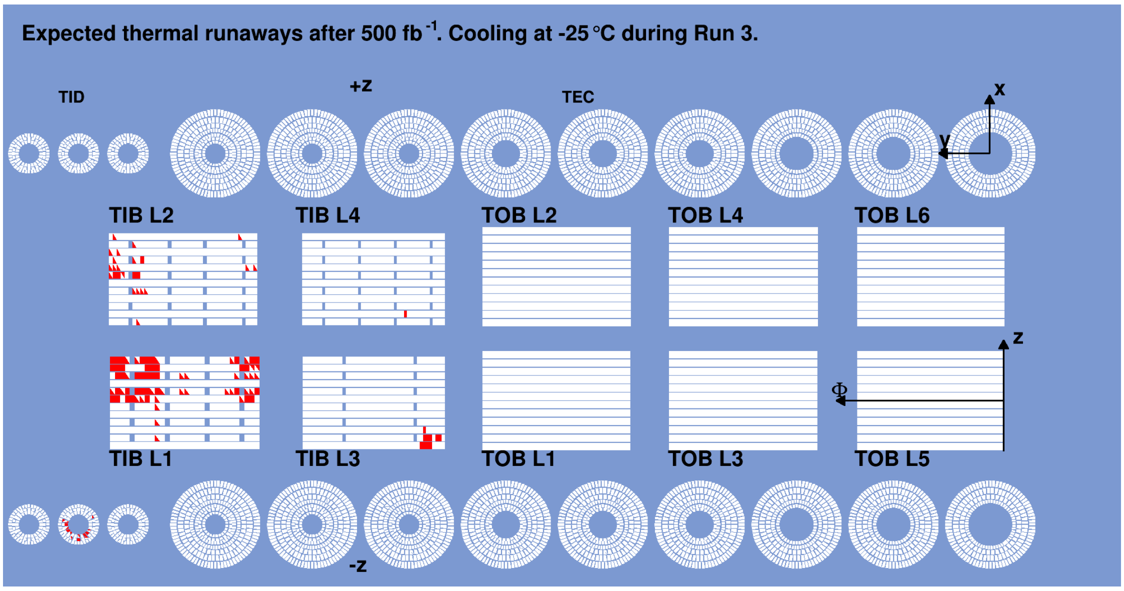


Figure 5.9.: The expected distribution of thermal runaways after 500 $fb^{-1}$ in the strip tracker. The simulation predicts a total number of 307 thermal runaways. More details are given in Section 5.4.2.

If the cooling set point during Run 3 is higher than −25 °C, or delivered integrated luminosity exceeds the 500 $fb^{-1}$ which are assumed in the applied scenario, the leakage current values will be higher and more thermal runaways will occur. Tracker maps for a 600 $fb^{-1}$ scenario with cooling at −25 °C can be found in Appendix A.3.

The occurrence of thermal runaways versus fluence is shown in Figure 5.10. To get a better understanding of the thermal runaway evolution in the strip tracker on a global scale, a hypothetical 1000 $fb^{-1}$ integrated luminosity scenario was simulated in addition.

According to Figure 5.10, the lowest risk of thermal runaways is in the TOB[2]. The radiation exposure in TOB is comparatively low and cooling is mostly satisfactory, thus barely any thermal runaways in TOB are expected before reaching 1000 $fb^{-1}$. Only few TID modules are predicted to develop thermal runaways in the 500 $fb^{-1}$ scenario, and between the 500 $fb^{-1}$ and the exaggerated 1000 $fb^{-1}$, only few additional TID modules are affected. The same statement can be made about the TIB L3 and L4. On the other hand, the double layers TIB L1 and TIB L2 show a significant increase in thermal runaway numbers from one scenario to the other. TEC modules, which are not affected at all in the realistic 500 $fb^{-1}$ scenario, make a substantial contribution to thermal runaway numbers in the 1000 $fb^{-1}$ scenario.

The overall shape of the histogram distribution shows a step up in numbers around $80 \cdot 10^{12}$ MeV $n_{eq}/cm^2$. It must be remembered that fluence in Figure 5.10 does not represent a globally valid alternative time scale; each module progresses in radiation exposure with individual speed, depending on its geometrical position in the tracker. For example a thermal runaway in TIB L1 may occur at a higher total fluence, but at an earlier point in

[2] It consists of thicker 500 µm modules, and is therefore expected to reach the limit before TIB L4 with the thin 320 µm modules.

time compared with some TIB L4 module. The latter is positioned at a higher radius and thus exposed to less fluence in the same extent of time.

It looks from the number of thermal runaways versus delivered integrated luminosity in Figure 5.11, as if the beginning of Run 3 at 300 $fb^{-1}$ marks a point beyond which the occurrence of thermal runaways may become more frequent. This coincides with notably higher integrated luminosities per day in the underlying luminosity scenario. Beyond it, the rate of occurrence increases slowly but steadily, yet without any sudden point at which a drastic increase in thermal runaway numbers must be expected, even if the strip tracker is exposed to more than the realistic 500 $fb^{-1}$ of integrated luminosity.

A critical subject related to leakage current in the strip tracker is the per-HV group leakage current. The maximum is at 12 mA per power supply. Previous studies had shown that a cooling set point of $-25\,°C$ instead of $-20°C$ ameliorates the situation. It will be crucial to monitor the leakage current per HV group during Run 3.

As the depletion voltage will stay well below any critical limit, and thus even some reverse annealing could be taken, warm-up phases during shut-downs for beneficial leakage current annealing might be a tool in the future. The regions with the highest predicted depletion voltage, especially TEC D9 R5, should in that case be carefully monitored regarding the reverse annealing of the depletion voltage.

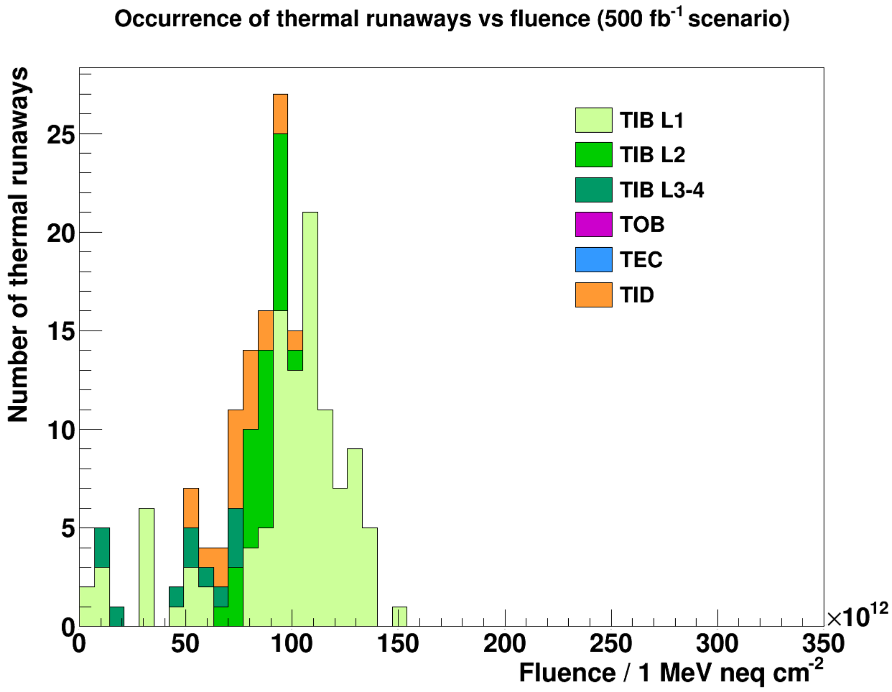


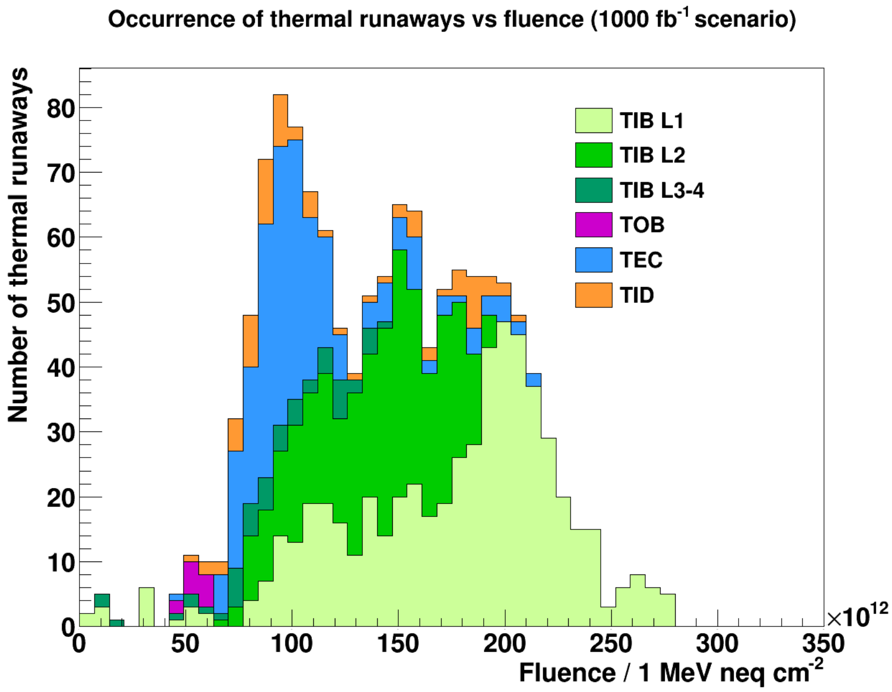


Figure 5.10.: Occurrence of thermal runaways versus fluence for both the realistic 500 fb$^{-1}$ scenario and a hypothetical 1000 fb$^{-1}$ scenario.

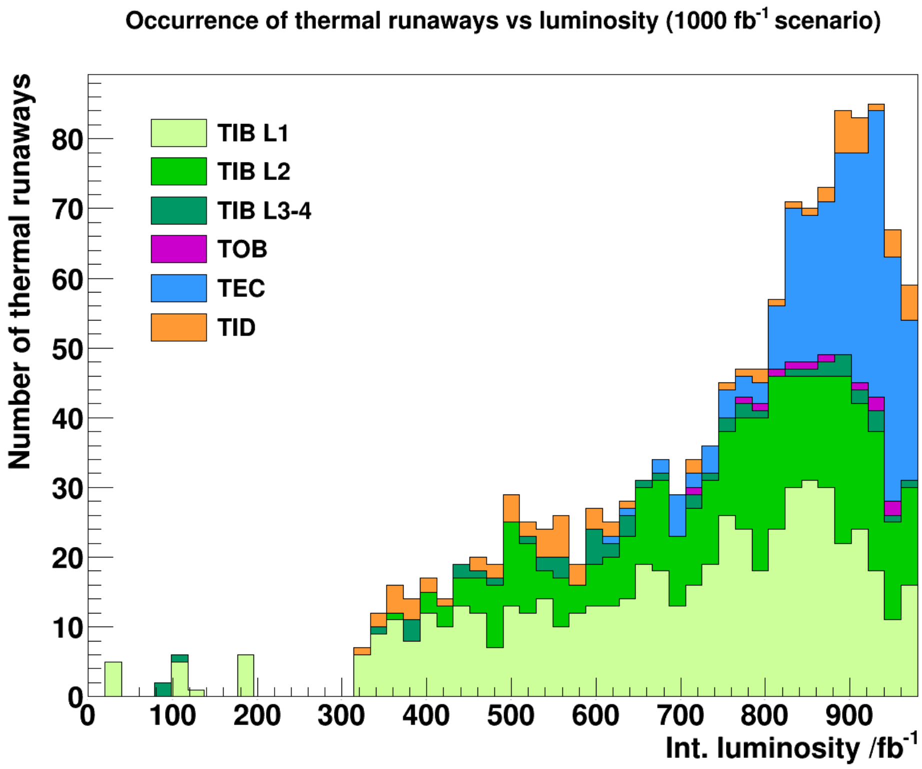


Figure 5.11.: Occurrence of thermal runaways versus luminosity for a hypothetical 1000 $fb^{-1}$ scenario. Though the occurrence rate is rising continuously, no sudden increase in thermal runaway numbers is predicted for beyond the currently prognosed 500 $fb^{-1}$.

# 6. Modelling of the CMS pixel tracker leakage current and depletion voltage

Based on the available strip tracker modelling tool, a similar tool was developed for the pixel tracker. The simulation step size of one day was chosen for the pixel tracker studies, due to the higher fluctuations in temperature compared with the strip tracker (Section 4.3.5).

The main sources of uncertainties from input parameters to the pixel tracker modelling tool were identified as

- Silicon temperatures, especially important for the leakage current
- Hamburg parameter set for the calculation of the depletion voltage
- Modules spanning a range of several mm in radius

The listed input parameters were varied separately to evaluate the sensitivity of the depletion voltage, while the rest was set to the best estimate value. This was done for both Phase-0 and Phase-1; The Phase-0 depletion voltage modelling results serve as an example in the following section.

## 6.1. Input parameters for the pixel tracker modelling tool

### 6.1.1. Fluence

The DOFZ silicon of the pixel sensors requires separate Hamburg parameter sets for neutral and charged particles (compare Section 3.2). The BRIL group provided FLUKA studies for 6.5 TeV beam energy with split neutral and charged particle contributions. Version tags are CMS FLUKA study v3.20.1.0 for the Phase-0 pixel tracker geometry and CMS FLUKA study v3.23.1.0 for the Phase-1 geometry. The FLUKA study uses track-length binning and is scored to the neutron equivalent fluence. It was normalised to an integrated fluence value per $fb^{-1}$, which was subsequently scaled with the integrated luminosity per day.

Fluence changes rapidly with radius, especially in the inner pixel layers, and so a high granularity binning of 1 mm in $r$ was paramount. 1 cm binning in $z$ is sufficient, as the simulated fluence is very homogeneous in $z$ across the tracker volume (see Section 6.4.3) and this way the barrel modules are wider than the chosen binning. Depletion voltage and leakage current are modelled for each barrel layer at $z = 0$ cm.

The modelling of leakage current and depletion voltage is only done for an average radius per layer. The average Phase-0 and Phase-1 layer radii are listed in Table 6.1, along with radii of inner and outer ladders of each layer.

| Phase-1 | L1 | L2 | L3 | L4 |
|---|---|---|---|---|
| Inner ladder radius (in mm) | 27.39 | 65.78 | 107.08 | 158.15 |
| **Average radius (in mm)** | **28.98** | **67.57** | **108.725** | **159.805** |
| Outer ladder radius (in mm) | 30.56 | 69.35 | 110.37 | 161.46 |
| Phase-0 | L1 | L2 | L3 | |
| **Average radius (in mm)** | **4.38** | **7.28** | **10.15** | |

Table 6.1.: The average radius of each pixel barrel layer was used as input for the modelling of $V_{\text{dep}}$ and $I_{\text{leak}}$. Inner and outer radii of Phase-1 are calculated from the sensors' centres of inner and outer ladders respectively [67]. For Phase-0, a generic ±0.15 mm offset was applied on the average layer radius to approximate the inner and outer radius.

The fluence exposure of a module depends strongly on its radial distance $r$ from the beam pipe. Since modules are planar and the design of a layer features alternating inner and outer ladders of modules as sketched in Figure 6.1, the modules of one layer span a range of several millimetres in $r$. Figure 6.2 gives an impression of the depletion voltage

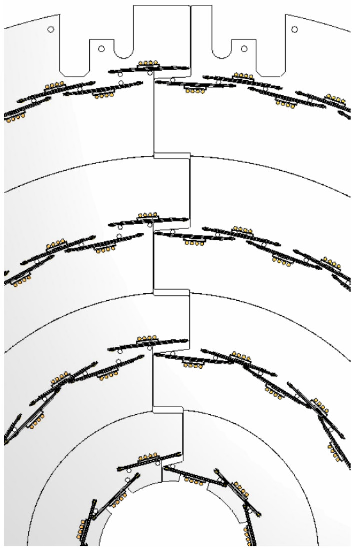

Figure 6.1.: Schematic crosssection of the Phase-1 pixel barrel showing the placement of ladders with modules attached, as well as the position of the cooling loop pipes. Taken from [59].

spread expected within one pixel barrel layer solely attributed to different radial positions of modules.

A rough expectation for the fluence in the detector would be a $\propto r^{-2}$ dependence. Consequently the impact of the radius variations in Figure 6.2 is greatest for L1, with depletion voltage differences of about 50 V between inner and outer radius. However, as the difference between the inner and outer layer radii in Figure 6.2 is only 3 mm, the FLUKA granularity of 1 mm in $r$ already plays a role and results are not expected to be

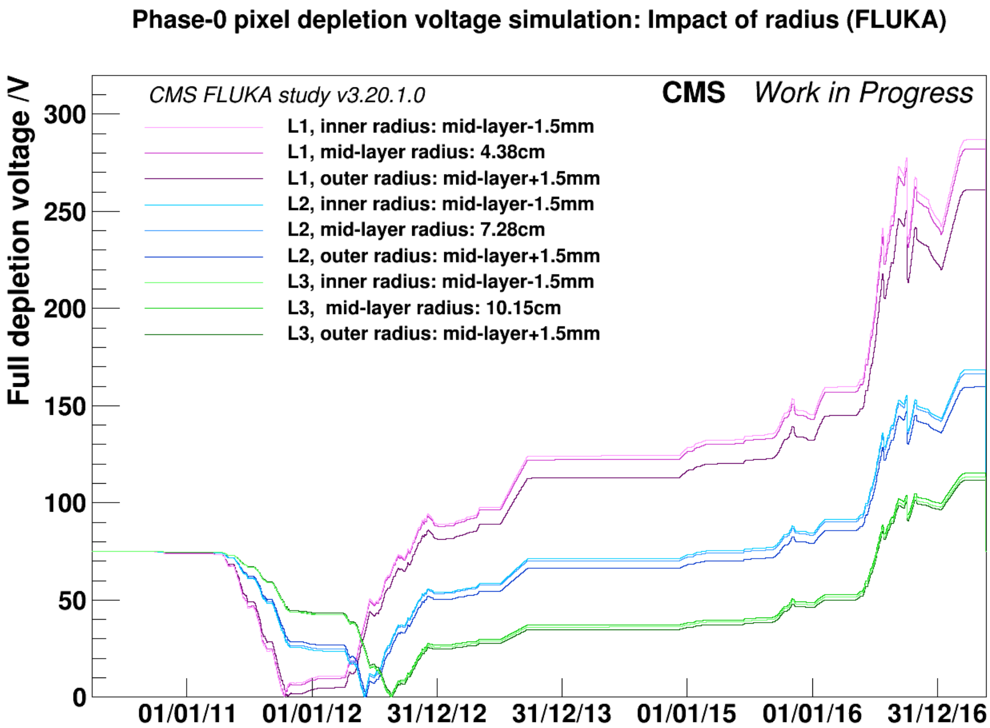


Figure 6.2.: Impact of radius on the depletion voltage results. Since each of the three Phase-0 pixel barrel layers consists of inner and outer ladders, which are placed at different radii, inner ladders are expected to see correspondingly higher fluences. For all following studies the mean value of inner and outer radius is taken.

overly precise. In conclusion, the average radius of a layer is a reasonable choice for the modelling tool, even though a small difference in depletion voltage is expected for the L1 inner and outer ladders.

### 6.1.2. Delivered integrated luminosity

The official recorded integrated luminosity was obtained using the *brilcalc* tool [68]. It extracts the luminosity measured by BRIL. A script from the strip tracker community was then used to obtain the delivered integrated luminosity per day [69]. As luminosity production was not yet finished at the time of writing, a scenario for a total integrated luminosity of ~70 fb$^{-1}$ in 2018 in CMS was used; it has been progressively replaced by newly available luminosity data. For Run 3, a 400 fb$^{-1}$ scenario was applied. The resulting total integrated luminosity input scenario is shown in Figure 6.3.

### 6.1.3. Hamburg model and leakage current parameter set

The depletion voltage of the pixel barrel is modelled with two separate parameter sets for neutral and charged irradiation contributions. This is necessary due to the NIEL violation

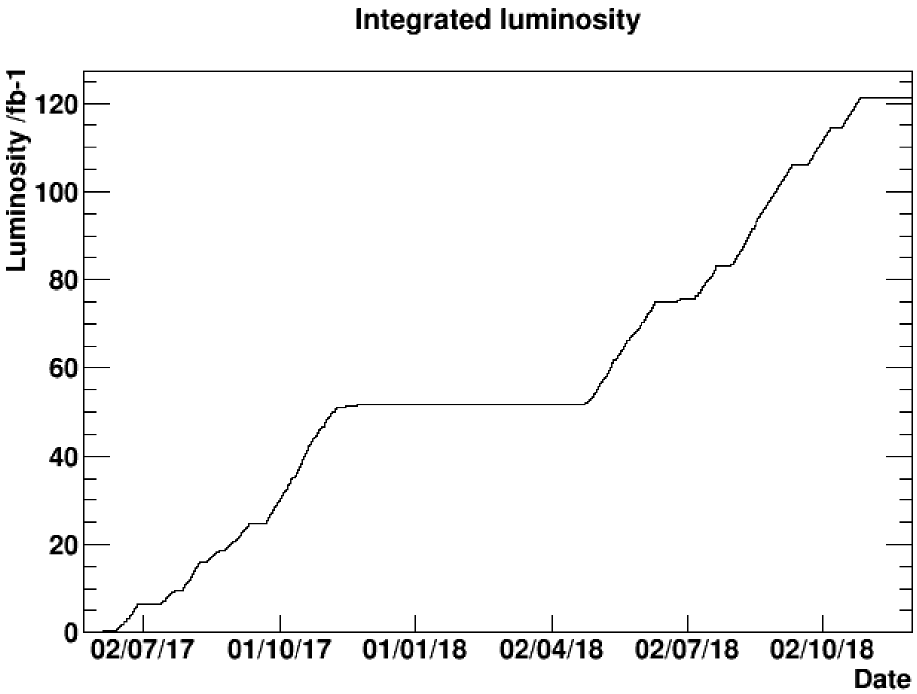


Figure 6.3.: The delivered integrated luminosity per day was used as input to the modelling script for Phase-1. Measured data were regularly updated, progressively overwriting the realistic scenario which has been assumed for the future. The resulting total integrated luminosity scenario is shown here.

of charged particles in DOFZ material described in 3.2. Two parameter sets for oxygenated silicon were available: *RD48* and *CBoxy* [29, 70], both of which assume a saturation of the Hamburg model's reverse annealing term, as it was found in laboratory studies [71]. While the RD48 set is only implemented with saturation for charged particles, the CBoxy set has been extracted in conjunction with a parametrisation which assumes saturation for both the neutral and charged particles' reverse annealing terms. A comparison is shown in Figure 6.4.

Differences of up to 40 V between the two parameter sets occur in the outer L3, where the discrepancy is largest. In case of the pixel Phase-0 scenario, the difference seems to become smaller after a higher total fluence. The parameter set RD48 was found to describe the Phase-0 depletion voltage data best. Contrarily, the second parameter set CBoxy yielded a better description of the depletion voltage of the Phase-1 pixel, and was used there instead of the RD48 set.

It was assumed that the leakage current parameter set given in Section 3.6 is valid, even though it was extracted from measurements of different time and temperature ranges. The temperature validity range of the parameter set in [2] lies between 21 °C and 106 °C, and therefore above the application case of the pixel detector. Specifically for effective $\alpha$ parameters above $6 \cdot 10^{-17}$ A/cm additional short-term annealing components are expected to enter the leakage current behaviour. Typical values for the pixel tracker during operation lie between $6 \cdot 10^{-17}$ A/cm and $7 \cdot 10^{-17}$ A/cm.

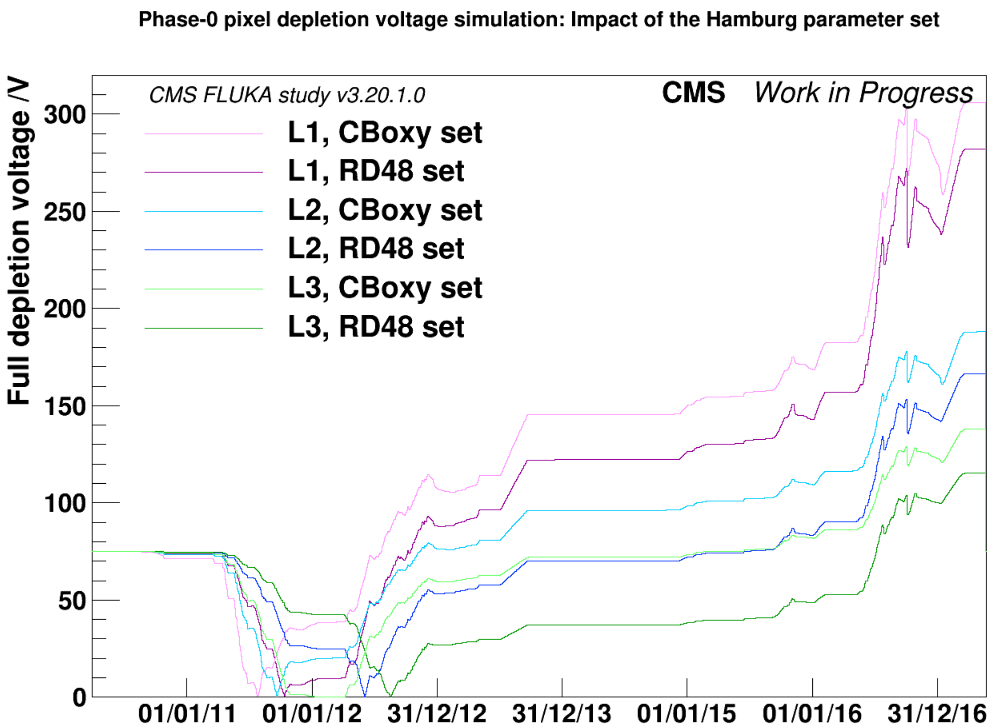


Figure 6.4.: Two different parameter sets for oxygenated silicon were available, called RD48 and CBoxy. Differences between these two give an impression of the model's uncertainty.

### 6.1.4. Temperature

The pixel barrel has no direct silicon temperature measurements. The spatially closest information available are measurements on the carbon fibre support structure near the cooling loop just outside the barrel, whose average value will be denoted $T_{cf}$ in the following. Precise estimations for the silicon temperature $T_{sil}$ of the pixel sensors are an important input to the modelling tool. $T_{sil}$ is expected to increase with module power, compare Section 3.6.1. The offsets $\Delta T = T_{sil} - T_{cf}$ for each of the layers in the pixel tracker were the missing information.

The module power is approximately[1] composed of the high voltage (HV) sensor power $P_{HV} = V_{bias} I_{leak}$ and the low voltage (LV) ROC power that consists of a digital and an analogue contribution, $P_{LV} = P_{ana} + P_{dig}$:

$$P_{module} = P_{HV} + P_{LV} \tag{6.1}$$

In order to understand the impact of temperature uncertainty on the depletion voltage modelling, the temperature offset $\Delta T$ was varied, while all other input parameters were kept fixed. The result in Figure 6.5 is again an example of the Phase-0 scenario.

Temperature offsets in Figure 6.5 were varied for a range of $\binom{+10K}{-1K}$ around the Phase-0 best guess temperatures described in the following section. Although the impact on the

[1] Neglecting the power contribution of the *Token Bit Manager* (TBM) shown in Figure 4.6, compare [60].

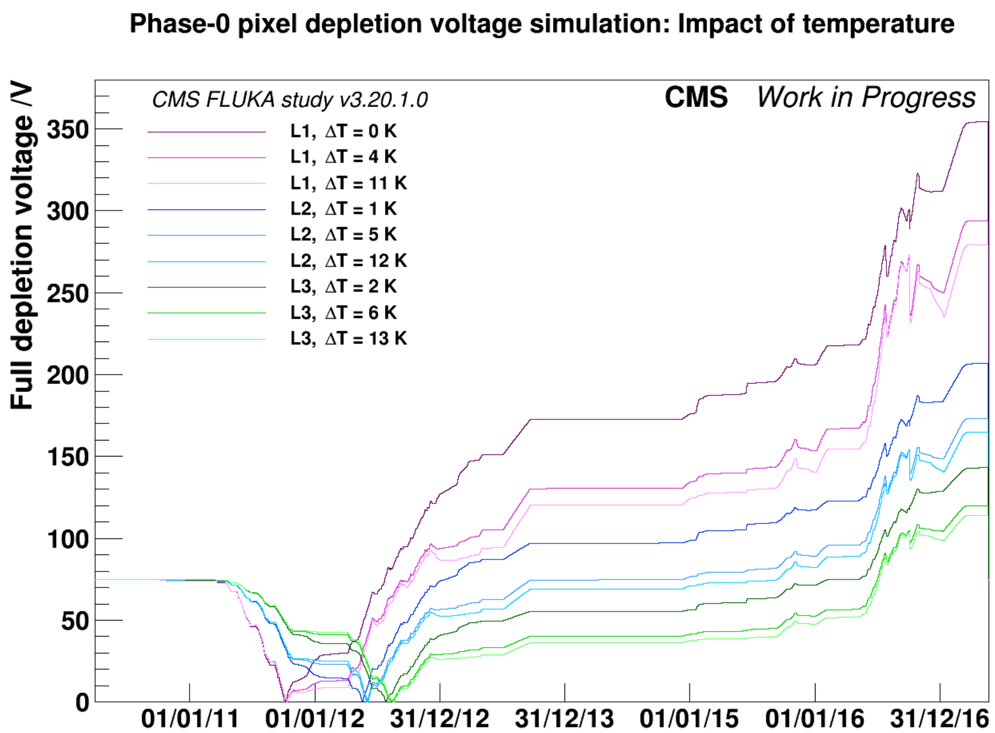


Figure 6.5.: Depletion voltage results depend on the estimated temperature offset $\Delta T$ added to the cooling loop temperature $T_{cf}$ in order to estimate $T_{sil}$. Assumptions of higher operational temperatures lead to lower depletion voltage predictions in Phase-0: At high temperatures, annealing is accelerated and beneficial short-term annealing decreases the depletion voltage. Detrimental reverse annealing does not play a role for the considered operational temperatures mostly around or below 0 °C.

depletion voltage in Figure 6.5 seems large, this range was intentionally exaggerated and almost certainly contains the true silicon temperature.

In the following sections, the estimation of $\Delta T$ for Phase-0 and Phase-1 is described as well as the underlying input temperature scenarios.

#### 6.1.4.1. Silicon temperatures in the Phase-0 pixel detector

From 2010 until YETS 2011/12, the $C_6F_{14}$ cooling set point was at +7 °C; It was then changed to 0 °C until LS1, after which it was lowered to −10 °C. During LS1 the barrel had been extracted. A temperature scenario with 80 days at room temperature of 20 °C was assumed to account for the time during which work in the cleanroom has been performed.

The available Phase-0 temperatures were averaged for each day over all temperature probes associated to cooling loops, to obtain the mean carbon fibre temperature $T_{cf}$. The result is shown in Figure 6.6.

The Phase-0 mechanical design of the barrel layers resembles the design of the Phase-1 layers 2, 3, and 4. Even though the cooling mechanism and precise layout of the barrel

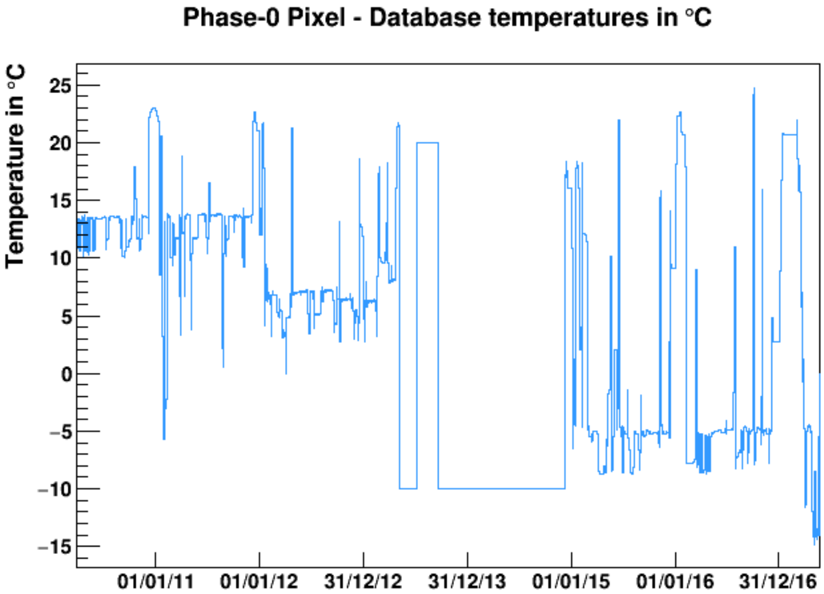


Figure 6.6.: Averaged carbon fibre temperature $T_{cf}$ for Phase-0. It serves as a basis for the estimation of $T_{sil}$, for which an offset is added whenever the LV is on. The resulting temperature scenario is used as an input to the depletion voltage modelling in Figure 6.11.

is different in Phase-0, $\Delta T$ is assumed to be comparable. This allows to estimate the temperature offset $\Delta T$ for each of the barrel layers L1-3 between $T_{cf}$ and $T_{sil}$. They loosely follow the insights recently won from the laboratory studies described in the following section. The final temperature offsets, which were added to $T_{cf}$ in order to compute the model curves in Figure 6.11, are $\Delta T_{L1} = +3$ K, $\Delta T_{L2} = +2$ K, and $\Delta T_{L3} = +3$ K.

#### 6.1.4.2. Silicon temperatures in the Phase-1 pixel detector and thermal mock-up studies

Three temperature sensors are placed on each cooling loop: Below the first, middle, and last module of the cooling loop (*In*, *Middle*, *Return*). All three positions are on the edge of the barrel, as indicated in Figure 6.7.

The unprocessed Phase-1 carbon fibre temperature data from the pixel barrel is shown in Figure 6.8. $T_{cf}$ was obtained by averaging these measurements irrespective of the layer association of the temperature probes, since no clear layer dependence was observed in the temperature data.

The offset $\Delta T$ between $T_{cf}$ and $T_{sil}$ was derived from dedicated laboratory studies of the pixel community. A mock-up layer 2 half-shell, largely identical to the real Phase-1 barrel layer 2, had been presciently constructed for precise temperature modelling [72]. Parameter settings like module power and cooling flow were chosen according to the real detector environment. The module power was set to 2.9 W (for L2), split between 0.1 W HV power and 2.8 W from LV, compare Equation (6.1). The $CO_2$ cooling flow for the mock-up was set to 2.5 g/s, which had been the setting in BPIX until TS2. The cooling

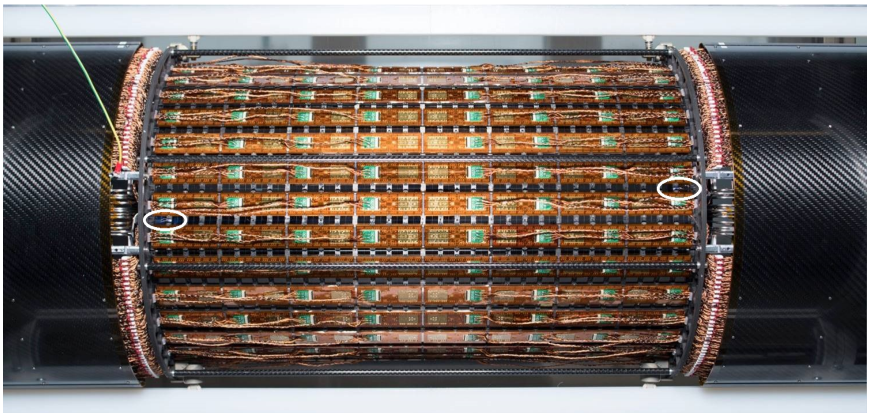

Figure 6.7.: The pixel barrel in the laboratory. Cooling loop pipes are installed in a zigzag fashion. The position of two example cooling loop sensors is marked by white circles.

liquid in the mock-up was brought to the working point two-phase state by pre-heating to achieve the same conditions as in the real detector.

After the $CO_2$ enters the pixel barrel, the cooling temperature is dropping as the $CO_2$ pressure decreases. As a result, the temperature spread observed in the thermal mock-up is approximately ±2 K around the average silicon temperature.

An anchor point was necessary to compare the mock-up with the real detector. When both are in a cooled-down state and module power is off, temperatures should equalise in the tracker volume. The $T_{cf}$ measurement is then expected to be identical to $T_{sil}$ in the real detector. Cooling set points were comparable at −22 °C in the detector and −22.5 °C in the mock-up. The carbon fibre temperatures in the detector were found to be around an average of −17.5 °C, while the average mock-up temperature was at −19.5 °C. A possible explanation for this difference could be the surrounding strip tracker heating the ambient, which is not present in the laboratory. Correcting for this offset, the mock-up studies predict silicon temperatures in the detector L2 between −12 °C and −8 °C with module power on.

These predictions tally with the experiential expectations for $T_{sil}$. An offset of $\Delta T$ = 2 K between $T_{cf}$ and $T_{sil}$ is estimated to be realistic in a setup without base strips (see Section 4.3.6). Starting from the approximate average $T_{cf}$ = −11.5 °C found in the real detector when the detector is on, this leads to $T_{sil}$ = −9.5 °C, assuming no base strips. With base strips, slightly higher temperatures are expected, in full accordance with the thermal mock-up predictions for L2.

Further support for these values comes from a thermal simulation which was developed in the scope of [60]. For the settings in the real detector L2 it predicts $T_{sil}$ = −9.4°C and $T_{cf}$ = −11.0°C without base strips. According to the simulation, the base strips used in layer 2-4 could further account for an additional +1 K due to the higher thermal resistance between base strips and carbon fibre. Layer 1 in the Phase-1 pixel barrel does not have base strips, however the power consumption is higher closer to the IP due to higher hit rates and corresponding digital activity. These two effects are estimated to cancel each

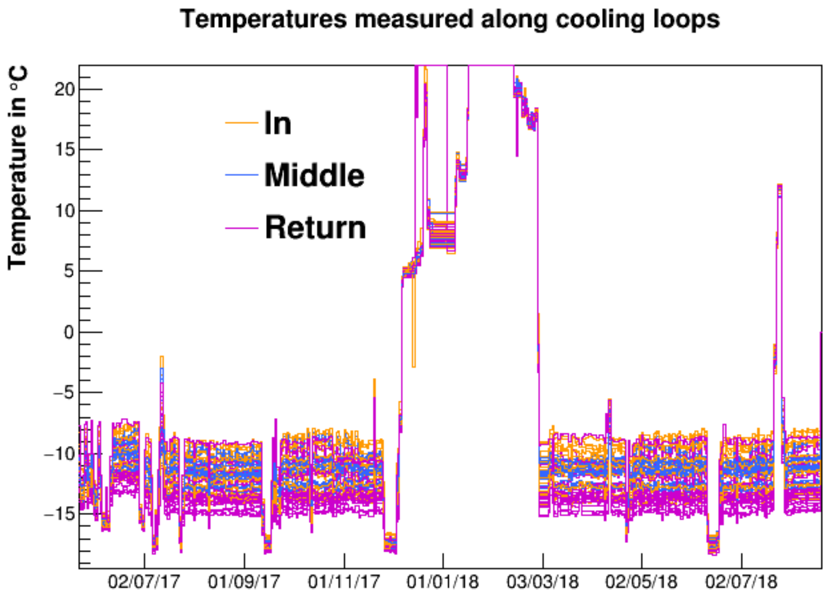


Figure 6.8.: Pixel Phase-1 temperature measurements. The temperature probes are placed along the carbon fibre near the cooling loop (In, Middle, Return: compare Figure 6.7). Values are averaged and the average, $T_{cf}$, is used as a basis for estimation of the silicon temperature $T_{sil}$. In periods when the detector is on, $T_{cf}$ lies around −11.5 °C.

other out. Layer 4 is adjacent to the strip tracker inner barrel layer, which is on average warmer than −8.5 °C. Therefore layer 4 was attributed a slightly higher temperature offset of $\Delta T_{L4} = 4$ K. Table 6.2 summarises these steps.

The temperature offsets $\Delta T$ listed in Table 6.2 were added to the cooling loop mean value of each day whenever the detector LV was on. The example in Figure 6.9 shows the final resulting average silicon temperature scenario for L1.

The mock-up studies yielded an absolute estimate for $T_{sil}$ with the assumed module power close to the situation in the real detector at present if the LV is on. Recent mock-up results estimate the thermal contact to be around 2.6 K/W for L2. However an implementation of the thermal contact like in the case of the strip tracker was not applied in the following studies.

### 6.1.5. Geometry

The sensor volume comes into play when calculating the leakage current. Without the guard rings, the active volume amounts to $(6.48 \times 1.62 \times 0.0285)\ \text{cm}^3 = 0.299\ \text{cm}^3$ per sensor. The sensor volume is the same for Phase-0 and Phase-1.

The necessity of a geometry correction to the diode's solution for the depletion voltage in the pixel modelling tool (compare Section 2.7.1 and Section 5.2.3) is discussed in the following. A single pixel has a pitch area of $(100 \times 150)\ \mu\text{m}^2$, and the pixel implant area is about $(80 \times 130)\ \mu\text{m}^2$, compare Figure 4.5.

| | L1 | L2 | L3 | L4 | |
|---|---|---|---|---|---|
| Cooling set point | -22 | -22 | -22 | -22 | °C |
| Mean $T_{\mathrm{cf}}$ (Figure 6.8) | -11.5 | -11.5 | -11.5 | -11.5 | K |
| + Offset $\Delta T$ | +3 | +3 | +3 | +4 | °C |
| Resulting $T_{\mathrm{sil}}$ (Figure 6.9) | -8.5 | -8.5 | -8.5 | -7.5 | °C |

Table 6.2.: Summary of the input temperatures. Depending on the layer, an offset of $\Delta T_{\mathrm{sil}} = 3$ K or 4 K is added to the average carbon fibre temperature. The latter is permanently changing during detector operations due to the dependence of digital activity on detector hits in the pixel tracker. An average value per day is considered, whose value lies around $-11.5\,°\mathrm{C}$ when the detector is on (compare Figure 6.8).

The width-to-pitch ratio is sufficiently close to 1 in both spatial directions $\frac{w}{p} \to 1$ to assume $A_0\left(\frac{w}{p}\right) \to 0$, and the depletion voltage formula for a pixel sensor approaches the original solution for a diode

$$V_{\mathrm{dep,pix}} \approx V_{\mathrm{dep,diode}}. \tag{6.2}$$

The correction would be of the order of $O\left(10^{-2}\right)$. Since the correction is expected to be negligible, no geometry factor is applied in case of the pixel depletion voltage modelling.

### 6.1.6. Depletion voltage data from cluster size and cluster charge

Similar to the strip tracker, full bias scans are performed about every half-year. They involve all sectors of the pixel barrel and endcap. Several hours of collision time are needed for these scans during which data is not usable for physics analyses.

The HV scans before 2018 had been too scarce to reliably test the modelling results against. Mini HV bias scans have since been adopted as an approximately bi-weekly practice. They include one representative power group in each barrel layer and endcap ring and yield comparable results as the full scans. A comprehensive list of the HV scans can be found in Appendix A.2.

For each voltage step of the bias scan, a convoluted Landau-Gauss distribution was fitted to the raw data to extract the most probable value (MPV) of the cluster charge distribution. An exemplary curve of MPVs was already given in Figure 5.5.

Subsequently the kink position associated with the full depletion of the sensor volume can be extracted by either of the following methods

- Two linear fits whose intersection point marks $V_{\mathrm{dep}}$
- Fitting the curvature with a parabola, where the minimum marks $V_{\mathrm{dep}}$
- By visual judgement

For Phase-0 the linear fitting algorithm described in Section 5.3 was used on cluster charge measurements to obtain data for comparison.

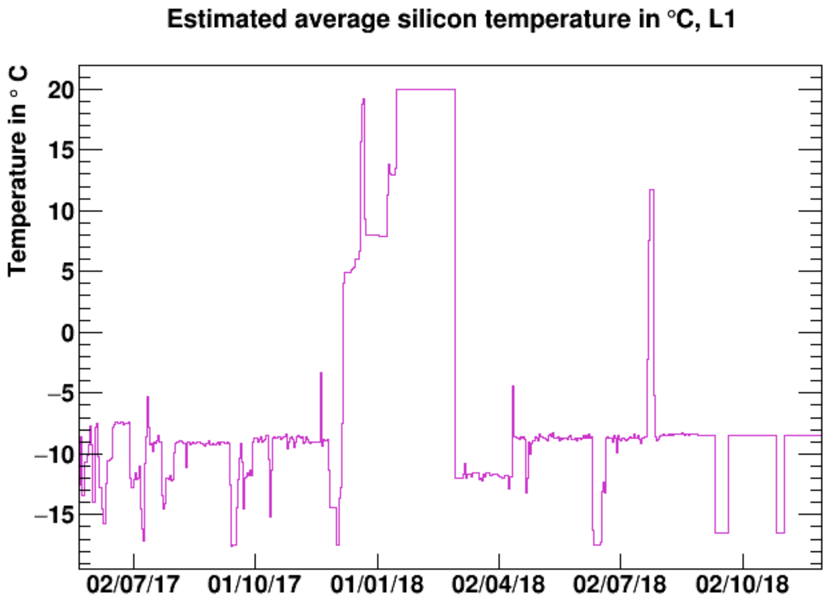


Figure 6.9.: The resulting Phase-1 pixel layer 1 silicon temperature scenario used as input for the leakage current and depletion voltage models.

In pixel Phase-1 the usage of the linear fitting algorithm is unsuitable due to the no longer textbook shapes of the CC and CS distributions with the onset of trapping. This also increases the uncertainty of the method for obtaining data significantly.

The curvature method is a promising tool for distributions which do no longer saturate in a plateau. While a curvature algorithm is available from the strip tracker community, the fit needs further adaptation and is not yet applicable to the pixel tracker bias scan results. The $V_{dep}$ data points for Phase-1 were therefore extracted by eye for both CS and CC. Future plans beyond the scope of this thesis include the tuning of the curvature fitting algorithm for a more reproducible data point extraction.

A source of uncertainty is the definition of the kink position; this may vary in a range of $\sim$ 50 V between extraction methods. Additionally CC and CS results sometimes show a large discrepancy, which can be up to 100 V in L1 in extreme cases.

A cross-check with some successful curvature fit results showed that the visual extraction approach is justified; Differences between extraction methods lie within the discrepancy seen between CS and CC.

### 6.1.7. Leakage current data

A tool for the extraction of the leakage current data from the database was already available [73]. It creates a list of successful LHC fills with stable beams. Based on this list, the first leakage current database entry is taken after more than 10 minutes have passed since the declaration of stable beams. By this time, the detector environment should be in a reasonably stable temperature state.

The readout and storage of leakage current data is per HV group; no information about the $z$ distribution of the leakage current is available in the real detector. Leakage current is expected to be comparable for all modules in a HV group. A more detailled discussion can be found in Section 6.4.3.

## 6.2. Estimation of the combined input parameter uncertainties

In an attempt to understand the total uncertainty, the radius, temperature offset and parameter set were varied simultaneously in Figure 6.10. While inner radius, RD48 parameter

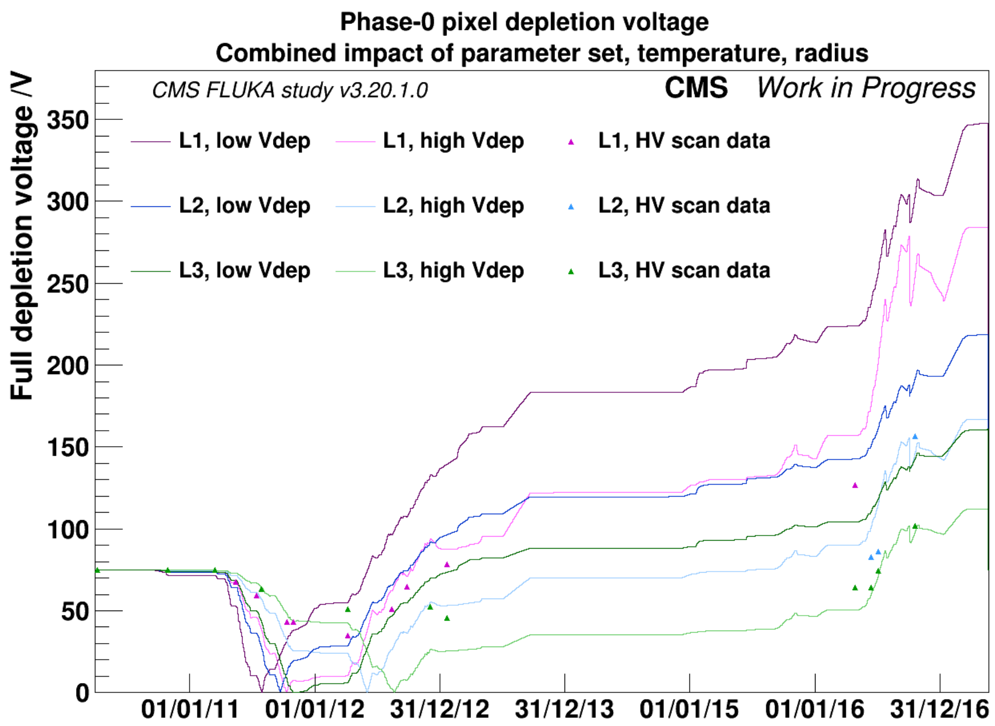


Figure 6.10.: Simultaneous variation of the modelling input parameters radius, parameter set and temperatures show a large impact on the depletion voltage. A more detailed description is given in Section 6.2.

set and low temperatures individually lead to low depletion voltage values in the Phase-0 example, the interplay between the parameters is intricate, but overall leads to expectedly low values. On the other hand outer radius, RD48 parameter set and high temperatures lead to high depletion voltage results in the Phase-0 example. The combined variation of the parameters in Figure 6.10 gives an estimation for the minimum ("best case") and maximum ("worst case") depletion voltage values that would be covered by the model.

In conclusion, the explanation for discrepancies between data and model cannot be attributed to a single aspect, but is due to a combination of several factors. The complexity of the underlying model and limited possibilities of investigation on the past beyond the recorded database values did not allow to further resolve the influences.

## 6.3. Phase-0

### 6.3.1. Phase-0 depletion voltage

The pixel modelling tool was first compared to available Phase-0 data in order to assert its general reliability. In Figure 6.11, the depletion voltage is modelled for each of the three Phase-0 pixel barrel layers. Cluster charge data points were extracted with the linear fit algorithm described in Section 6.1.6. Clearly visible are the periods without

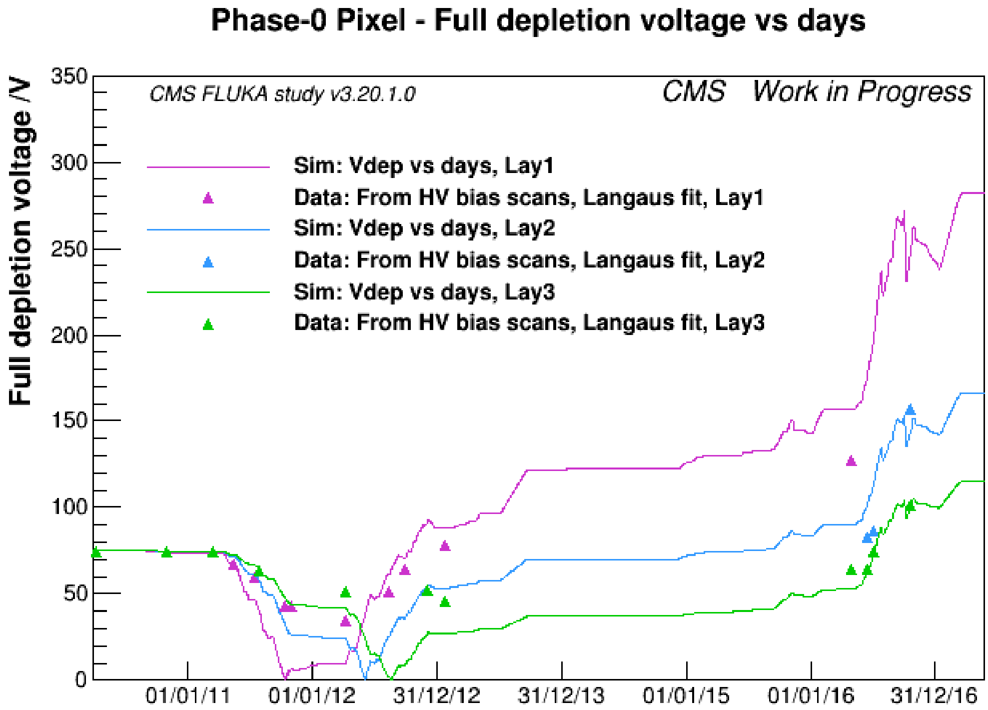


Figure 6.11.: Modelling of the pixel Phase-0 depletion voltage for each of the three barrel layers. Cluster charge data was obtained from HV bias scans using the linear fit algorithm.

luminosity production, technical stops and the LS1 in 2013-2014, where the depletion voltage shows a plateau. Warm-up periods lead to annealing behaviour in the depletion voltage. Luminosity production ended in November 2016, after which the Phase-0 detector was extracted.

L1 receives higher fluences and undergoes type-inversion first. The data points do not follow the model all the way to zero around the period of type-inversion. This behaviour is inherent to the data point extraction method shown in Figure 5.5. The simulated depletion voltage evolution in L1 is always ahead of the data. This results in an underestimation of the data before type-inversion, and an overestimation after type-inversion. Only two data points are available for L2 due to the lack of bias scan data. The data points in 2016 however represent a useful anchoring point and are described well by the modelled depletion voltage within the uncertainties. In case of L3, the simulation again seems to be slightly ahead of the data in 2012 during type-inversion. However in 2016 the data points are well described by the model curve.

The seeming discrepancy between data and simulation is covered by the combined uncertainties of the data points, see Section 6.1.6, and the input data, discussed in Section 6.2. Differences between simulation and data are most pronounced for L1, where the uncertainties are also largest. The Phase-0 data allowed a successful validation of the pixel modelling tool.

## 6.4. Phase-1

### 6.4.1. Phase-1 depletion voltage

In the following, the depletion voltage of the present Phase-1 pixel tracker is studied. The input parameters for the depletion voltage model as well as estimated uncertainties were covered in the previous sections. In Figure 6.12, the depletion voltage for the four Phase-1 pixel barrel layers L1-4 is shown together with the CS and CC data. For the ratio plot, the mean value of both CS and CC data points of a given HV scan was divided by the model prediction of that day.

While the model describes the data within the estimated uncertainties, there are some discernible tendencies. Except for recent scan points in L1, the simulation tends to underestimate the depletion voltage data. Yet after warm periods[2] (scan points 19/04/2018 and 31/07/2018), the data and model are almost perfectly in agreement. The only exception are again the more recent L1 data points.

Figure 6.13 shows the underlying evolution of $N_{\text{eff}}$ in L1, described by the Hamburg model (see Section 3.3). $N_{\text{eff}}$ is further broken down into the contributions from each of the Hamburg model terms $N_{\text{C}}$, $N_{\text{A}}$, and $N_{\text{Y}}$ for both neutral and charged particles. After the annealing periods the contribution from $N_{\text{A}}$ has worn off. This is the case the full scan performed on 19/04/2018 after the YETS, and to a lesser extent the 31/07/2018 scan directly after the *machine development* MD2 (Section 6.4.1.1). It could be an indication that while the Hamburg model CBoxy parameters for stable damage $N_{\text{c}}$ and reverse annealing $N_{\text{Y}}$ are well suited for the application case pixel Phase-1, the short-term parameters or the $N_{\text{A}}$ implementation may have to be revised.

As $N_{\text{C}}$ and $N_{\text{Y}}$ seem to be well modelled, this suggests that the FLUKA fluence simulation for $z = 0$ cm in the pixel tracker is accurate. This statement must be put into perspective by the comparatively large uncertainties of the modelling tool.

After July 2018, the L1 data points lie below the depletion voltage model curve in Figure 6.12. This coincides with a change of the modules participating in the HV miniscans for L1 after July 2018. The previous set had developed an unexplained dip in the rising

[2]See Appendix A.2 for the 2018 schedule including TS, *machine development* (MD) and HV scan dates.

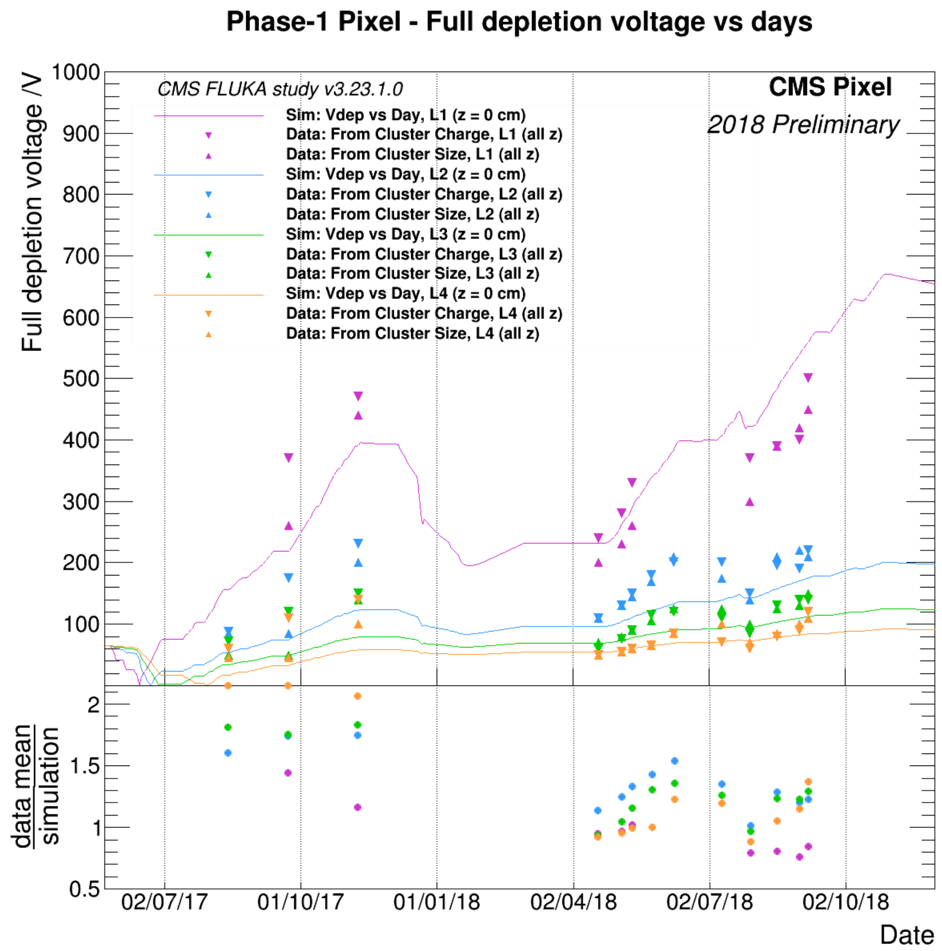


Figure 6.12.: Modelling of the pixel Phase-1 depletion voltage for each of the four barrel layers. Data points correspond to the saturation point of cluster charge and cluster size data from HV bias scans.

flank of the CS and CC measurements. A direct comparison of these modules can only be done as a subset of the two available full scans. The present L1 module selection shows indeed lower values in the same scan, though $r$ or $z$ position cannot explain the difference. It is estimated to be 25 V. Trapping or other radiation effects influencing the shape of the CC and CS distribution could also have an impact, possibly explaining the tendency to show the kink position at lower bias voltages in the more recent L1 data. Also the validity of the Hamburg model is no longer obvious in case of L1, since it has been exposed to a total fluence of $\sim 7 \cdot 10^{14}$ MeV $n_{eq}/cm^2$ as of October 2018.

Overall, the simulation describes the data well enough to allow future projections of the depletion voltage. The modelling tool for the pixel depletion voltage therefore provides a comparatively easy and fast way to estimate the detector conditions with respect to optimal bias settings. Application cases of the modelling tool results are described in the following Section 6.4.1.1 and Section 6.5.

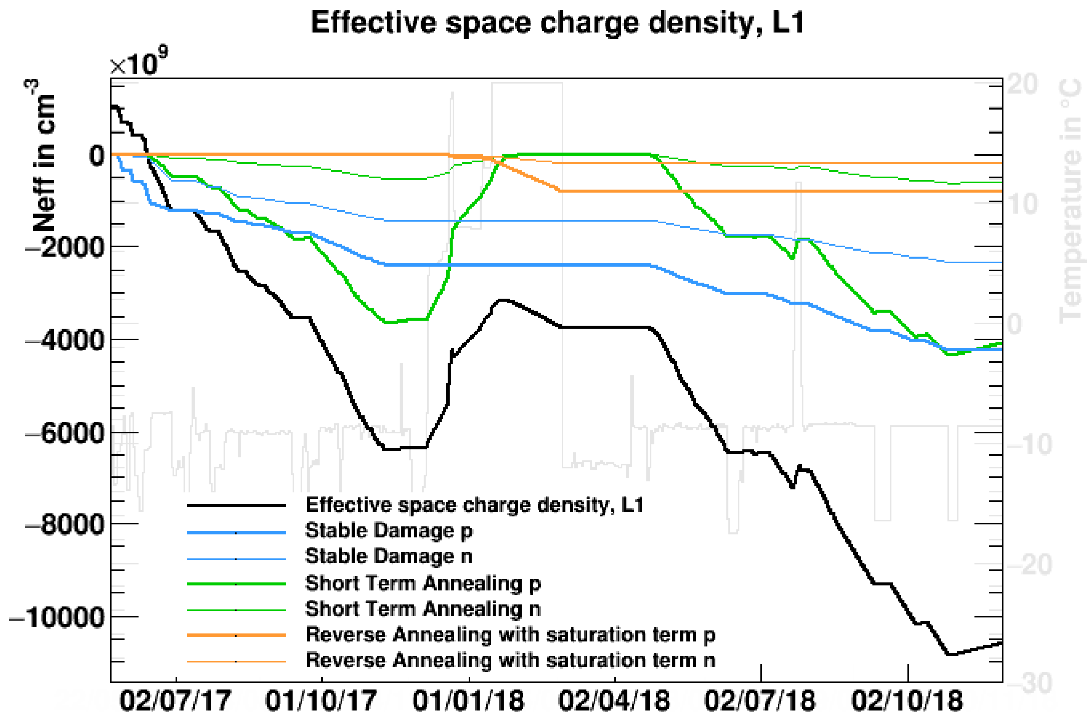


Figure 6.13.: Effective space charge evolution in L1 as predicted by the Hamburg model. The total $N_{\mathrm{eff}}$ is the result of three terms - stable damage $N_{\mathrm{C}}$, short-term annealing $N_{\mathrm{A}}$, and reverse annealing $N_{\mathrm{Y}}$. Contributions from neutral (n) and charged (p) particles are split as they show different behaviour in oxygenated silicon. The silicon temperature is given as an overlay. Its impact on the annealing terms is evident.

#### 6.4.1.1. Annealing studies for the Phase-1 pixel depletion voltage

The bias setting of L1 had been at 400 V since the beginning of 2018 and during operations in 2018, the L1 depletion voltage approached this value. Some action was required in order to continue with optimal settings for the innermost layer. Two main options were considered; raising the bias voltage, or warming up the detector to make use of beneficial annealing of the depletion voltage (compare section 3.3). Pixel sensor specifications theoretically allow bias voltages well beyond what is currently possible in the detector. The limiting factor are the *power supply units* (PSU) with a maximum output of 600 V.

Changes of the bias voltage entail the need for new calibrations. Pixel cluster shapes depend on incident angle, Lorentz angle (due to the Lorentz force), and field configuration, which changes under $V_{\mathrm{bias}}$ and with irradiation; templates of these cluster shapes are used in the offline data reconstruction. The production of new calibration templates requires some leadtime. If the depletion voltage can be predicted reliably, the templates can be prepared in advance; Bias settings can be applied right when needed without compromising on quality in the first iteration of data reconstruction[3].

The second option, warming up the detector, meant no less effort as this entailed the need for new calibration templates as well as possible impacts on other parts of the experiment. Possible days for a warm-up procedure were the upcoming TS and MD periods.

Multiple times, projections of the depletion voltage for different warm-up annealing scenarios were provided as a basis for decisions.

During preparation of TS1, the L1 depletion voltage was predicted to increase beyond the bias voltage setting at the time soon after TS1, if no action was to be taken. It was decided to raise the bias voltage of L1 to 600 V after TS1. However the attempt had to be abandoned for technical reasons.

The annealing study in Figure 6.14 was requested by the Pixel Monitoring Group to answer the question which impact warm days in MD2, MD3, and optionally MD4, have on the depletion voltage evolution in L1. The highest achievable warm-up temperature was assumed to be 17 °C. Based on these results, the annealing of the detector at 17 °C

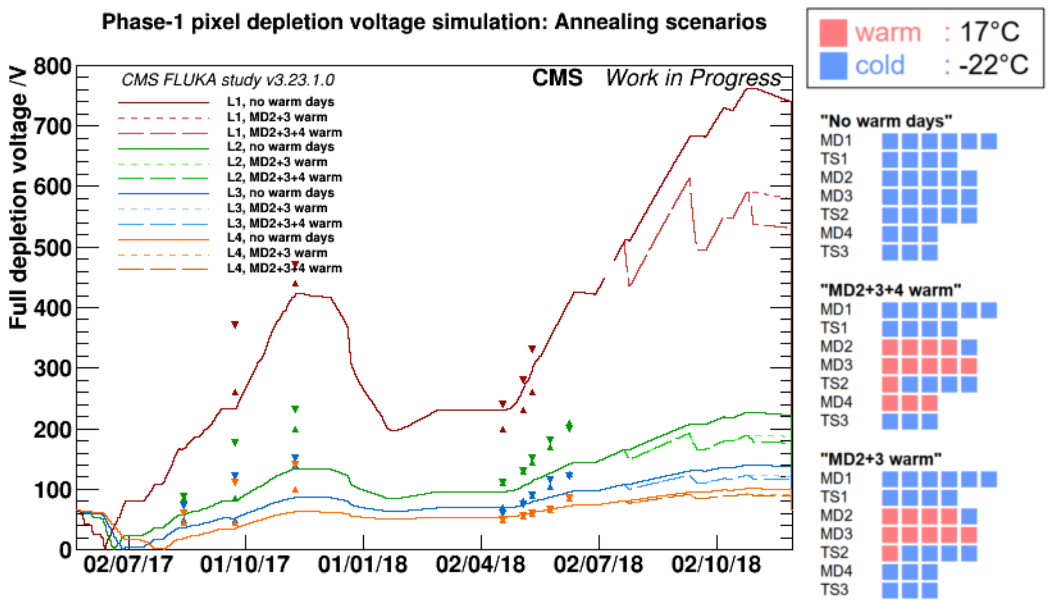


Figure 6.14.: Depletion voltage annealing scenarios considered before MD2. Compared are different combinations of warm days in MD2, MD3, and optionally MD4. A graphic representation of the warm days (red) is given on the right side. 17 °C correspond to the assumed maximum possible warm-up temperature. As a reference, a curve with no annealing is plotted.

was attempted in the ensuing MD2. In Figure 6.15, different warm-up temperatures are compared, as it was not clear beforehand which temperatures could be achieved. During the warm-up procedure the temperature stagnated around 12 °C due to passive cooling

[3] The data is available within a matter of a few days – with original calibration settings – for analysis purposes. Often a second iteration is issued with optimised calibrations. However this step may take up to several months.

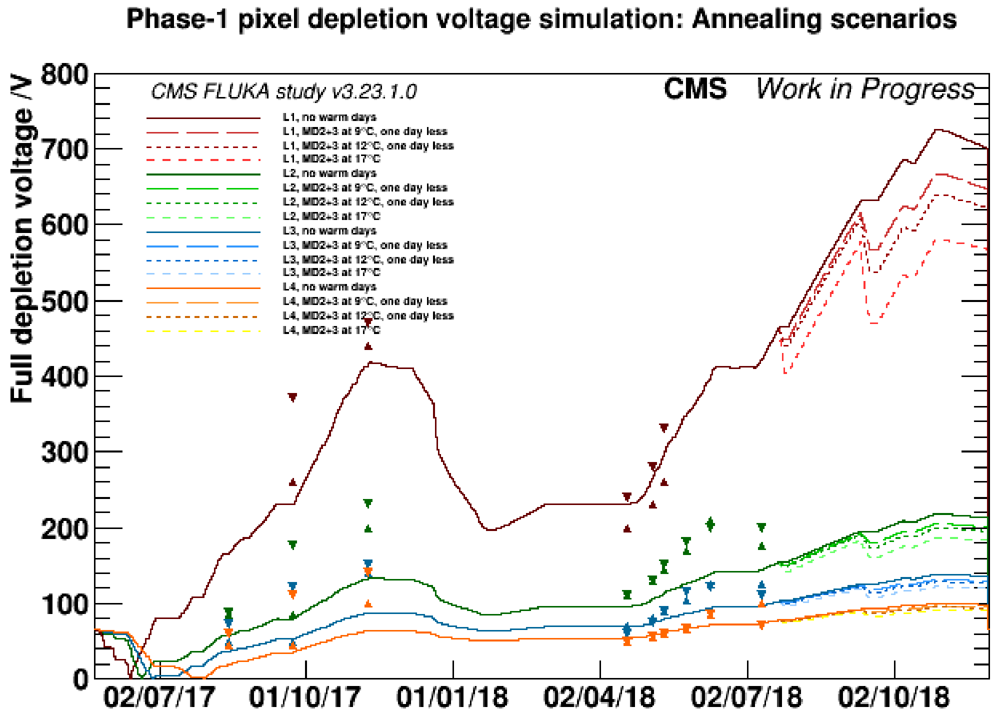


Figure 6.15.: The impact on depletion voltage of warm days in MD2 and MD3 with annealing temperatures at 9, 12, and 17°C are compared with no annealing. Details are given in Section 6.4.1.1.

from the surrounding strip tracker. This meant collecting fewer days of annealing at a lower temperature than expected.

A beneficial effect of the warm-up procedure was not clearly visible in the data afterwards. No reliable CC/CS data points could be extracted for layer 1 (L1) in the period just before the warm-up, thus the temperature impact on depletion voltage cannot be quantified regarding the L1 data. L2-4 data points show annealing behaviour in terms of depletion voltage, however effects in these outer layers were of secondary importance.

Complementary monitoring parameters describing the performance of the sensor and the chip, like CC, CS, CCE, resolution, or the efficiency with which hits are detected, should always be studied in addition to the depletion voltage predictions. A detailed study of these parameters did not show notable changes for the critical L1 after the annealing attempt in MD2.

Predictions for a potential warm-up at 12 °C in MD3 displayed a potential depletion voltage drop in L1 by only 50 V. Neither the depletion voltage nor the complementary parameter studies promised large improvements from the complicated warm-up procedure. It was decided to instead raise the bias voltage by 50 V to 450 V to effectively establish the same leeway between $V_{\text{bias}}$ and $V_{\text{dep}}$.

### 6.4.2. Phase-1 leakage current

The modelling of the leakage current in the present Phase-1 pixel tracker as a further important operational parameter is discussed in the following. All input parameters were described in the previous sections. Like the depletion voltage, the leakage current was modelled for each of the four barrel layers using the average layer radii. Fluence was extracted from the FLUKA matrix for $z = 0$ cm.

$I_{\mathrm{leak}}$ was calculated at $T_{\mathrm{ref}} = 20\,°\mathrm{C}$ in the day by day manner described in Section 5.1, including annealing at the average sensor temperature of the day, $T_{\mathrm{A}} = T_{\mathrm{sil}}$. The result was then scaled from $T_{\mathrm{ref}}$ to the measurement temperature of each day, again identical to $T_{\mathrm{sil}}$.

The temperature spread within one layer discussed in Section 6.1.4.2 is visible in the $I_{\mathrm{leak}}$ data. About a factor of 2 or more lies between the highest and lowest current measurements, which, if directly translated to a temperature difference according to Equation (2.48), corresponds to a temperature difference of 7 K between the warmest and coldest group of modules. The L3 $I_{\mathrm{leak}}$ data displays a noticeably smaller spread compared to the other layers. The cooling loop arrangement in L3 has incoming (warmer) and outgoing (colder) pipes geometrically adjacent to each other and temperatures assimilate between them. In all other layers the cooling loops are arranged with incoming pipes next to each other, and outgoing pipes next to each other, thereby creating warmer and colder areas in the layer. The resulting temperature modulation over $\varphi$ is clearly visible in the cooling loop data of L1, L2, and L4.

The leakage current model curves in Figure 6.16 and Figure 6.17 reflect leakage current calculated from the average temperature of the modules. This is not identical to the average leakage current of the modules due to the intricate temperature dependence in two ways - annealing history and measurement temperature - described in Section 3.6. However the average leakage current is expected to lie within the upper and lower band limits given in the plots.

A temperature variation of $\pm 2$ K, reflecting the temperature spread observed in the pixel mock-up, was taken as an input for the separate calculation of the upper and lower band limits.

All four layers show deviations between model and data. Yet the shape of $I_{\mathrm{leak}}$ data evolution is well described – the ratio between the data's mean value and the model is fairly constant for the whole measurement period within one layer. The model underestimates the data by approximately a factor of 1.3 in L1, 2.4 in L2, and 1.8 in both L3 and L4. These factors depend on the chosen temperature scenario; however they are not explainable by merely a wrong temperature estimation. Unrealistically high temperatures around 0 °C would be the conclusion, contradicting all studies which have been carried out to estimate module temperatures.

As leakage current is very sensitive to temperature, one could presume that averaging the temperature over a whole day introduces a considerable systematic uncertainty. Leakage current annealing at a given average temperature is slower compared with annealing at fluctuating temperatures around this average. The impact of realistic temperature fluctuations proved negligible[4].

[4] The impact of realistic temperature fluctuations within a day on the depletion voltage prediction is even smaller.

In conclusion, the missing factors are very unlikely to originate from a single source. This is underpinned by the observation that the factors display no stringent increase (or stringent decrease) from one layer to the next as one would expect for something solely related to one parameter out of surface area or volume, fluence scaling, or similar.

The pragmatic approach of applying a multiplication factor leads to accurate descriptions of the leakage current data for all four barrel layers and therefore allows meaningful predictions of the future leakage current evolution in the pixel tracker.

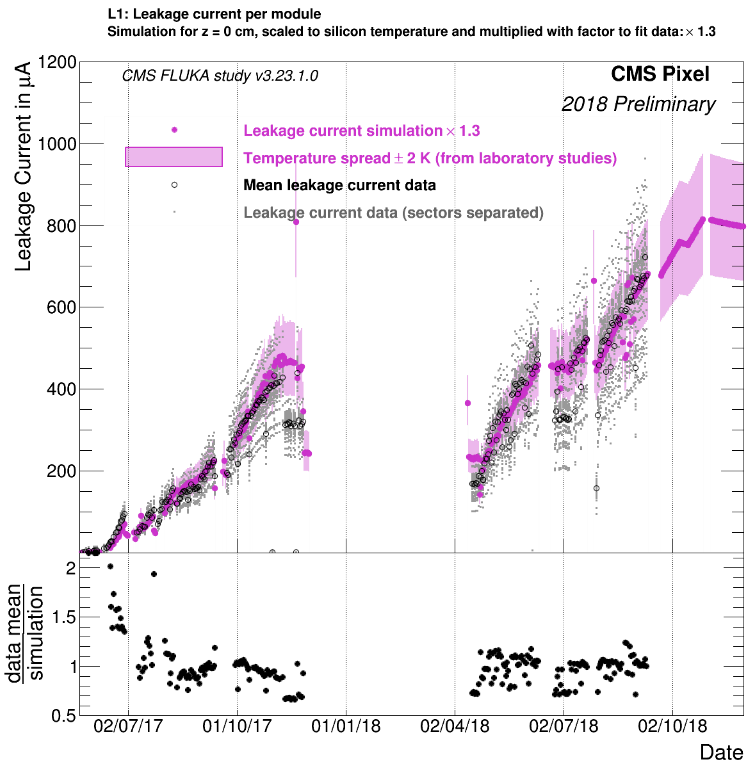


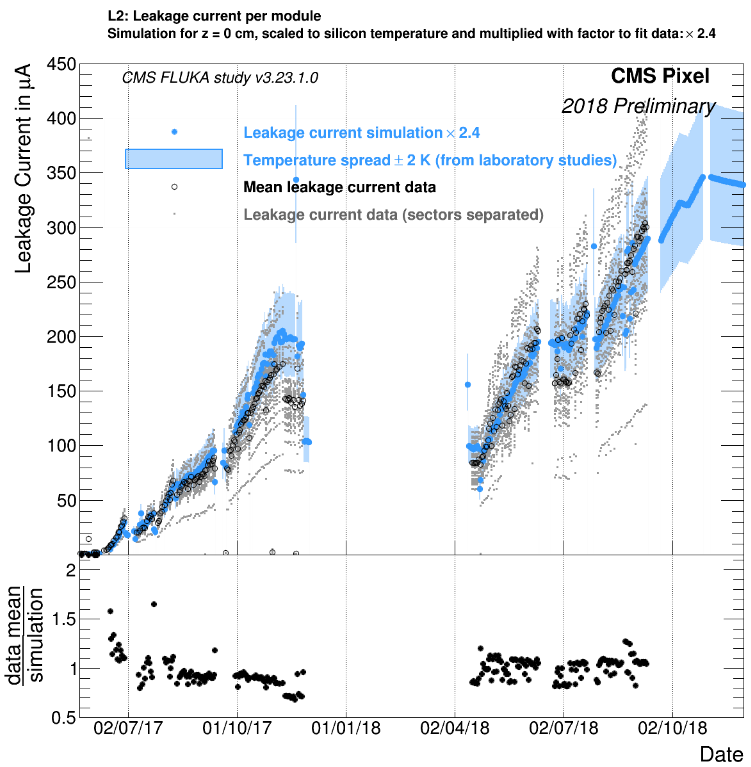


Figure 6.16.: Pixel Phase-1 leakage current in the barrel layers 1 and 2. Data is per HV group and its average is also given. Both data and model are scaled to $T_{\mathrm{sil}}$ for each day. Multiplication factors were applied to the simulation results to scale them to the data.

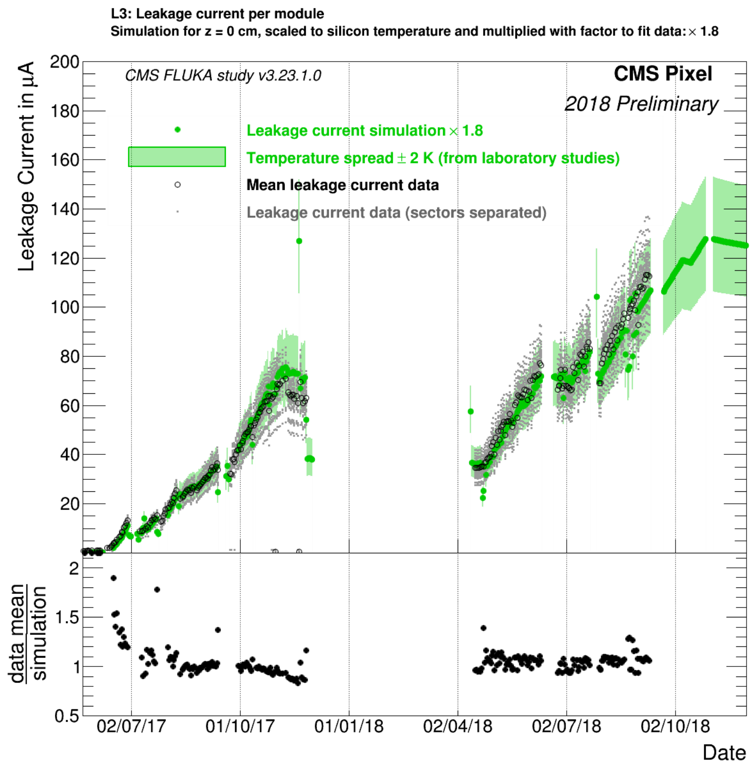


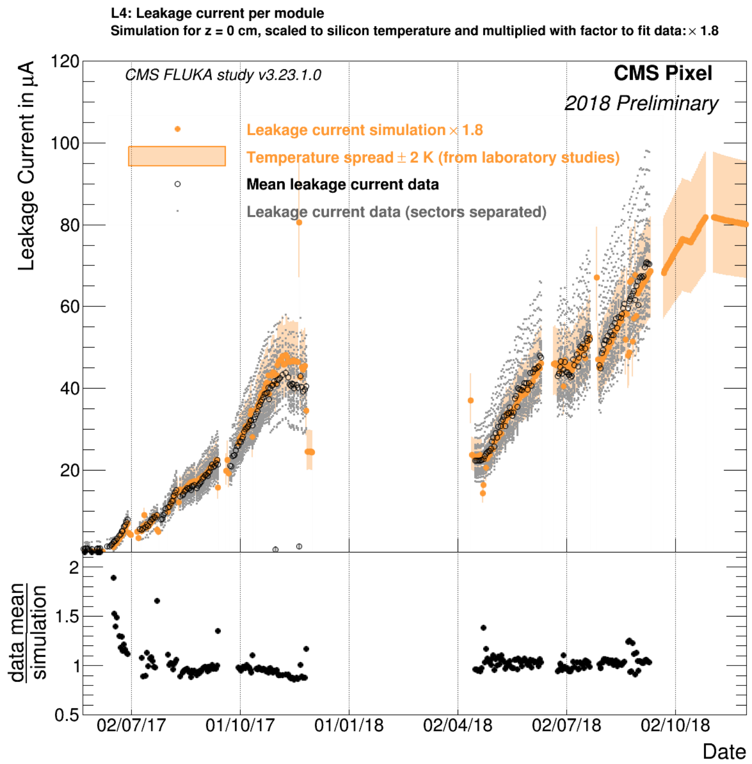


Figure 6.17.: Pixel Phase-1 leakage current in the barrel layers 3 and 4. Data is per HV group and its average is also given. Both data and model are scaled to $T_{sil}$ for each day. Multiplication factors were applied to the simulation results to scale them to the data.

### 6.4.3. Investigation on $z$ distributions of several parameters

Questions have been raised about the $z$ distribution of the leakage current data and simulation in the pixel tracker. Since the leakage current data is read out per HV group, which includes multiple modules at potentially different temperatures, this cannot be tackled by a direct approach. However, hypothetical differences of the leakage current in $z$ direction would arise from either fluence or temperature gradients in $z$. Further, a parameter which is accessible in a $z$-resolved way is the depletion voltage.

The mock-up studies led to the conclusion that temperature drops by several Kelvin along the distance of a cooling loop, while the $CO_2$ traverses part of a barrel layer. The temperature drop will roughly cancel out between adjacent cooling pipe sections due to the change of flow direction after each turn in the zigzag layout. When averaging over a whole layer, the temperature should thus be fairly independent of $z$ (assuming no exceptional cases like areas with degraded cooling contacts).

Fluence expectations are based on the FLUKA simulation. The available FLUKA file for Phase-1 (see Section 6.1.1) shows a striking uniformity of fluence in $z$ within the pixel tracker volume, as can be seen in Figure 6.18. A slight exception is L1, where the charged particle fluence is higher nearer the IP. The predicted impact on the simulated L1 depletion voltages at different $z$ positions can be seen in Figure 6.19. It is predicted to result in a depletion voltage difference of 60 V at the most. The $z$ slices for which the FLUKA values were plotted correspond to the average module centre $z$ positions, listed in Table 6.3.

| Barrel minus | | | | | | | | Barrel plus |
|---|---|---|---|---|---|---|---|---|
| -4 | -3 | -2 | -1 | IP | +1 | +2 | +3 | +4 |
| -23.7 cm | -17.1 cm | -10.4 cm | -3.7 cm | 0 cm | 3.0 cm | 9.7 cm | 16.4 cm | 23.1 cm |

Table 6.3.: Average $z$ position of modules in the Phase-1 pixel barrel for which the FLUKA information in Figure 6.18 and Figure 6.19 was extracted.

Breaking down the depletion voltage data of a full bias scan into $z$-resolved information would allow to check if it is indeed roughly constant along the full pixel barrel length. It could give an indication whether the fluence simulation and temperature laboratory measurements describe the real detector environment well. The final cross-check will be left for future studies as the necessary data was not available at the time of writing.

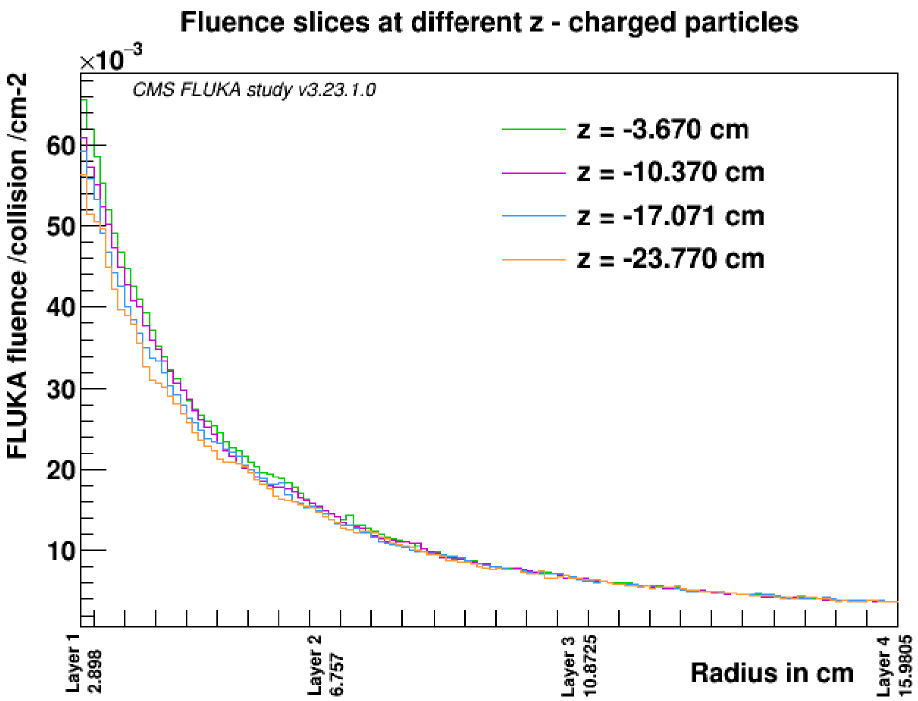


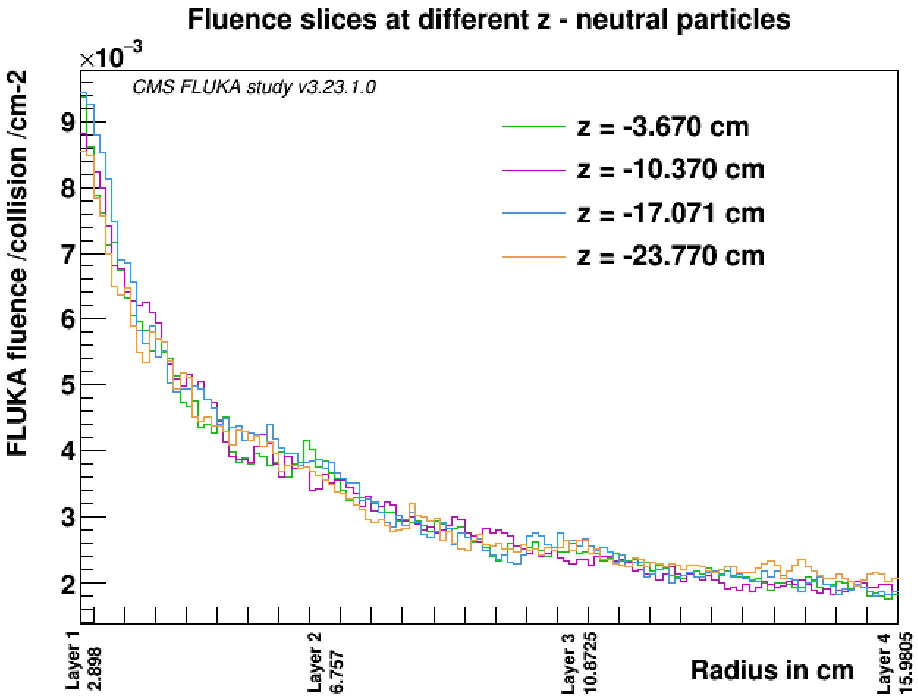


Figure 6.18.: Simulated FLUKA fluence of neither charged nor neutral particles shows any significant difference along the $z$ range of the pixel tracker for a given radius $r$. Fluctuations are within statistical uncertainties.

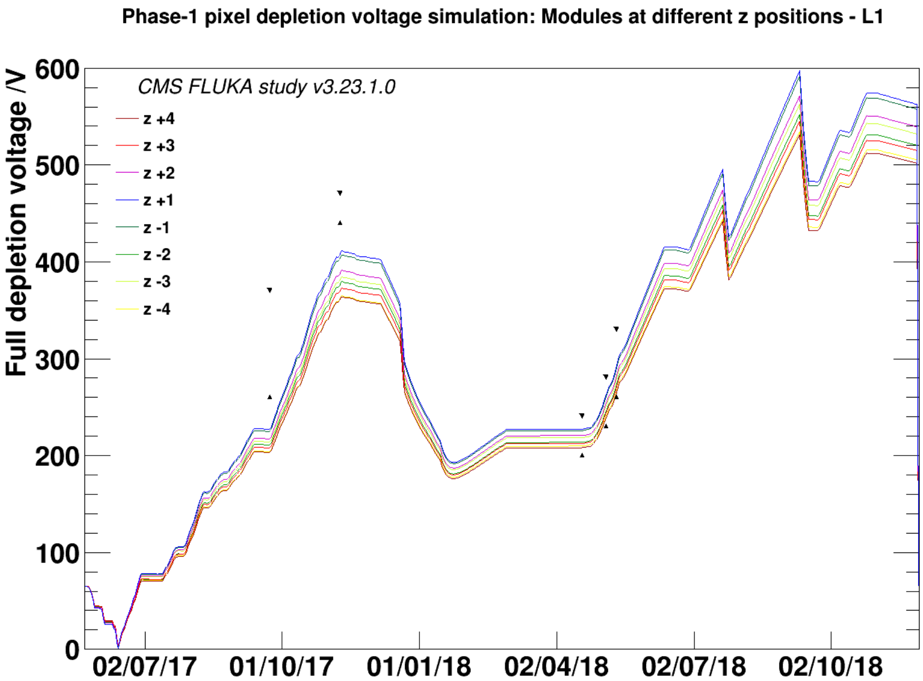


Figure 6.19.: Pixel depletion voltage simulations for $z \neq 0$. FLUKA values were extracted at the average $z$ position of the barrel modules, as described in Table 6.3. FLUKA bin width is 1 cm in $z$. Even though the depletion voltage for $z = \pm 1$ is higher due to the higher fluences in L1 near the IP, the difference to the modules at higher $z$ positions is 60 V at the most.

## 6.5. Predictions for after LS2

With the tool's results anchored to the available Phase-1 data until 2018, predictions for the evolution of $I_{\text{leak}}$ and $V_{\text{dep}}$ during the upcoming Run 3 were made.

The time scope was extended until the end of 2023, to contain the expected schedule for LS2 and Run 3. For the future temperature scenario in Figure 6.20, it was assumed that the sensor temperatures will remain comparable to those in 2018. A period of 30 days at room temperature during each of the YETS of Run 3 is included. For all YETS in Run 3 the duration of four months (December to March) was allocated. In each year of Run 3, four generic TS of five days each were assumed, during which the detector is off and kept cold.

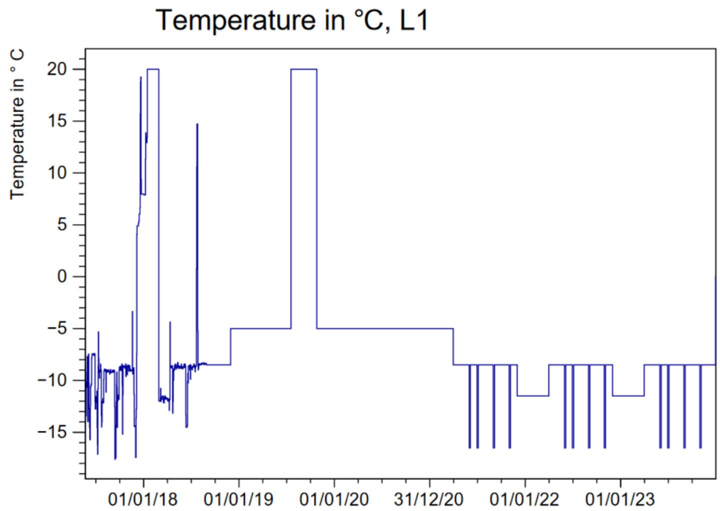


Figure 6.20.: Silicon temperature scenario (example given for L1) used as input for the modelling of the depletion voltage and leakage current evolution until 2023.

A luminosity scenario resulting in a total integrated luminosity of 400 fb$^{-}$1 delivered during Run 3 was chosen, corresponding to a realistic to slightly-above-expectations estimate. It is displayed in Figure 6.21.

The depletion voltage evolution of the pixel detector is shown in Figure 6.22. L1 will be exchanged in LS2, which is why its depletion voltage and leakage current model curves restart from an unirradiated state in 2021. However since the concept of depletion voltage is no longer applicable for L1 in Run 3, the prediction can only be sensibly interpreted for the outer layers.

The necessary bias voltage in L2 will approach the present power supply limit of 600 V according to the projections in Figure 6.22. During LS2 the power supply units will be upgraded to allow a maximum bias voltage of 800 V. Sensors and full modules have been shown to withstand these bias voltages.

In Run 3 the HV power supply limit of 12 W will be a critical value. One power supply is responsible for the combined sensor power of one HV group. Therefore the leakage current of a HV group and its set bias voltage together have to stay below this 12 W limit. The number of modules differs from one HV group to the next. Table 6.4 lists the minimum, maximum and average number of modules per HV group for each of the layers. Using this

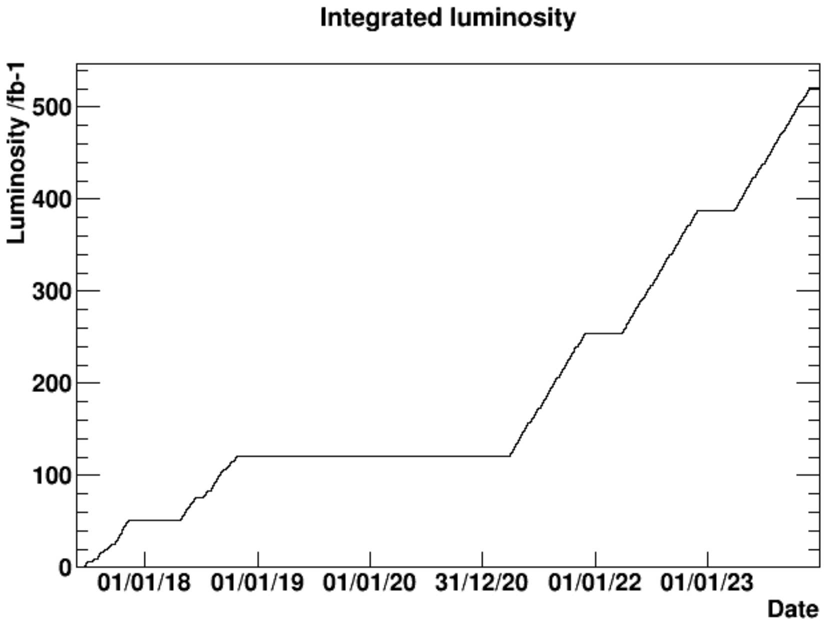


Figure 6.21.: Delivered integrated luminosity scenarios used as input for the modelling of the depletion voltage and leakage current evolution until 2023.

| | Average | Minimum | Maximum |
|---|---|---|---|
| L1 | 3 | 3 | 3 |
| L2 | 7 | 4 | 8 |
| L3 | 11 | 8 | 12 |
| L4 | 16 | 16 | 16 |

Table 6.4.: Number of modules per HV group for each of the four Phase-1 pixel barrel layers. Average (exact), minimum and maximum are listed.

information the leakage current per HV group was modelled for average, minimum and maximum numbers of modules. Again the same temperature and integrated luminosity scenario was applied. The results are given in Figure 6.23 and Figure 6.24.

At 600 V, the leakage current in a HV group must remain below $12\,\mathrm{W}/600\,\mathrm{V} = 20\,\mathrm{mA}$. At 800 V the leakage current limit is even at $12\,\mathrm{W}/800\,\mathrm{V} = 15\,\mathrm{mA}$.

In case of L1 and L2, these limits will have to be closely monitored during Run 3. An option would be to reduce the cooling set point in the pixel detector further, thereby scaling the leakage current to lower values.

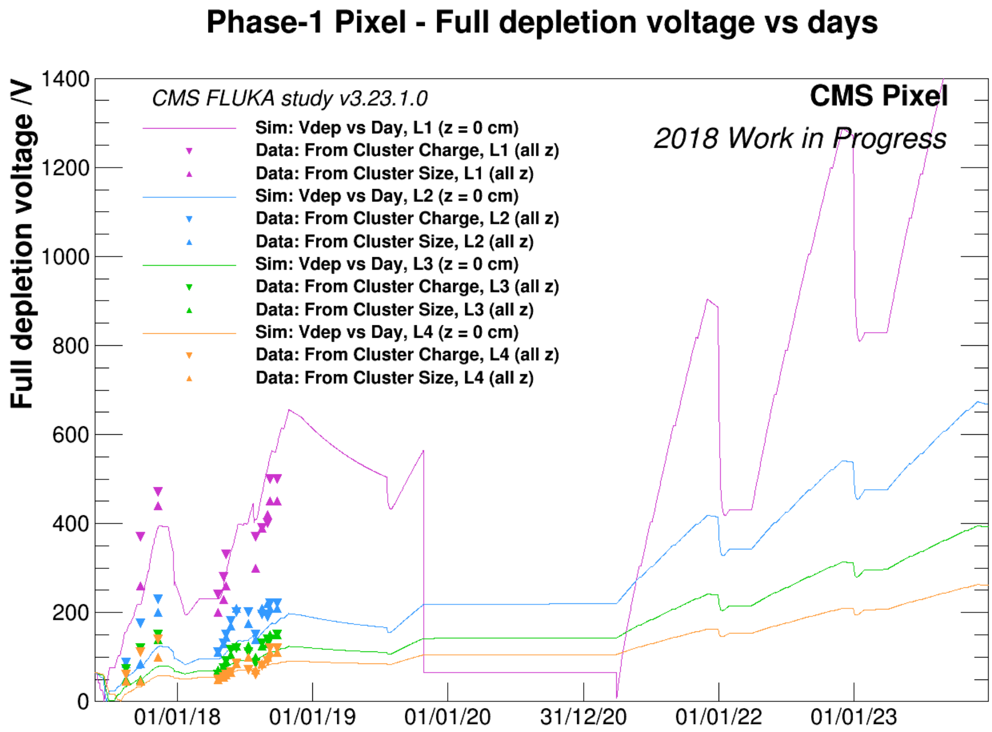


Figure 6.22.: Pixel depletion voltage evolution prediction until 2023.

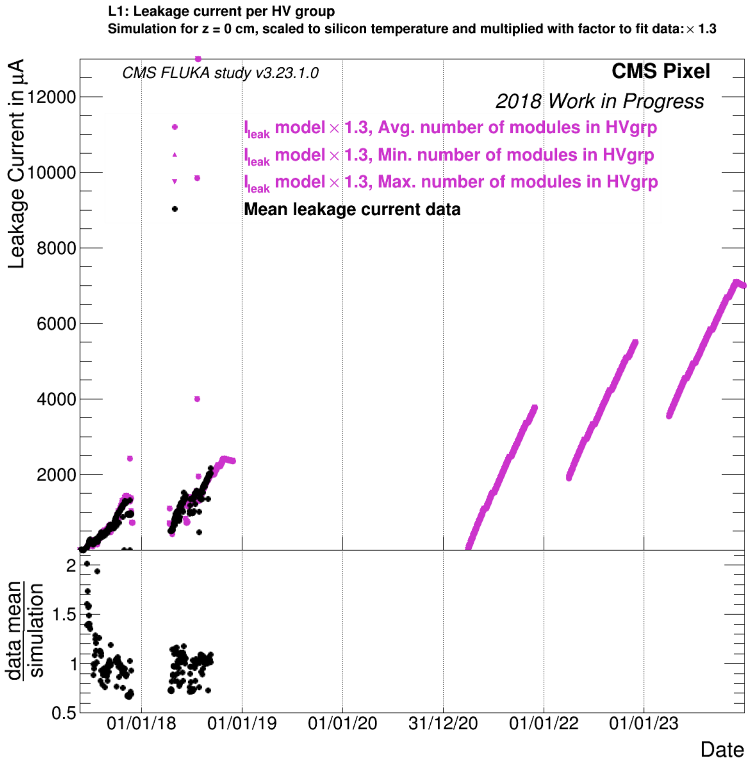


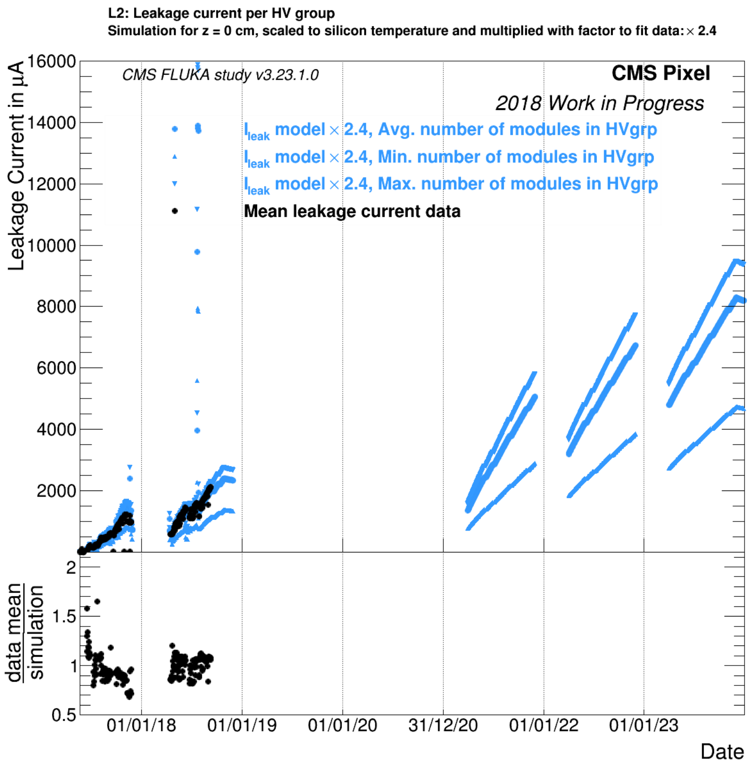


Figure 6.23.: Predictions of the leakage current evolution per HV group until 2023 for L1 and L2. The average, minimum, and maximum numbers of modules per HV group were considered, compare Table 6.4.

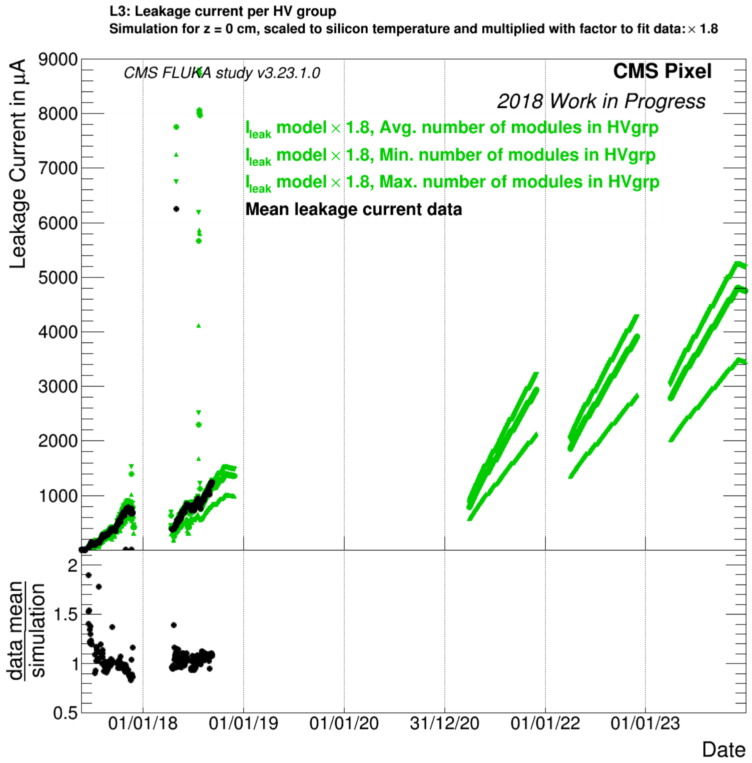


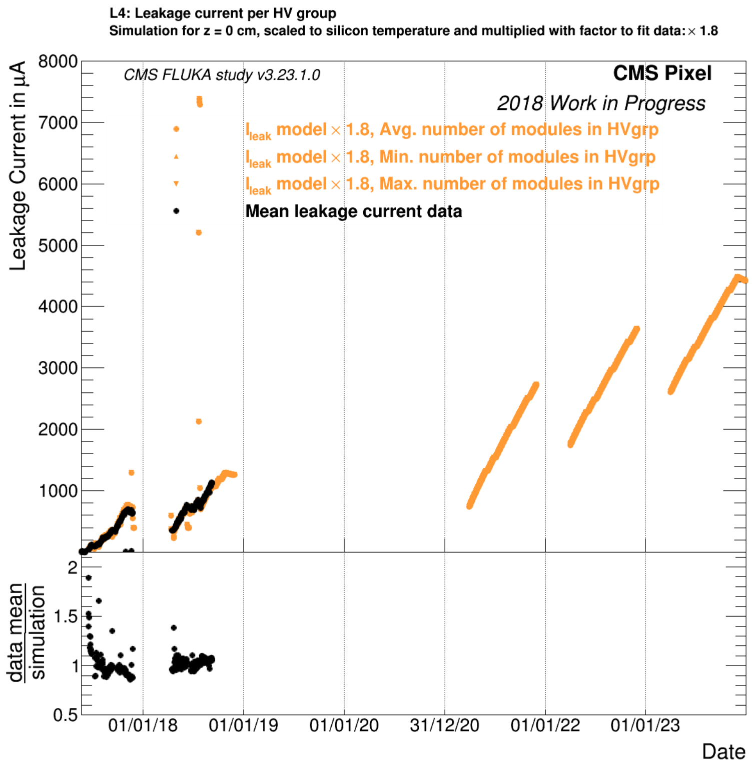


Figure 6.24.: Predictions of the leakage current evolution per HV group until 2023 for L3 and L4. The average, minimum, and maximum numbers of modules per HV group were considered, compare Table 6.4.

## 6.6. Outlook

The modelling tool for the pixel has proven its applicability for the prediction of the important detector parameters depletion voltage and leakage current. It was used multiple times to define operational procedures.

Current ideas for further studies include the adaptation of the curvature algorithm to the Phase-1 CC and CS shapes to extract the depletion voltage, as described in Section 6.1.6. A study of the $z$ distribution of the depletion voltage data could be interesting for the reasons explained in Section 6.4.3. Another interesting topic is the attempt to extract a pixel specific Hamburg parameter set from Phase-1 data. Frequently performed mini bias scans during the past months and very recent results of the L2 mock-up, which substantiated the temperature estimations considerably, made this a viable option.

The task of maintaining the code and providing the Pixel Monitoring group with information based on the simulation has recently been adopted by the Particle Physics and Detector Development group of the Hamburg university to ensure future continuation.

# 7. Summary

Leakage current and depletion voltage are important operational parameters in the CMS strip and pixel tracker. Their evolution with radiation in the detector is continuously monitored.

A tool for modelling of the leakage current and depletion voltage of the strip tracker had been developed in [1] (Section 5.1). The parametrisations of the depletion voltage and leakage current were taken from [2]. Work on the existing strip tracker tool was resumed and previous results were successfully reproduced. A comparison with available depletion voltage detector data was made (Section 5.3) and a very good agreement between simulation and data was found. New projections of the expected depletion voltage, leakage current, and thermal runaway occurrences in the strip tracker for different integrated luminosity scenarios until 2023 (end of Run 3) were provided (Section 5.4).

Tying in with the strip tracker modelling tool, a similar tool was established for the pixel tracker in the scope of this thesis (Chapter 6). All necessary input parameters were assessed and laboratory studies of the thermal mock-up pixel barrel layer 2, performed by the pixel tracker community, provided valuable insight to the silicon sensor temperatures in the detector (Section 6.1.4.2). The depletion voltage and leakage current results were compared to available detector data (Section 6.3.1 and Section 6.4). The good agreement between data and simulation allows predictions for future evolution of these two observables.

Several times during the past year, predictions for the pixel tracker depletion voltage evolution in 2018 served as a basis for decisions on operational procedures (Section 6.4.1.1). A warm-up of the detector was performed based on the beneficial depletion voltage annealing prospects the tool yielded. Predictions of the evolution of leakage current and depletion voltage in the pixel tracker during Run 3 were provided (Section 6.5).

Both tools are in a good state for reliable predictions and their results will continue to make an important contribution to the tracker monitoring.

# 8. Acknowledgements

I would like to express my profound gratitude to Professor Dr. Thomas Müller for the opportunity to write my master's thesis at CERN. Further I wish to thank Professor Dr. Ulrich Husemann for reviewing this thesis.

For the constant support and expert advise I have received from Dr. Frank Hartmann and Dr. Erik Butz I am exceptionally grateful. Equally thankful I am for the essential help and initial guidance from Dr. Christian Barth.

Advice and untiring help from Dr. Jory Sonneveld, Dr. Benedikt Vormwald, Dr. Annapaola de Cosa, and the Pixel Monitoring Group have been of indispensable worth. I would like to specially thank Dr. Andrea Venturi for asking many critical questions. I am also grateful to Dr. Fengwangdong Zhang for detailed investigations of leakage current and temperature measurements. Special thanks to Max Rauch, Dr. Nicola Bachetta, and everyone involved in the Pixel Thermal Mock-Up laboratory studies, for valuable insights.

Dr. Sophie Mallows and the BRIL RS group provided vital input to my work and I am grateful for many helpful discussions. The provision of the high voltage bias scan data by Dr. Márton Bartók was much appreciated. Of great help have been the algorithms provided by Dr. Jean-Laurent Agram, Dr. Nicolas Tonon, and Dr. Sinan Sagir. Further I would like to thank Finn Feindt, Dr. Tilman Rohe, Dr. János Karancsi, and Dr. Michael Moll for fruitful correspondences.

I wish to thank my family for their absolute love and support.

# Bibliography


[1] C. Barth. “Physikalische Analyse des Ansprechverhaltens des CMS Siliziumdetektors beim Betrieb am LHC”. PhD thesis. Karlsruhe Institute of Technology, 2013.

[2] M. Moll. “Radiation damage in silicon particle detectors – Microscopic defects and macroscopic properties”. PhD thesis. Universität Hamburg, 1999.

[3] I. Bejar Alonso et al. *HiLumi LHC Technical Design Report*. CERN-ACC-2015-0140. 2015. URL: https://cds.cern.ch/record/2069130/files/CERN-ACC-2015-0140.pdf.

[4] F. Hartmann. *Evolution of Silicon Sensor Technology in Particle Physics*. Springer Tracts in Modern Physics ; 275. 2017.

[5] RD50 Collaboration. *R&D Proposal: Development of radiation hard semiconductor devices for very high luminosity colliders*. LHCC 2002-003, P6–1/36. 2002. URL: http://rd50.web.cern.ch/rd50/doc/status-reports/LHCC-2002-003-RD-proposal.pdf.

[6] S. Hunklinger. *Festkörperphysik*. Oldenbourg. München, 3rd edition, 2012.

[7] G. Lutz. *Semiconductor radiation detectors : device physics*. 2nd print of the 1st ed. Berlin: Springer, 2007. ISBN: 978-3-540-71678-5; 3-540-71678-5.

[8] S. M. Sze and K. K. Ng. *Physics of semiconductor devices*. 3. ed. Wiley-Interscience, 2007. ISBN: 0-471-14323-5; 978-0-471-14323-9.

[9] C.C. Hu. *Modern Semiconductor Devices for Integrated Circuits*. 2010. URL: https://people.eecs.berkeley.edu/~hu/Chenming-Hu_ch1.pdf.

[10] H.A. Bethe. *Zur Theorie des Durchgangs schneller Korpuskularstrahlen durch Materie*. Ann. Phys. 5, 325 (1930).

[11] C. Amsler et al. (Particle Data Group). *Passage of particles through matter*. Physics Letters B667, 1 (2008) and 2009 partial update for the 2010 edition. URL: http://pdg.lbl.gov/2009/reviews/rpp2009-rev-passage-particles-matter.pdf.

[12] H. Bichsel. *Straggling in Thin Silicon Detectors*. Rev.Mod.Phys. 60, 663-699. 1988. DOI: 10.1103/RevModPhys.60.663.

[13] W. Shockley and W.T. Read. *Statistics of the Recombinations of Holes and Electrons*. Physical Review. 87 (5): 835–842. 1952. DOI: 10.1103/PhysRev.87.835.

[14] R.N. Hall. *Electron-hole recombination in Germanium*. Phys. Rev. 87 (1952), pp. 387. 1952.

[15] A. Chilingarov. *Intrinsic concentration and generation current temperature dependence*. Technical Note. 2011. URL: http://eprints.lancs.ac.uk/39969/3/Ni_and_ITdependence.pdf.

[16] R. Wunstorf. “Systematische Untersuchungen zur Strahlenresistenz von Silizium-Detektoren für die Verwendung in Hochenergiephysik-Experimenten”. PhD thesis. Universität Hamburg, 1992.

[17] F. Hartmann. *Evolution of Silicon Parameters due to Irradiation at the LHC*. Proceedings of "The 20th Anniversary International Workshop on Vertex Detectors" (Vertex 2011) Rust, Lake Neusiedl, Austria. Published online at http://pos.sissa.it/cgi-bin/reader/conf.cgi?confid=137., id.36.

[18] T. Rohe. *Pixel Sensor Radiation Hardness*. PIRE 2011 Collaboration Meeting. October 2011. URL: `https://indico.cern.ch/event/158991/contributions/221932/`.

[19] J. Schwandt et al. *Surface effects in segmented silicon sensors*. Nuclear Instruments and Methods in Physics Research Section A: Accelerators, Spectrometers, Detectors and Associated Equipment Volume 845, pp 159-163. 2016. DOI: `10.1016/j.nima.2016.06.032`.

[20] RD50 Collaboration. *RD50 Status Report 2009/2010 – Radiation hard semiconductor devices for very high luminosity colliders*. CERN-LHCC-2012-010, LHCC-SR-004. URL: `https://cdsweb.cern.ch/record/1455062/files/LHCC-SR-004.pdf`.

[21] R. Radu et al. *Radiation damage in n-type silicon diodes after electron irradiation with energies between 1.5 MeV and 15 MeV*. NIM A730, 84–90. 2013. URL: `https://doi.org/10.1016/j.nima.2013.04.080`.

[22] T. Rohe. *Talk on Radiation Damage in Silicon Sensors for Particle Tracking*. December 6, 2011. URL: `https://indico.cern.ch/event/158991/contributions/221932/attachments/179559/252509/rohe_pire_2011.pdf`.

[23] M. Huhtinen. *Simulation of defect formation in different hadron irradiation environments*. Nuclear Instruments and Methods in Physics Research Section A: Accelerators, Spectrometers, Detectors and Associated Equipment, Volume 491, Issues 1–2, 194-215. 2002. DOI: `10.1016/S0168-9002(02)01227-5`.

[24] J. Lindhard and V. Nielson. *Nuclear collisions and ionisation fluctuations in charged particle detectors*. Physics Letters, Volume 2, Issue 5, pp. 209-211. 1962. DOI: `10.1016/0031-9163(62)90229-9`.

[25] A. Vasilescu (INPE Bucharest), G. Lindstroem (University of Hamburg). *Displacement damage in silicon*. Online compilation. 2000. URL: `https://rd50.web.cern.ch/rd50/NIEL/default.html`.

[26] A. Vasilescu et al. *Fluence normalization based on the NIEL scaling hypothesis*. 3rd ROSE Workshop on Radiation Hardening of Silicon Detectors, DESY-PROCEEDINGS-1998-02. February 1998. URL: `https://indico.cern.ch/event/158991/contributions/221932/attachments/179559/252509/rohe_pire_2011.pdf`.

[27] M. Huhtinen. *Simulation of Non-Ionising Energy Loss and Defect Formation in Silicon*. ROSE/TN/2001-02, CERN, CH-1211 Geneva 23, Switzerland. 2001.

[28] E. Fretwurst et al. *Radiation hardness of silicon detectors for applications in high-energy physics experiments*. Journal of Optoerlectronics and Advanced Mateials Vol. 2, No. 5, p. 575-588. 2000. URL: `https://joam.inoe.ro/arhiva/pdf2_5/Fretwurst.pdf`.

[29] The ROSE Collaboration, R&D on Silicon for future Experiments. *3rd RD48 Status Report*. CERN/LHCC 2000-009, LEB Status Report/RD48. 1999.

[30] RD50 Collaboration. *RD50 Status Report 2002/2003 – Radiation hard semiconductor devices for very high luminosity colliders*. CERN-LHCC-2003-058 and LHCC-RD-002. URL: `http://rd50.web.cern.ch/rd50/doc/status-reports/031114-RD50-Status-Report-2003.pdf`.

[31] M. Swartz. *A Detailed Simulation of the CMS Pixel Sensor*. CMS-NOTE-2002-027. 2002. URL: `https://cds.cern.ch/record/687440`.

[32] M. Moll et al. *Relation between microscopic defects and macroscopic changes in silicon detector properties after hadron irradiation*. Nuclear Instruments and Methods in Physics Research B 186 (2002) 100–110.

[33] CMS General Meeting. *Plot Approval Session*. November 16, 2017. URL: `https://indico.cern.ch/event/678015/contributions/2793648/attachments/1559773/2454940/Strip_radiation_damage_plot_approvalNov2017.pdf`.

[34] E. Mobs. *The CERN accelerator complex*. 28. August 2018. URL: `https://cds.cern.ch/record/2636343`.

[35] P. Higgs. *Broken Symmetries and the Masses of Gauge Bosons*. Physical Review Letters 13 (16), pp. 508-509. accessed July 2, 2015. 1964. URL: `http://journals.aps.org/prl/pdf/10.1103/PhysRevLett.13.321`.

[36] G. Guralnik, C. Hagen, and T. Kibble. *Global Conservation Laws and Massless Particles*. Physical Review Letters 13 (20), pp. 585-587. accessed July 2, 2015. 1964. URL: `http://journals.aps.org/prl/pdf/10.1103/PhysRevLett.13.585`.

[37] The CMS collaboration. *Observation of a New Particle with a Mass of 125 GeV*. Phys.Lett. B716 (2012), pp. 30-61. July 4, 2012. URL: `%7Bhttp://inspirehep.net/record/1124338%7D`.

[38] The ATLAS collaboration. *Observation of a new particle in the search for the Standard Model Higgs boson with the ATLAS detector at the LHC*. Phys.Lett. B716 (2012), pp. 1-29. August 31, 2012. URL: `%7Bhttp://inspirehep.net/record/1124337%7D`.

[39] The CMS Collaboration. *CMS Physics, Technical Design Report – Volume 1: Detector Performance and Software*. CERN-LHCC-2006-001, CMS-TDR-8.1. 2006. URL: `http://cdsweb.cern.ch/record/922757/files/lhcc-2006-001.pdf`.

[40] The CMS Collaboration. *Particle-Flow Event Reconstruction in CMS and Performance for Jets, Taus, and MET*. CMS Physics Analysis Summary, CMS-PAS-PFT-09-001. 2009. URL: `https://cds.cern.ch/record/1194487`.

[41] The CMS Collaboration. *Particle-flow reconstruction and global event description with the CMS detector*. CMS-PRF-14-001, CERN-EP-2017-110. 2017. URL: `arXiv:1706.04965`.

[42] The CMS Collaboration. *CMS TriDAS project : Technical Design Report, Volume 1: The Trigger Systems*. CERN-LHCC-2000-038, CMS-TDR-6-1. 2000. URL: `https://cds.cern.ch/record/706847`.

[43] The CMS Collaboration. *CMS The TriDAS Project : Technical Design Report, Volume 2: Data Acquisition and High-Level Trigger*. CERN-LHCC-2002-026, CMS-TDR-6. 2002. URL: http://cdsweb.cern.ch/record/578006/files/cer-2336481.pdf.

[44] The CMS Collaboration. *Performance of the new DAQ system of the CMS experiment for run-2*. 20th IEEE-NPSS Real Time Conference, Padua, Italy. June 2016. URL: https://cds.cern.ch/record/2264424.

[45] *Computing*. 2012. URL: https://cds.cern.ch/record/1997391.

[46] The CMS Collaboration. *The CMS muon project : Technical Design Report*. CERN-LHCC-97-032, CMS-TDR-3. 1997. URL: https://cds.cern.ch/record/343814.

[47] The CMS Collaboration. *The CMS magnet project: Technical Design Report*. CERN-LHCC-97-010, CMS-TDR-1. 1997. URL: https://cds.cern.ch/record/331056.

[48] The CMS Collaboration. *The CMS hadron calorimeter project : Technical Design Report*. CERN-LHCC-1997-031, CMS-TDR-2. 1997. URL: https://cds.cern.ch/record/357153.

[49] J. Freeman. *Innovations for the CMS HCAL*. International Journal of Modern Physics A VOL. 25, NO. 12. 2010. DOI: 10.1142/S0217751X10049682.

[50] J.P. Merlo. *CMS hadronic forward calorimeter*. Nuclear Physics B - Proceedings Supplements, Volume 61, Issue 3 41-46. 1998. DOI: 10.1016/S0920-5632(97)00536-7.

[51] The CMS Collaboration. *The CMS electromagnetic calorimeter project : Technical Design Report*. CERN-LHCC-97-033, CMS-TDR-4. 1997. URL: https://cds.cern.ch/record/349375.

[52] J. Mašík. *Vertex and track reconstruction in ATLAS and CMS*. 14th International Conference on B-Physics at Hadron Machines, Bologna, Italy. April 2013. URL: https://cds.cern.ch/record/1563583/files/ATL-PHYS-PROC-2013-206.pdf.

[53] The CMS Collaboration. *Tracker Technical Design Report*. CERN/LHCC 98-6, CMS-TDR-5. 1998. URL: http://inspirehep.net/record/1614059/files/Tracker_TDR.pdf.

[54] The CMS Collaboration. *Addendum to the CMS Tracker TDR*. CERN/LHCC 2000-016, CMS-TDR-5 Addendum 1. 2000. URL: https://cds.cern.ch/record/490194/files/cer-2244540.pdf.

[55] The CMS Collaboration. *The CMS experiment at the CERN LHC*. JINST 3 (2008) S08004. 2008. URL: http://inspirehep.net/record/796887.

[56] The CMS Collaboration. *The Phase-2 Upgrade of the CMS Tracker – Technical Design Report*. CERN-LHCC-2017-009, CMS-TDR-014. 2017. URL: https://cds.cern.ch/record/2272264/files/CMS-TDR-014.pdf.

[57] E. Alagöz et al. *Annual Report 2005/06 – Particle Physics with CMS*. Physik-Institut der Universität Zürich. URL: https://www.physik.uzh.ch/en/reports/report2006.html.

[58] The CMS Collaboration. *The CMS pixel system*. Nuclear Instruments and Methods in Physics Research Section A: Accelerators, Spectrometers, Detectors and Associated Equipment Volume 579, Issue 2, 669-674. 2007. URL: https://doi.org/10.1016/j.nima.2007.05.270.

[59] The CMS Collaboration. *CMS Technical Design Report for the Pixel Detector Upgrade*. CERN-LHCC-2012-016, CMS-TDR-011. 2012. URL: https://cds.cern.ch/record/1481838/files/CMS-TDR-011.pdf.

[60] M. Rauch. "Thermal Characterization and Optimization of the Pixel Module Support Structure for the Phase-1 Upgrade of the CMS Pixel Detector". MA thesis. RWTH Aachen, 2015. URL: https://web.physik.rwth-aachen.de/service/wiki/pub/Feld/FeldAbschlussarbeiten/Masterarbeit_Max_Rauch.pdf.

[61] The CMS Collaboration. *Commissioning and Performance of the CMS Pixel Tracker with Cosmic Ray Muons*. CMS PAPER CFT-09-001, arXiv:0911.5434v2 [physics.ins-det]. 2010.

[62] C. Barth, E. Butz, and F. Hartmann. *Strip Tracker detector longevity*. Tracker Management Board. March 2018.

[63] A. Dierlamm. "Untersuchung zur Strahlenhärte von Silizium-Sensoren". IEKP-KA/03-23. PhD thesis. Universität Karlsruhe, 2003.

[64] T.T. Böhlen et al. *The FLUKA Code: Developments and Challenges for High Energy and Medical Applications*. Nuclear Data Sheets 120, 211-214. 2014.

[65] A. Ferrari et al. *FLUKA: A multi-particle transport code*. CERN-2005-10, INFN/TC-05/11, SLAC-R-773. 2005.

[66] J. Rahn. *Depletion Characteristics of Silicon Microstrip Detectors*. SCIPP 93/12. 1993. URL: http://cds.cern.ch/record/275959.

[67] B. Kotlinski. *Phase-1 pixel barrel radii*. Personal communication. May 9, 2018.

[68] BRIL Work Suite – brilcalc. URL: https://cms-service-lumi.web.cern.ch/cms-service-lumi/brilwsdoc.html#brilcalc.

[69] S. Sagir. *CMS Strip Tracker Radiation Damage Monitoring*. TWiki Documentation. accessed October 2018. URL: https://twiki.cern.ch/twiki/bin/viewauth/CMS/CMSStripTrackerRadiationDamageMonitoring#1_LUMI.

[70] M. Moll. *Hamburg model parameter sheet*. Personal communication (C. Barth, T. Rohe). November 3, 2017.

[71] L. Andricek et al. *Radiation Hard Strip Detectors on Oxygenated Silicon*. IEEE NSS-MIC, N19-2. 2001. URL: https://www.mpp.mpg.de/~sct/welcomeaux/papers/IEEETNS49_1117_1121.pdf.

[72] J. Renner. "Planning and validation of the thermal mock-up for the CMS Pixel Detector". MA thesis. Karlsruhe Institute of Technology, 2017. URL: https://ekp-invenio.physik.uni-karlsruhe.de/record/48898/files/EKP-2017-00025.pdf.

[73] A. de Cosa. *Pixel Monitoring*. gitlab repository. accessed October 2018. URL: https://gitlab.cern.ch/decosa/PixelMonitoring.

# A. Appendix

## A.1. Acronyms

**ALICE** A Large Ion Collider Experiment
**ATLAS** A Toroidal LHC Apparatus (Experiment)
**APV** Analogue pipeline voltage chip
**BPIX** Barrel pixel
**CERN** European Organisation for Nuclear Research
**CC** Cluster charge
**CCE** Charge collection efficiency
**CMS** Compact Muon Solenoid (Experiment)
**CS** Cluster size
**CSC** Cathode strip chambers
**D** Disk
**DCU** Detector control unit
**DOFZ** Diffused-oxygenated float-zone
**DT** Drift tubes
**ECAL** Electromagnetic calorimeter
**EYETS** Extended year-end technical stop
**FED** Front-end driver
**FPIX** Forward pixel
**FZ** Float-zone
**HAPS** Hybrid active pixel sensor
**HF** Hadronic forward calorimeter
**HCAL** Hadronic calorimeter
**HDI** High-density interconnect
**HL-LHC** High-luminosity LHC
**HLT** High-level trigger
**HO** Hadronic outer calorimeter
**HV** High voltage
**IP** Interaction point
**L** Layer
**LHC** Large Hadron Collider
**LHCb** LHC beauty (Experiment)
**LS** Long shutdown
**LV** Low voltage
**MD** Machine development
**MIP** Minimum ionising particle
**MPV** Most probable value
**NIEL** Non-ionising energy loss

**PSU** Power supply unit
**R** Ring
**ROC** Readout chip
**RPC** Resistive plate chambers
**SCR** Space charge region
**SMD** Surface mount device
**TBM** Token bit manager
**TCT** Transient current technique
**TEC** Tracker endcap
**TIB** Tracker inner barrel
**TID** Tracker inner disk
**TOB** Tracker outer barrel
**TS** Technical stop OR Thermal screen
**YETS** Year-end technical stop

## A.2. High voltage bias scans

### A.2.1. Phase-0

2010 Apr 05 – L3, D1
2010 Oct 28 – L1, L3, D1
2011 Mar 14, 16, 18 – L1, L3, D1
2011 May 15 – L1
2011 Jul 14 – L1
2011 Jul 28 – L3
2011 Aug 03 – L2
2011 Sep 07 – L1, D1
2011 Oct 12 – L1
2011 Oct 27 – L1
2011 Oct 30 – D1
2012 Apr 06 – L1-3, D1-2
2012 Jul 02 – L1-3, D1-2
2012 Aug 13 – L1
2012 Sep 27 – L1
2012 Dec 02 – L1-3, D1-2
2013 Jan 21 – L1-3, D1
2015 Jun 08 – L1-3, D1-2
2016 Apr 28 – L1-3, D1-2
2016 Jun 13 – L1-3, D1
2016 Jul 04 – L1-3, D1
2016 Oct 20 – L1-3, D1-2

### A.2.2. Phase-1

2017 May 25 – D1-3
2017 Aug 14 – L1-4
2017 Aug 23 – L1
2017 Aug 26 – L1,3,4
2017 Sep 23 – L1-4, D2
2017 Okt 04 – L1
2017 Okt 27 – L1
2017 Nov 09 – L1-4, D1-3
2018 Apr 19 – L1-4, D1-3 (Full)
2018 May 05 – L1-4, D1-3 (Mini)
2018 May 12 – L1-4, D1-3 (Mini)
2018 May 25 – L1-4, D1-3 (Mini)
2018 Jun 09 – L1-4, D1-3 (Mini)
**MD1** – 2018 Jun 12-17
**TS1** – 2018 Jun 18-21
2018 Jul 11 – L1-4, D1-3 (Mini)
**MD2** – 2018 Jul 23-28
2018 Jul 31 – L1-4, D1-3 (Full)
2018 Aug 17 – L1-4, D1-3 (Mini) – New HV groups
2018 Sep 01 – L1-4, D1-3 (Mini)
2018 Sep 07 – L1-4, D1-3 (Mini)
**MD3** – 2018 Sep 12-16
**TS2** – 2018 Sep 17-21
2018 Sep 26 – L1-4, D1-3 (Mini)

## A.3. Future projections for the strip tracker in 2023 after an integrated luminosity of 600 fb$^{-1}$

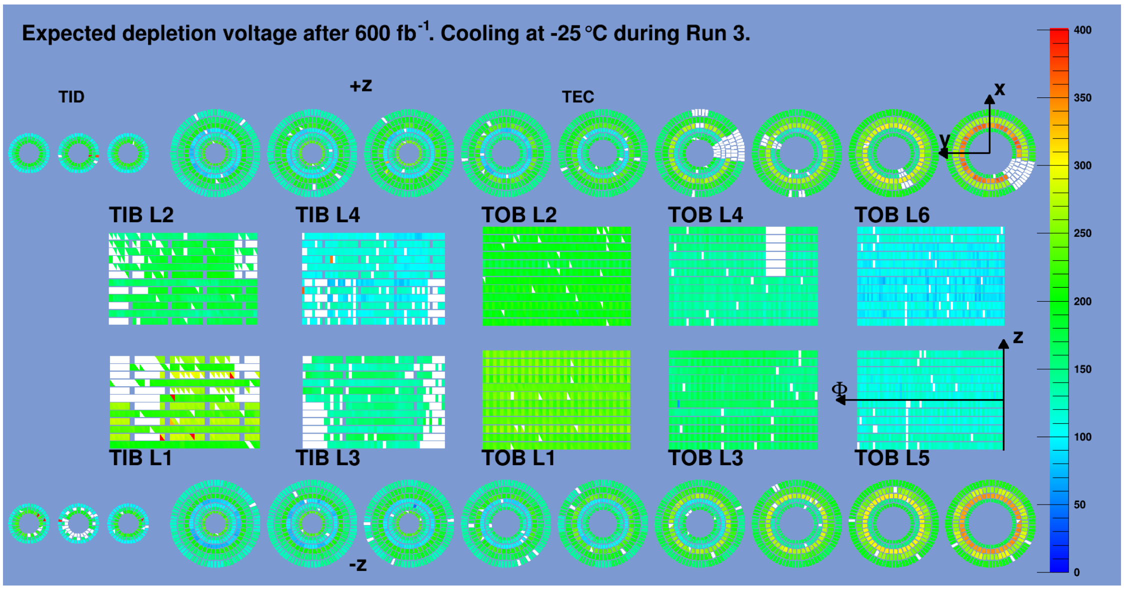


Figure A.1.: The expected depletion voltage after 600 fb$^{-1}$ in the strip tracker. The depletion voltage is predicted to stay well below the power supply limit of 600 V during Run 3. More details are given in Section 5.4.1.

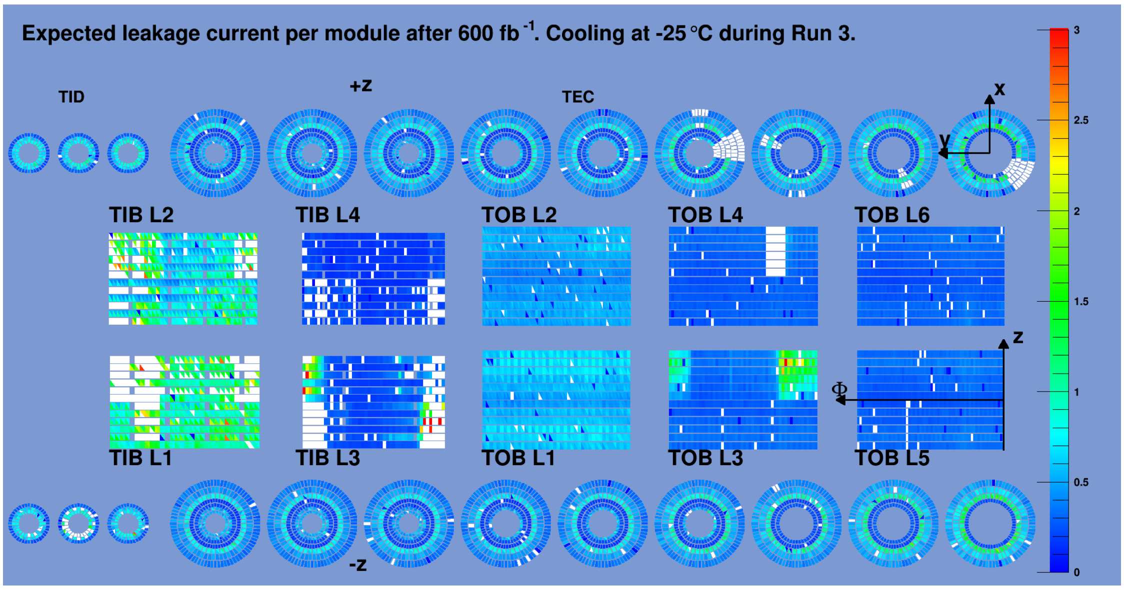


Figure A.2.: The expected leakage current per module after 600 $fb^{-1}$ in the strip tracker. The leakage current simulation is known to underestimate the data by about 20 %. Some regions approach critically high values where the risk of thermal runaways is imminent. More details are given in Section 5.4.2.

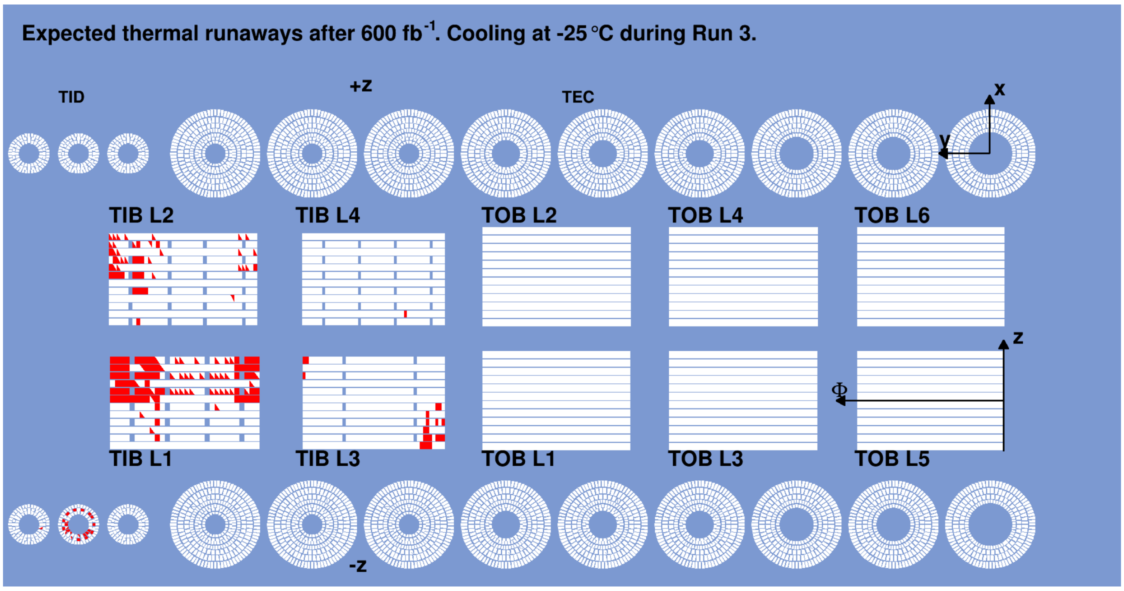


Figure A.3.: The expected distribution of thermal runaways after 600 $fb^{-1}$ in the strip tracker. More details are given in Section 5.4.2.